CALIBRATION AND RESULTS OF THE EQUIS II PLASMA IMPEDANCE PROBE (PIP)

by

Seth D. Humphries

A thesis submitted in partial fulfillment
of the requirements for the degree

of

MASTER OF SCIENCE

in

Electrical Engineering

Approved:

Dr. Charles M. Swenson Major Professor	Dr. Randy R. Jost Committee Member
Dr. Michael W. Tompkins Committee Member	Dr. Laurens H. Smith Interim Dean of Graduate Studies

UTAH STATE UNIVERSITY
Logan, Utah

2005

Abstract

Calibration and Results of the Equis II Plasma

Impedance Probe (PIP)

by

Seth D. Humphries, Master of Science

Utah State University, 2005

Major Professor: Dr. Charles M. Swenson
Department: Electrical and Computer Engineering

This thesis presents the calibration process and analysis results for the two Plasma Impedance Probe (PIP) units that were flown as part of the NASA Equis-II campaign from the Kwajalein Atoll. The work of calibration that was presented by Krishna Kurra for the PIP on the Floating Potential Measurement Unit (FPMU) is improved and extended herein. The sweeping impedance probe (SIP), the instrument formerly known as plasma sweeping probe (PSP), is an integral part of the PIP. For the SIP, the calibration presented in this work, calibration error less than 5% error is achieved. The calibration is applied to the flight data to yield impedance measurements. Balmain's normalized theoretical model is fit to normalized calibrated data to obtain electron density profiles within the range of about 2×10^3 to 5×10^6 $[N_e/\mathrm{cm}^3]$. Electron density profiles from the plasma frequency probe (PFP), also part of the PIP, are compared with the density profiles from the SIP and there is a close correlation, verifying the calibration and analysis of the SIP.

(108 pages)

This work is dedicated to my lovely, supporting wife.

Acknowledgments

I would like to thank Dr. Charles Swenson for making this happen and for all his valuable time. Thanks to Dr. Tompkins and Dr. Jost for their suggestions, help, and time.

I would like to thank Jeff Ward, Aroh Barjatya and Chad Fish for their time, ideas and corrections. Thanks also goes to Krishna Kurra and Chad Carlson without whom I would not have had a stepping stone. Much appreciation goes to Albert Hummel and Wayne Sanderson for their work and especially for their time in responding quickly to all my dumb requests. Good luck with the next generation! I also thank Allan McInnes for his help correcting formatting issues in LaTex.

The Utah State University student paper, The Statesman, made us laugh over a story about the PIP. On Friday, Sep. 3, 2004 they published a photo on the front page with a mistake in the caption. They called it the ¨Plasma Pimpedance Probe¨ or what became dubbed the ¨PIMP¨ (see fig. 1). I thank them for helping us not take our work too seriously. The photo and caption below are as they appeared in the Statesman, misspellings and all.

Fig. 1: Albert Hummel stands as the launch site in the island of Roi-Namur where the Plasma Pimpedance Probe (PIP) and the Sweeping Langmuir Probe (SLP) were launched into the ionosphere.

Contents

List of Tables

List of Figures

Acronyms

ACS	Attitude Control System
A/D	Analog-to-Digital signal converter
DCP	DC Langmuir Probe
Efield	Electric Field Probe
Equis	Equatorial Ionospheric Studies
ESSp	refers to the impedance phase measurement of the patch antenna
Ewinds	NASA investigation into the "Winds in the E-region" of the ionosphere
FPGA	Field Programmable Gate Array
FPMU	Floating Potential Measurement Unit
GPS	Global Positioning System
IGRF	International Geomagnetic Reference Field
ISS	International Space Station
ITAS	HP measuring device
LSQC	Least Squares Curve Fit
MSIS	Mass Spectrometer and Incoherent Scatter
PCM	Pulse Code Modulated
PFP	Plasma Frequency Probe
PIP	Plasma Impedance Probe
S-Band	Communication band, ranging from 1.55 GHz to 3.9 GHz
SDL	The Space Dynamics Lab at Utah State University
SIP	Sweeping Impedance Probe
SLP	Sweeping Langmuir Probe
SSE	Sum Squared Error
TM	Telemetry Matrix
UHF	Ultra High Frequency

USU	Utah State University
VHF	Very High Frequency
VHDL	Very high speed integrated circuit Hardware Description Language

Chapter 1

Introduction

The term ionosphere means a region, or sphere, where ions exist. The Earth's ionosphere is a region in the upper atmosphere that includes the near-earth space environment. The Earth's ionosphere extends from an altitude of about 70km to 1500km. Many of the atmospheric molecules in this region become ionized by the intense radiation from the Sun producing the ions of the ionosphere [1]. These ionized neutrals and free electrons constitute what space scientists call a collisional plasma, a quasi-neutral fluid of charged and neutral particles.

The ionospheric plasma and fluctuations therein can cause a myriad of interesting phenomena for space scientists. It also causes problems for engineers building both space and terrestrial systems. For instance, the reflection of low frequency communication waves off ionospheric plasma are important to short wave communication over long distances. The density and height of the ionosphere directly affect the ranges of these waves. This is especially important to short-wave radio operators as wave reflection allows them to communicate over the horizon. Fluctuations in density within the ionosphere, like waves on a pond, can distort the reflected signal causing loss of communication. High frequency waves can pass through the plasma, but fluctuations in the ionospheric plasma can slightly change the wave path by refraction resulting in distortion [2]. Variations in the ionosphere can cause periodic disruption of communications systems and GPS navigation signals [2, 3]. To predict these phenomena and prevent problems associated with them it is important to develop the science of space weather, similar to the terrestrial weather science developed by meteorologists.

Electron density is important for understanding ionospheric plasma fluctuations and characteristics. Consequently many different methods (or instruments) for measuring elec-

tron density have been devised. Measurement techniques may be broadly categorized as either in situ or remote sensing. In situ measurements are made while physically located in the medium of interest, thus they are made on satellites or on sounding rocket payloads. Examples of in situ measurement techniques are the sweeping Langmuir probe (SLP) [4–6], the DC Langmuir probe (DCP) [4–6], the sweeping impedance probe (SIP) [6–8], and the plasma frequency probe (PFP) [6, 9, 10]. Remote sensing measurements are done from a distance and can be based on satellites or more commonly on the ground. Some remote sensing techniques include incoherent scatter radar, ionosonde, Faraday rotation, and GPS [11]. These methods or instruments are by no means the only ones available to measure electron density in plasma, but are the more commonly used methods.

Utah State University builds and flies a suite of instruments for measuring electron density which it calls the plasma impedance probe (PIP) [12]. This suite consists of a DCP, PFP and SIP. The DCP is a sensing surface biased in the electron saturation region of the Langmuir curve [5]. The DC current collected provides a relative measurement of electron density. The second instrument is a PFP, an instrument which tracks a natural resonance of plasma as determined by the changing impedance of an antenna immersed in a plasma [9]. The frequency of this resonance is directly related to electron density. The SIP is similar to the PFP in that the measurement is based on the impedance of a short antenna immersed in a plasma. The SIP measures the impedance of the probe, magnitude and phase, as a function of frequency. USU has recently built a number of these PIP instrument suites for measuring electron density in situ. One unit was built for NASA to be installed on the International Space Station (ISS) named the Floating Potential Measurement Unit (FPMU). This unit is yet to be installed because of a lack of shuttle flights due to the tragic Columbia Shuttle disaster in 2003. Four units were flown as part of the E-Winds campaign and two units were flown as part of the Equis-II campaign. The units from the Equis-II campaign are the instruments on which this thesis will focus. Since all of these units are very similar, the calibration process herein may be applied to the other units as well.

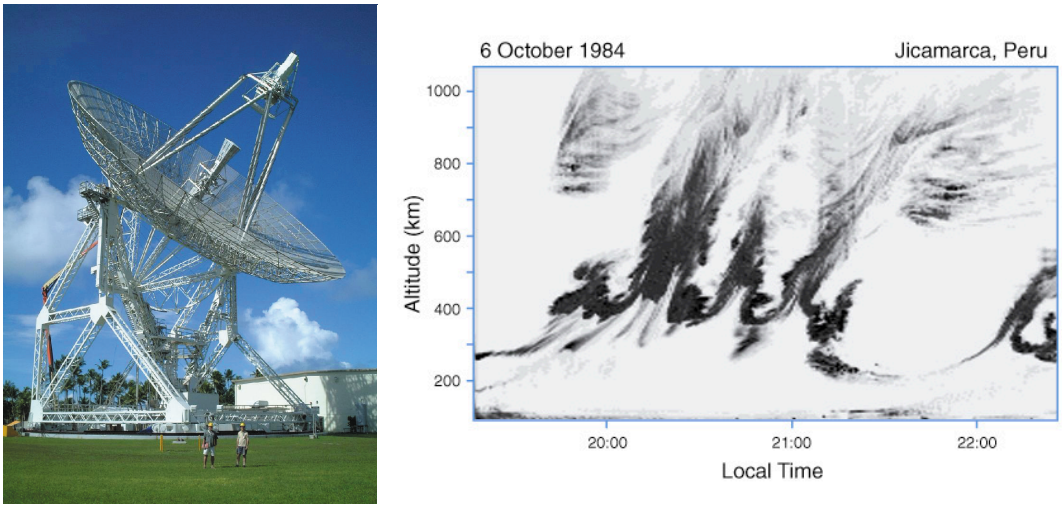

Fig. 1.1: Altair Radar at Kwajalein Atoll with radar image of plasma bubbling.

The calibration of the SIP unit that is part of the FPMU for the ISS was the subject of a thesis by Krishna Kurra entitled ¨Calibration of Plasma Impedance Probe on the Floating Potential Measurement Unit¨ [12]. The application of this calibration has not been tested as FPMU data is yet unavailable. Following the example laid forth by Kurra, the calibration of two SIP units flown as part of the Equis-II campaign will be presetned. Improvements to Kurra's methods will also be demonstrated herein. Additional methods to deal with instrumentation faults and limitations were developed as part of this thesis. The calibration is applied to flight data and suggestions for future improvement of the SIP are made.

1.1 The Equis II Campaign

As part of the NASA Equis II campaign, two Utah State University built PIP units were flown on two separate rocket launches in August of 2004. These two rockets (29.036 and 29.037, see the introduction in [10] for definition of the numbering system used) were part of an investigation led by David Hysell of Cornell University into the nature of thin layers in the lower altitude regions of the ionosphere. These layers are frequently observed by radars operating near the earth's equator in the VHF band like the Jicamarca Radio Observatory in Peru or the Altair radar in Kwajalein shown in fig. 1.1. The layers typically appear in the

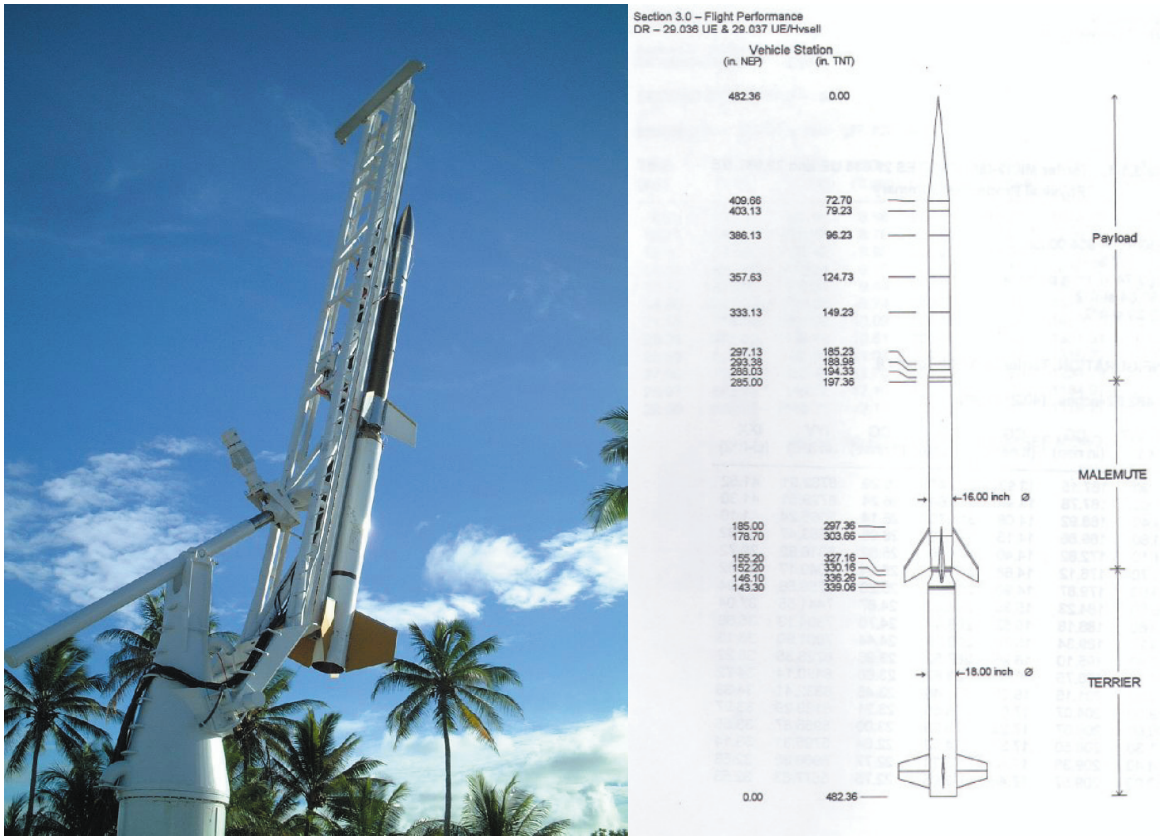

Fig. 1.2: 29.036 rocket on rail launcher at launch site on Roi-Namor Island and rocket diagram.

post-sunset evening and are thought to be precursors to the formation of equatorial plasma bubbles. The bubbles, seen as strong radar returns starting just before 20:00 local time in fig. 1.1, are common in the ionosphere near the equator and are responsible for enhanced scintillations on radio communications traveling through them. Therefore the 29.037 and 29.036 rockets were prepared and launched during part of the Equis II campaign in an effort to obtain data that could be used to eventually develop predictive capabilities for when bubbling will occur [13]. Launches took place from the island of Roi-Namor with support of the Altair radar as shown in fig. 1.1, [14, 15]. Altair is a VHF/UHF radar and was used to both observe when the low altitude layers were present as well as obtain electron density as a function of altitude (profile) remotely. The rockets were deployed on a rail launcher with each consisting of an instrumented payload on a two-stage rocket, see fig. 1.2. These rockets were put together in the NASA facilities at Wallops Island VA and

consist of a Malemute motor (stage 2) stacked on top of a Terrier motor (stage 1) giving an overall length of just over 40 feet.

The instrumented payloads consisted of a sweeping Langmuir probe (SLP) provided by Utah State University (USU), a plasma impedance probe (PIP) provided by USU and an electric field probe (Efield) provided by Pennsylvania State University. The location of the USU-built probes may be seen in the cartoon and diagram of fig. 1.3. The SLP boom was located under the nose cone and the PIP boom was located under a skirt on the tail of the payload. Each payload also contained an attitude control system (ACS) to orient the payload's spin direction parallel with Earth's magnetic field. The ACS was active shortly after payload separation from the motors and then again briefly at apogee. The goal of the ACS was to orient the payload so it would roll with the Earth's magnetic field. Electron density is dependent on orientation to the magnetic field so the re-orientation was done to minimize the affects of the spinning payload. This work will be only concerned with the PIP and the data collected from it during these two rocket flights.

In the days before launch, the 29.036 rocket was prepared, attached to the motors, and loaded on the rail. However, during final checkouts it was determined that the ACS system was not functioning properly. So the 29.037 payload was exchanged for the 29.036 payload and eventually launched in this configuration. The 29.036 payload was repaired and launched with the 29.037 rocket motors. NASA sometimes refers to this as 29.036 motors with the 29.037 payload and the second rocket as the 29.037 motors with the 29.036 payload.

The first launch (29.037 payload) took place on the 7^{th} of August, 2004 at 20:52:55.632 LT and the second launch (29.036 payload) was on the 15^{th} at 20:21:52.693 LT. Each rocket was launched in an easterly direction from the launch site and was allowed to splash down without recovery, as seen in fig. 1.4. The in-flight data was telemetered via an S-band radio link to the ground and recorded for later analysis. Both launches were considered successful with each obtaining an apogee height of nearly 425 km. The GPS coordinates of each flight

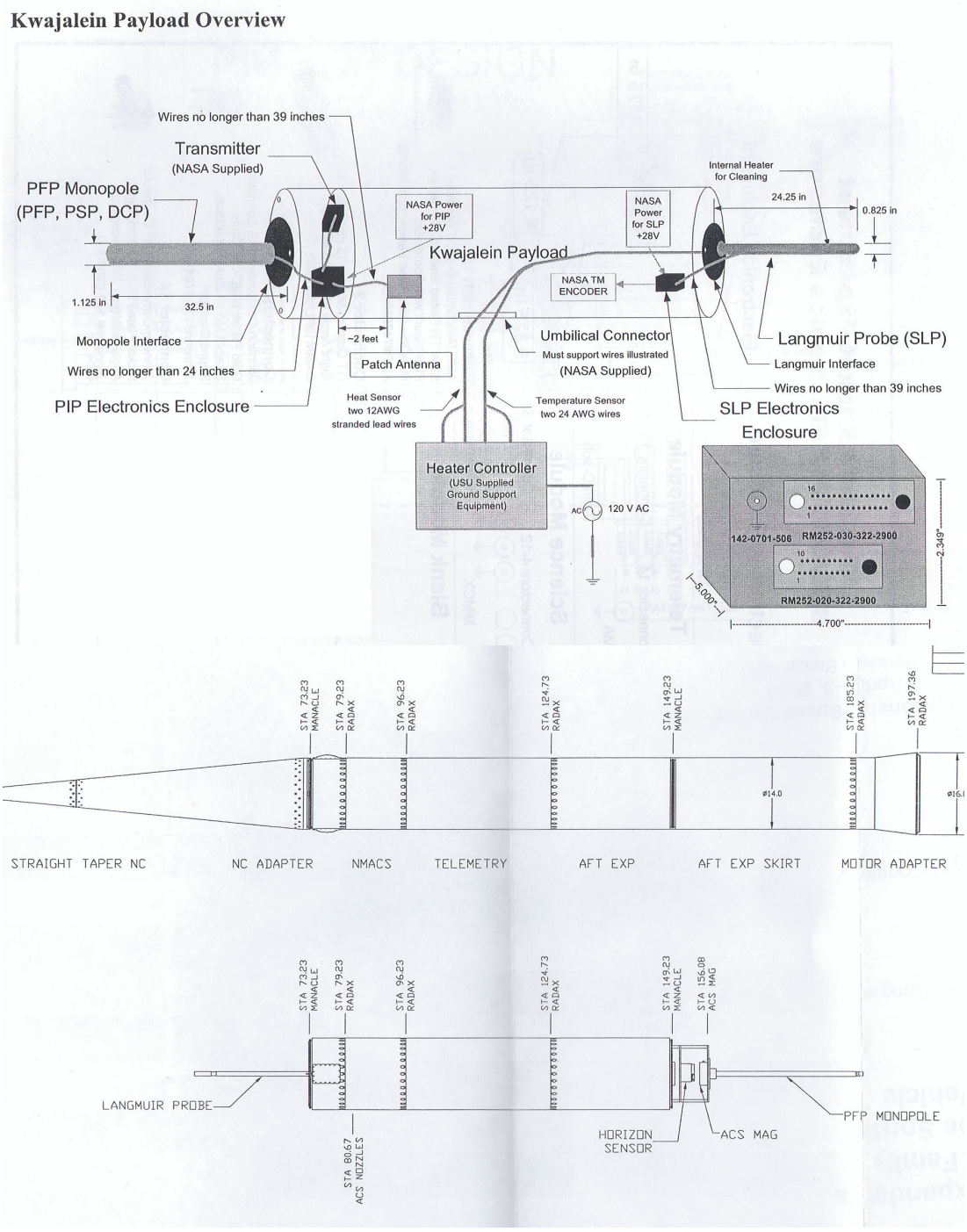

Fig. 1.3: Payload and instrument description.

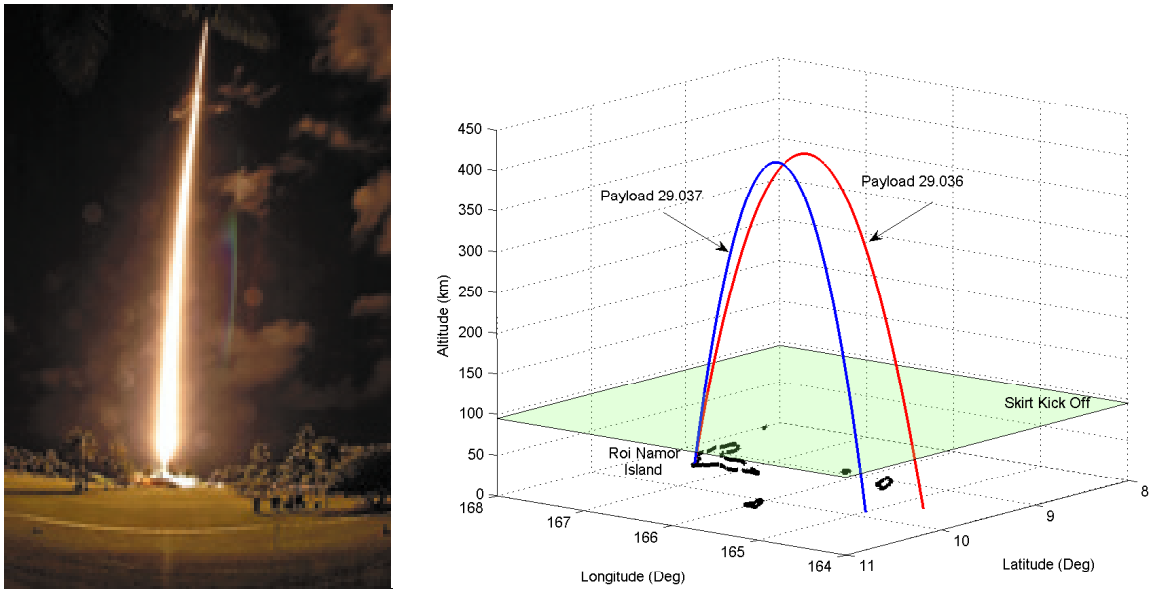

Fig. 1.4: A rocket launch and the flight trajectory of the two flights.

path were recorded and the corresponding flight paths are presented in fig. 1.4 along with an image of the launch of one of the rockets.

The data from the USU science instruments was formatted using PCM standards. PCM refers to a pulse code-modulated signal. The telemetry data for the Efield and SLP was designated as link 1 and also contained rocket house keeping. The telemetry data, for the PIP, was inserted into link 2 that also contained some rocket house keeping is show in fig. 1.5. Each matrix is defined to give certain temporal resolutions to measurements and a specific order to the stream of data. The ground station adds a time stamp as it receives each row of the TM and records each transmitted TM data stream as a binary stream. Each binary stream is saved as a file with a name distinction referring to the payload, date of flight, and link with the suffix ¨RC1¨. The data was picked out of the binary files via MATLAB scripts.

1.2 Impedance Probe Overview

The impedance probe measurement technique is based on observing the changing electric properties of a sensor as it is immersed in a plasma. The sensor is typically an elec-

Earle (27.144) Rocket Experiment
SDL-USU PIP Telemetry Matrix

SUBFRAME/ WORD	0	1	2	3	4	5	6	7	8	9	10	11	12	13	14	15
0	SYNC1	SYNC2	DCP	PFPf_H	PFPf_L	PFPQm0	PFPQp0	SFID	PFPQm1	PFPQp1	M5V	PFPQm2	PFPQp2	M12V	PSPm	PSPp
1																
2																
3																
4																
5																
6																
7	SYNC1	SYNC2	DCP	PFPf_H	PFPf_L	PFPQm0	PFPQp0	SFID	PFPQm1	PFPQp1	M5V	PFPQm2	PFPQp2	M12V	PSPm	PSPp

SUBFRAME/ WORD	16	17	18	19	20	21	22	23	24	25	26	27	28	29	30	31
0	IRMm	P5D	DCP	PFPf_H	PFPf_L	I12P	PFPQm3	PFPQp3	I5D	P5V	PFPQm4	PFPQp4	P12V	T2	PSPm	PSPp
1	P28V								I5P							
2	IRMp								I5M							
3	P28V								I12M							
4	IRMm								T1							
5	P28V								T2							
6	IRMp								T3							
7	P28V	P5D	DCP	PFPf_H	PFPf_L	I12P	PFPQm3	PFPQp3	T1	P5V	PFPQm4	PFPQp4	P12V	T2	PSPm	PSPp

Channel	Description	Rate (Hz)	~Range
SYNC1	Sync Word 1	1785.7	Dig
SYNC2	Sync Word 2	1785.7	Dig
SFID	Sub-Frame ID	1785.7	Dig
PFPf_H	PFP Lock Freq	3571.4	_MHz
PFPf_L	PFP Lock Freq	3571.4	_MHz
DCP	DCP Magnitude	3571.4	0-12.7 uA
PFPQm0	PFP Q Magnitude	1785.7	_Volt
PFPQm1	PFP Q Magnitude	1785.7	_Volt
PFPQm2	PFP Q Magnitude	1785.7	_Volt
PFPQm3	PFP Q Magnitude	1785.7	_Volt
PFPQm4	PFP Q Magnitude	1785.7	_Volt
PFPQp0	PFP Q Phase	1785.7	_deg.
PFPQp1	PFP Q Phase	1785.7	_deg.
PFPQp2	PFP Q Phase	1785.7	_deg.
PFPQp3	PFP Q Phase	1785.7	_deg.
PFPQp4	PFP Q Phase	1785.7	_deg.
PSPm	PSP Magnitude	3571.4	_Volt
PSPp	PSP Phase	3571.4	_deg.
IRMm	IRM Magnitude	446.4	_Volt
IRMp	IRM Phase	446.4	_deg.
I5D	+5VD Current Mon	223.2	0-+2.0A
I5P	+5V Current Mon	223.2	0-+2.0A
I5M	-5V Current Mon	223.2	0-+2.0A
I12P	+12V Current Monitor	1785.7	0-+0.5A
I12M	-12V Current Mon	223.2	0-+0.5A
T1	Power PCB	446.4	_C
T2	Telemetry PCB	2008.9	_C
T3	Science PCB	223.2	_C
M5V	-5V Voltage Monitor	1785.7	_Volt
M12V	-12V Voltage Monitor	1785.7	_Volt
P5V	+5V Voltage Monitor	1785.7	_Volt
P12V	+12V Voltage Monitor	1785.7	_Volt
P28V	+28V Voltage Monitor	892.9	_Volt
5VD	+5V Digital Voltage Mon	1785.7	_Volt
Word Rate		57142.9	

Last Modified 2/4/03

	SYNC1	SYNC2
	11110101111001	01100110000000

Bit Rate	800 kb/s
Word Size	14-bit
Word Rate	57142.857 w/s
Matrix Columns	32
Matrix Rows	8
Matrix Size	256
Major Frame Rate	223.214 f/s
Sub-frame Rate	1785.714 sf/s

Words Transmited MSB First

Fig. 1.5: Definition of the Telemetry Matrix for pulling data out of the data stream created by ground station.

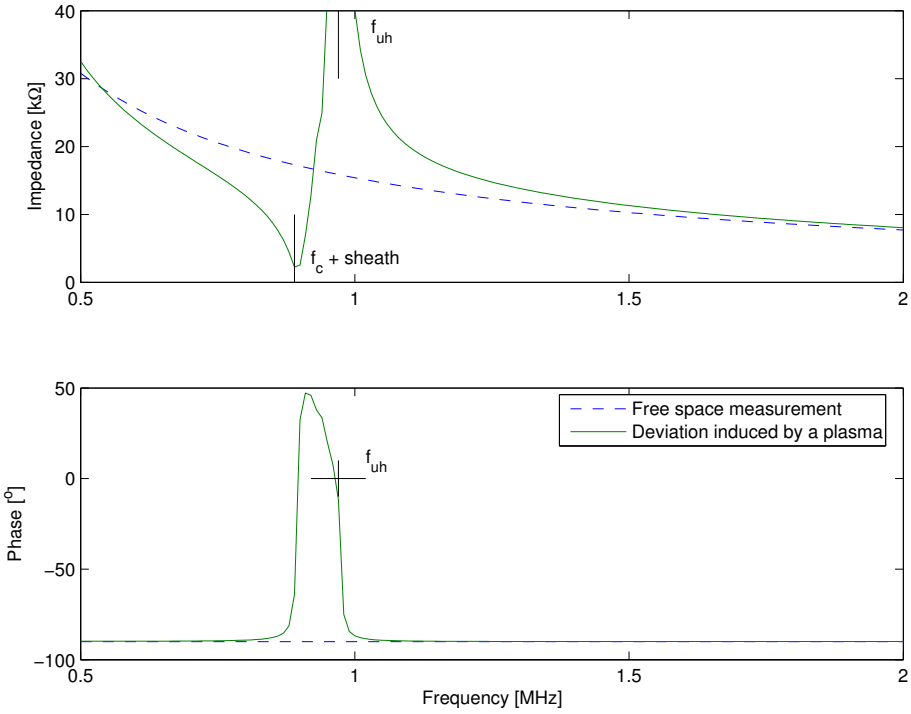

Fig. 1.6: Antenna impedance as a function of frequency as well as deviation due to plasma.

trically short monopole or dipole antenna. The term electrically short means that the physical length of the antenna is much smaller than the RF wavelength at the frequency of operation. The typical frequency operating range for ionospheric probing is between 100 KHz and 20 MHz corresponding to free-space wavelengths range from 15 m to 3 km. The antennas employed by USU typically have a physical length of less than one meter. Thus, unlike a communication antenna matched to the operating wavelength to provide a purely resistive input impedance in-band, the impedance probe's sensor is purely capacitive due to being electrically short. This impedance characteristic is shown as the dashed curve in fig. 1.6 and would be observed when the antenna is located with nothing around it for many wavelengths. In a plasma the impedance deviates form the pure capacitive response. The magnitude characteristic of the response is strongly dependent on the plasma density, the local magnetic field strength and the collision frequency of electrons with the background neutral gas. To a lesser extent it is dependent on the antenna's orientation to the magnetic field, the temperature of the plasma and the DC charge on the antenna which leads to the

formation of a plasma sheath surrounding the probe. All of these dependencies are referred to as the plasma parameters. The resulting impedance characteristics are complex and show series R-L-C like resonances at some frequencies and parallel R-L-C like resonances at other frequencies. This behavior is shown in fig. 1.6 along with the free space capacitive response. However, at frequencies above these resonances, high frequencies for the plasma, the impedance characteristics are simple capacitive.

In free space the antenna can be thought of as an empty parallel plate capacitor of value C_0. When the antenna is in a plasma, the measured capacitance will deviate from C_0. This can be thought of as filling the empty capacitor with a dielectric whose strength depends on the plasma's characteristics. The resulting measured capacitance C is defined by eq. 1.1.

$$C = \epsilon_r C_0 \tag{1.1}$$

The relative dielectric of the plasma, ϵ_r, can then be calculated as given by eq. 1.2 and thought of as the normalized admittance of the antenna.

$$\epsilon_r = \frac{C}{C_0} \tag{1.2}$$

For high frequencies the relative dielectric for a plasma is well known and frequency dependent and given by eq. 1.3 [16].

$$\epsilon_r(\omega) = 1 - \frac{\omega_p^2}{\omega(\omega - j\nu)} \tag{1.3}$$

Where ω is the operating frequency, ω_p is the plasma frequency and ν is the electron-neutral collision frequency. The plasma frequency is given in eq. 1.4 and is a function of

the plasma density, ρ_e, the electron mass, m_e, the electron charge, e, and the dielectric of free space, ϵ_r.

$$\omega_p^2 = \frac{\rho_e e^2}{m_e \epsilon_o} \tag{1.4}$$

In the ionosphere above about 140 km, the collision frequency is at least an order of magnitude less than the probing frequencies used in the Equis-II SIP measurements, ω. Thus, for much of the data obtained during the Equis-II campaign, eq. 1.3 may be reduced to eq. 1.5.

$$\epsilon_r(\omega) = 1 - \frac{\omega_p^2}{\omega^2} \tag{1.5}$$

Equation 1.1 follows from ideal conditions where the effective capacitance of the probe is completely filled by the plasma dielectric. In the real world, the geometry of the probe and cabling feeding it can add some complications to the measurement such that a part of C_0 is not filled with plasma. This can be thought of as a shunt capacitance, C_{shunt} in eq. 1.6.

$$C = \epsilon_r C_0 + C_{shunt} \tag{1.6}$$

This shunt capacitance can be due to factors such as incomplete shielding or guarding on the antenna feed cable. Its effect is highly dependent on the location in the signal path at which the instrument is calibrated (i.e. at the input to the electronics box, at the end of the test cables, at the end of the flight cables or the input to the antenna). This added shunt capacitance, if large compared to C_0, reduces the ability to accurately measure C_0 as well as ϵ_r. All efforts must be made to reduce the effective shunt capacitance but this is not easily accomplished in flight hardware.

Several models have been developed to capture the characteristics of the impedance of an antenna in a plasma. These models include the effects of the antenna's physical characteristics, such as length and radius, as well as most or all of the plasma parameters. These models attempt to give the impedance of the antenna at frequencies where the resonances occur. Perhaps the most widely used of these models is Balmain's [7] which gives the impedance for a cold plasma and an assumed triangular current distribution. The Balmain model captures the high frequency response better than the simple capacitor model previously discussed. However, the model has some deficiencies, the impedance changes at resonances from Balmain's model are too large as pointed out by Ward [17]. Ward has developed a finite-difference time-domain model that more accurately describes the antenna behavior in a plasma by numerically calculating the currents on the antenna. However, the run-time for Ward's model is far too long to be practical for data analysis purposes. While it does have some deficiencies, the Balmain model it does nicely capture the high frequency characteristics above the resonances and will be used to fit to the flight impedance data at those high frequencies.

The USU built plasma impedance probe (PIP) contains the sweeping impedance probe (SIP) and the plasma frequency probe (PFP). The SIP measures both the magnitude and phase of the probes' impedance at a set of frequencies in the operating range. The Balmain model is fit to this impedance data to extract electron density. The PFP uses the phase response to measure the frequency at which the capacitive response turns inductive. This transition occurs at the parallel R-L-C like resonance of the antenna and is associated with the plasma's upper hybrid frequency. Electron density is easily calculated from the upper hybrid frequency.

1.3 Thesis Summary

An outline showing the process of calibrating the SIP, applying the calibration to flight data and then fitting the data to probe theory to obtain density is shown in fig. 1.7. The calibration process entails two distinct measurements of a single set of calibrator standards. One set of measurements of the calibrators is made with a network analyzer whose calibra-

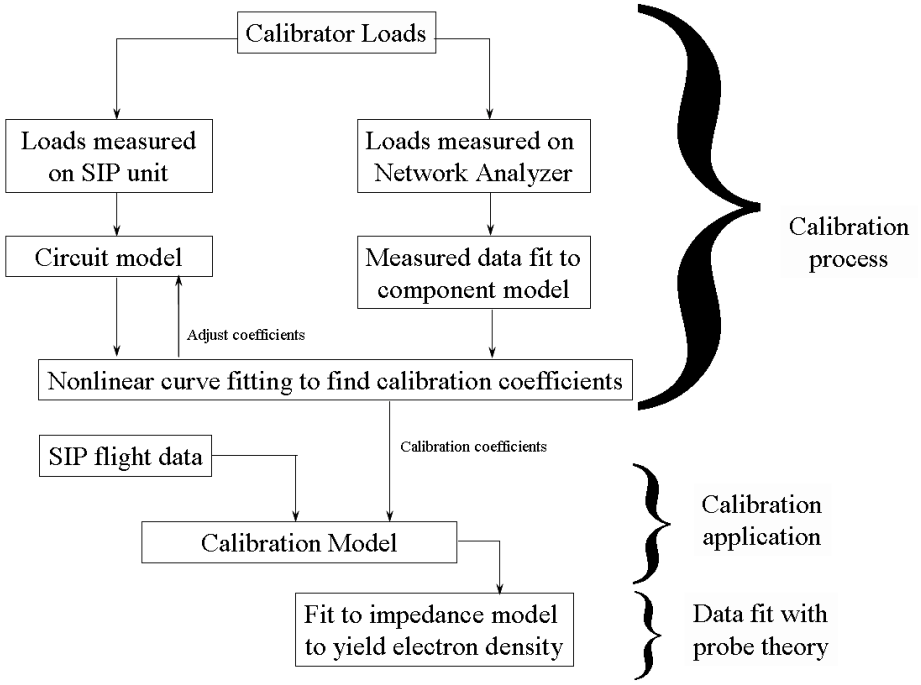

Fig. 1.7: SIP calibration flow chart.

tion is traceable. The other set of measurements of the calibrators is done with the SIP instruments before flight. A mathematical model of the instrument is developed complete with variable coefficients. The two sets of calibrator observations are compared by use of the mathematical model and the coefficients are adjusted until a best fit is achieved.

This thesis will include details associated with the calibration of the PIP units with the bulk of the emphasis on SIP calibration. Chapter 2 describes measurements using a set of loads used for the calibration of the SIP. The calibration loads were first placed on the SIP and measured resulting in digitized data in PCM counts. The same loads were then attached to a network analyzer and measured again. This process was to facilitate the calibration process by having a reference in both impedance and PCM counts. In chapter 3 this thesis covers the circuit model, the calibration model and the calibration coefficients used in the calibration process of the SIP. This process was first set up by Krishna Kurra in his master's thesis [12] and is generally followed in this work. Chapter 4 will discuss how values for the calibration coefficients, derived in chapter 3, are found. This process includes

implementation of the calibration equations from chapter 3 and also uses a least squares curve (LSQC) fit algorithm as well as the polynomial fit MATLAB function. Chapter 4 will also include the calibration of the PFP, another instrument on-board the PIP unit. Obtaining electron density from the SIP and PFP and the results will be discussed in chapter 5. Also in chapter 5 will be a comparison of the density results from the SIP and PFP to another independent instrument. The conclusion will discuss the calibration, the electron density results and make suggestions for improvement of future PIP units. The supporting material may be found in the appendices at the end of this work.

Chapter 2

SIP Calibration Data

The calibration of the SIP is based on two sets of data. The first is a set of measurements of calibrator standards. The second is a set of observations of these calibration standards by each of the SIP units. This chapter will discuss both elements. The calibration standards are the same ones used by Krishna Kurra on the FPMU [12], but they have been re-analyzed for the calibration of the Equis-II SIP units. There were several difficulties in preparing and working with the observations of the calibration standards on the SIP units including erroneous function of the instrument relative to the hardware documentation.

2.1 The Calibration Standards

The calibration standards are a set of simple resistors, capacitors and inductors. These calibrators have been used for the FPMU, the E-Winds mission and the Equis-II campaign reported in this work. The values of the calibrators were originally determined by Kurra through a process described in chapter 2 of his thesis [12].

The calibration standards were measured with a network analyzer so that their individual impedance characteristics would be known. A network analyzer at the USU Space Dynamics Lab (SDL) was used to make measurements of the real and imaginary components at ten different frequencies. These frequencies (in MHz) were 0.3, 0.5, 0.8, 1, 3, 5, 8, 10, 15, and 20, and Appendix A presents these impedance values in complex form.

Kurra fit, using magnitude only, circuit models to the measurements of the calibration standards. This left modes for the calibrators that were not as accurate as possible. This process has been improved by making use of both magnitude and phase (real and imaginary) information in a new set of model fits to the same data.

The value of the calibration standards is required at each of the frequencies of the SIP. Therefore, the measured impedance values of each of the standards must be interpolated over the entire frequency range based on the 10-point data acquired using the network analyzer. The calibration standards are real and non-ideal so three element circuit models are used to get a good interpolation of the data. The models are composed of three ideal elements with varying values for resistors, capacitors and inductors [18]. Transfer function forms, $H(s)$ of the three element models for real components, are presented in eq. 2.1 through eq. 2.3.

$$H(s)_{resistor} = L + (R//C) = \frac{Ls^2 + L/(RC)s + 1/C}{s + 1/(RC)} = \frac{RLCs^2 + RLCs + R}{RCs + 1} \tag{2.1}$$

$$H(s)_{capacitor} = R + L + C = \frac{Ls^2 + Rs + 1/C}{s} = \frac{LCs^2 + RCs + 1}{Cs} \tag{2.2}$$

$$H(s)_{inductor} = (R + L)//C = \frac{Ls + R}{LCs^2 + RCs + 1} \tag{2.3}$$

These transfer functions are then evaluated at $s = jw = j2\pi f$. Initially f represents the frequencies, in Hertz, used to measure the loads on the network analyzer. The values of R, C and L are then adjusted until a best fit to the measured calibrator is achieved. Kurra found values for R, C and L by minimizing the square of the magnitude error as in eq. 2.4.

$$\min \left[(|Z_{data}| - |Z_{model}|)^2 \right] \tag{2.4}$$

While this approach produced good fits for magnitude the phase of the models did not always agree with the observed data. Therefore the calibration standards were fit again with a norm that included phase information as in eq. 2.5.

$$\min \left[|Z_{data} - Z_{model}|^2 \right] \tag{2.5}$$

Equation 2.5 is the magnitude of the complex difference. This norm was completed outside of the MATLAB LSQC algorithm. This allows the LSQC algorithm to minimize the error

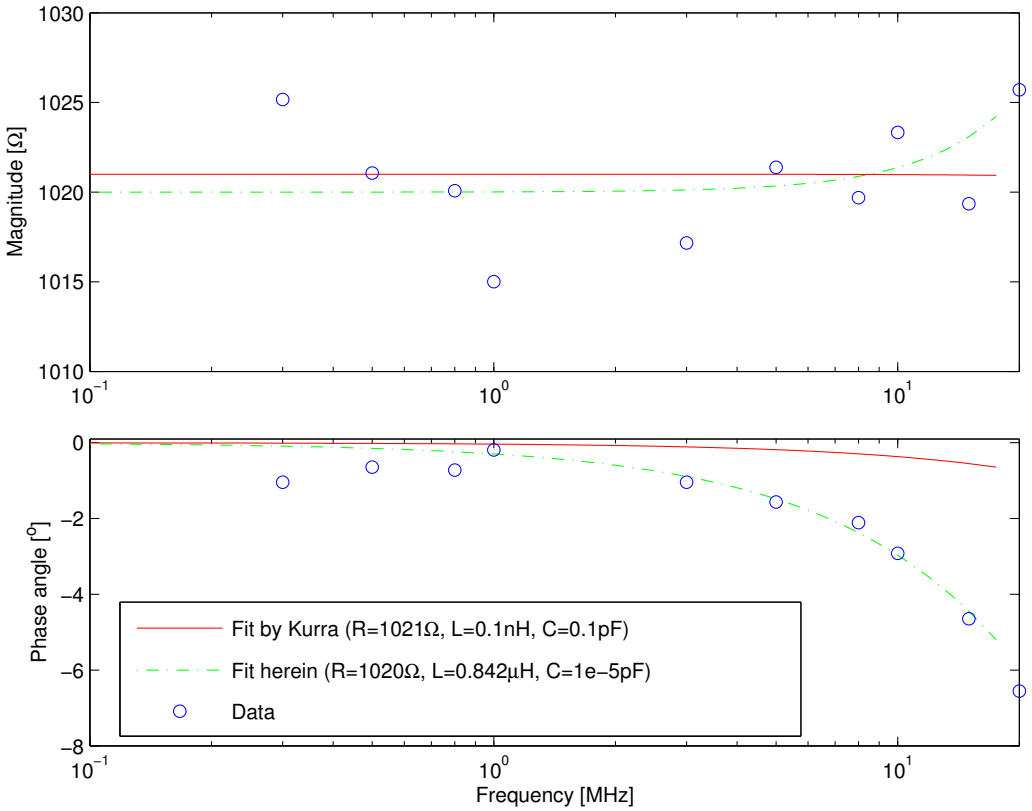

Fig. 2.1: Fitting using results both herein and from Kurra for the $1k\Omega$ calibration standard.

using both the phase and magnitude of the complex number. Using this strategy the network analyzer data was refit to the three element models. The entire set of plots of the fits may be seen in appendix D. The results of the fitting parameters (R, L, and C) are in table 2.1 with the nominal values being presented as well. The fit values are close to those reported values, i.e. fit resistances compared to corresponding resistor values. A process of removing data considered to be an outlier or erroneous could possibly improve the model fit to the data. However, this was not done with the fitting algorithm herein due to the limited number of data points in the data set.

Figure 2.1 demonstrates the importance of using the phase information in modeling the calibration standards. This plot compares Kurra's results [12] and those results from this chapter. The magnitude results are similar between the two different fittings but the

Table 2.1: Calibration load model fit values.

Load #	Value	R [Ω]	L [μH]	C [pF]
1	40Ω	39.923	0.000525	8.0228
2	82Ω	81.624	0.0018054	0.64304
3	120Ω	118.91	0.0056567	0.26811
4	200Ω	198.97	0.026732	0.05136
5	330Ω	330.79	0.073125	0.0041522
6	470Ω	472.31	0.18007	0.00019736
7	1kΩ	1021.2	0.84243	1.00E-05
8	3kΩ	3226.6	19.063	1.0104
9	10kΩ	11200	124.82	1
10	50kΩ	55561	595	1.00E+06
11	10pF	0.2	0.1	12
12	27pF	0.2	0.1	33.6
13	100pF	0.18377	0.0035988	112.5
14	72pF	0.2	0.0001	85.2
15	220pF	0.13511	0.019843	226.31
16	560pF	0.012299	0.0080127	532.47
17	1nF	0.0049233	0.0031625	915.42
18	0.1μH	0.0062774	0.090377	0.0001991
19	1.8μH	0.0086491	1.7585	0.023635
20	12μH	0.01916	12.301	1.8043
21	39μH	0.98898	38.578	4.1277
22	82μH	1.0008	82.42	1.8583
23	120μH	20.011	117.24	2.7445

phase results are different. The fit phase results from this chapter fit the measured phase much better than did Kurra's fitting results.

2.2 Calibration Standards on SIP

2.2.1 Setup and Data Acquisition of Calibration Loads on SIP

After final assembly of the PIP electronics box each calibration standard was connected in place of the antenna and the PCM telemetry data recorded. Communication from the SIP unit to a PC was done via the ITAS reader at SDL which replaced the flight payload telemetry system as well as the ground receiver station. As the calibration standards were

placed on the antenna several seconds of sweeps were recorded. This process was repeated four times for each load. This resulted in a large number of SIP sweeps for the calibration of each load. The concept was to average these sweeps thereby reducing the amount of noise in the representative observations of each calibration standard.

The ITAS is an older piece of hardware and decoding its formatting of the data was problematic. The ITAS, unlike the ground station to capture flight data, gives a tag number to each set of collected data. The tag numbers are related to the Telemetry Matrix (TM) definition, as seen in fig. 1.5, but they are not the same. The tag number definitions are defined by reading the TM from left to right, top to bottom grouping data from the same instrument, having the same name in the TM. This holds true with the exception the phase measurement of a patch antenna (ESSp) instrument being tag 29 instead of a tag of 30 as counting would suggest.

2.2.2 Discussion of Observed Data Calibration Loads on SIP

The SIP sweeps were not synchronized with the ITAS data acquisition system. Therefore, the starting point inside each file for each calibration measurement was random and a sweep starting point had to be found. Several attempts were made to automate this process, but each failed and the starting point for all four sets of twenty-three loads for each antenna were found one at a time manually.

Once a starting point for each set of sweeps was found the sweeps could be pulled from all four sets for each load. The sweeps were then averaged to yield a representative sweep. These averaged sweeps for the 29.037 and 29.036 payloads are presented in fig. 2.2 and fig. 2.3. The top panel is the SIP magnitude channel for the resistive calibration standards. The second panel in the figure is the corresponding SIP phase. The following panels are for the magnitude channel and phase channel of the capacitive and then the inductive standards.

The first observation of the SIP magnitude channel data, seen in fig. 2.2 and fig. 2.3, is that the instrument goes into saturation at a high value of about 16300 PCM counts. This is most evident in the capacitor data. The instrument magnitude channel has a floor of 0

PCM counts as seen in the inductor data. The phase data shows a striking feature between 9 and 14 MHz that is consistent between all channels. This is obviously non-physical and indicates an error in the instrument. The phase data between about 2 and 8 MHz may be usable as it generally shows the expected behavior of being near zero for resistors, low for capacitors and high for inductors. There are obvious complications in this phase data as the instrument magnitude channel goes into saturation. Because of apparent problems with the phase channel no attempt has been made to calibrate it or use it in the magnitude calibration process. Some of the measured values of the standards are saturated. The phase plots of these figures documents that the phase measurements are erroneous. In particular, the erroneous phase information of the capacitors, not in saturation, and the resistors is seen in fig. 2.2 and fig. 2.3.

2.2.3 SIP Sweep Frequencies Discussion

During the reduction of the calibration data it was discovered that a SIP sweep consisted of 257 points instead of the 256 points as expected. This was also observed in the flight data. Each sweep was expected to range from 100kHz to 20MHz and contain 18 points spaced at 50kHz, 225 points spaced at 40kHz, 10 points spaced at 500kHz, and finally 2 points spaced at 2.5MHz. This discovery of anomalous behavior from the designed behavior meant that the data no longer corresponded to the expected frequencies. After looking at the data and reviewing the VHDL code controlling the SIP frequencies, it was found that varying frequency steps were added to the starting frequency 256 different times resulting in 257 distinct frequencies. The extra step caused the unit to reset prematurely resulting in the first and the last points of each sweep being the same frequency. We will consequently consider these two points the first two points of the sweep. There was also supposed to be two points spaced at 2.5MHz at the end of each sweep, but it was found by looking at the data that there was only one. This meant that there was an extra step in one of the other step sizes. After much effort in looking at the data and searching through the VHDL code, it was concluded that an extra step in the 50KHz step range had been included.

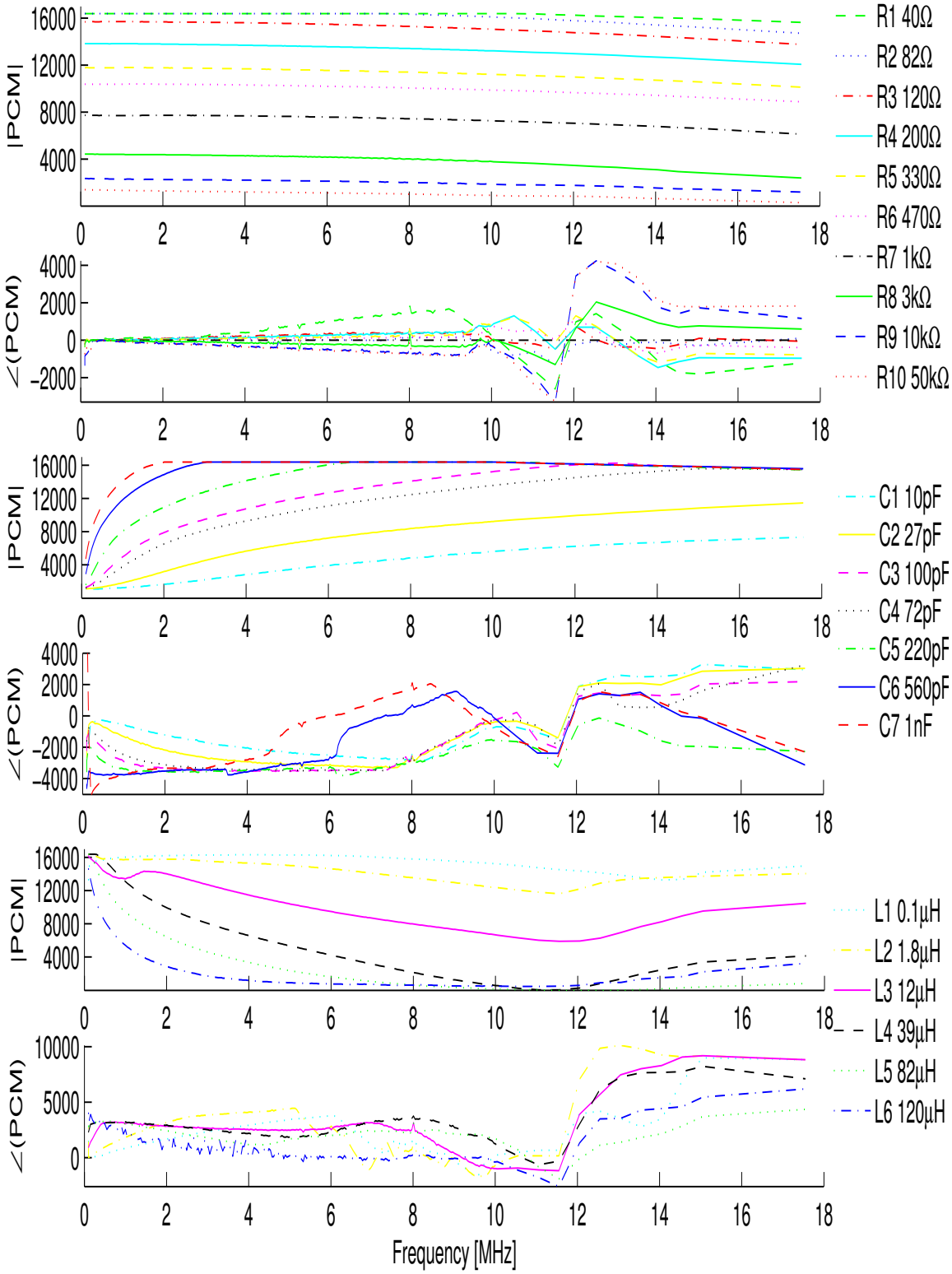

Fig. 2.2: Loads measured while attached to the SIP unit on payload 29.037.

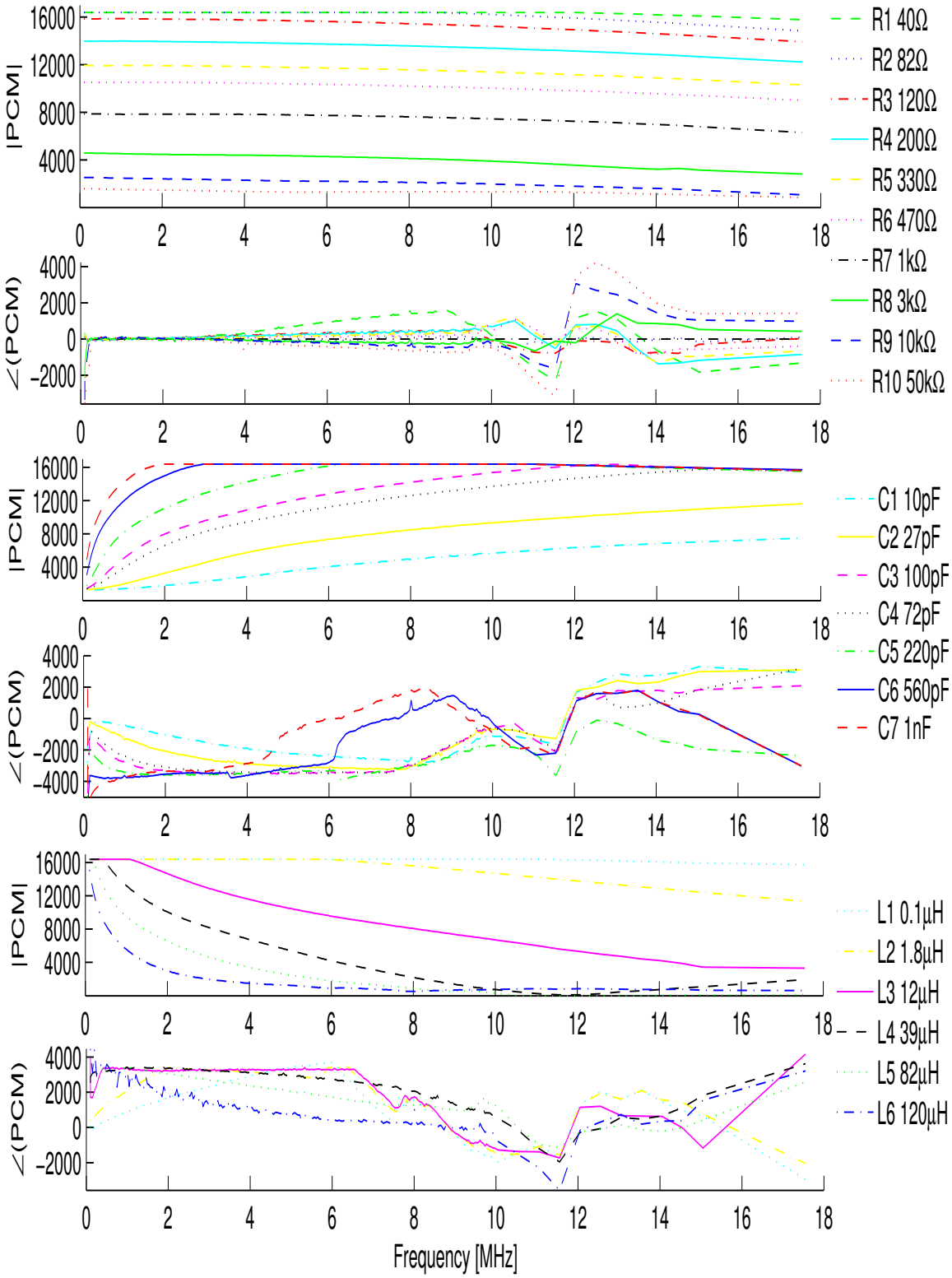

Fig. 2.3: Loads measured while attached to the SIP unit on payload 29.036.

The frequencies at which the SIP made measurements are presented in appendix B and appendix C.

Chapter 3

Sweeping Impedance Probe Circuit Model

The calibration of the Sweeping Impedance Probe (SIP) is accomplished by determining parameters of a calibration model that best fit known calibration standards as observed by the probe. Within this chapter we develop a mathematical model of the SIP for calibration based on the circuit model of the instrument. This model turns out to be coupled such that the instrument's telemetry magnitude channel is dependent on both the magnitude and phase of the antenna's impedance. Likewise, the telemetry phase output is also dependent on both the phase and magnitude of the antenna's impedance. This coupling of the magnitude and phase channels was an unfortunate result of a fix for a perceived problem that effected just the phase measurement. Additionally, the data from both instruments phase channels is poor so techniques and calibration models are developed that can be applied, with limited validity, given only magnitude data. These limited models are presented in this chapter for the purpose of analyzing Equis-II flight data.

3.1 SIP Circuit Model

The block diagram in fig. 3.1 represents the SIP circuit model. The instrument is based around a transimpedance amplifier (OA_1). This amplifier is driven with an RF signal represented by V_{in}. The frequency at V_{in} varies from 100KHz to about 17.5MHz with 257 points as outlined in section 2.2.3. The gain of OA_1 is set by the feedback parallel combination of the 430Ω resistor and the $3.9pF$ capacitor. The drive signal is then subtracted from the output of OA_1 by OA_2, the differencing amplifier. The output of OA_2 feeds a magnitude detector that has a logarithmic output and a phase detector. Both of these circuits are described in more detail by Carlson [10]. It is at this point that an unfortunate error was made in the circuit design. A voltage divider, the 150Ω

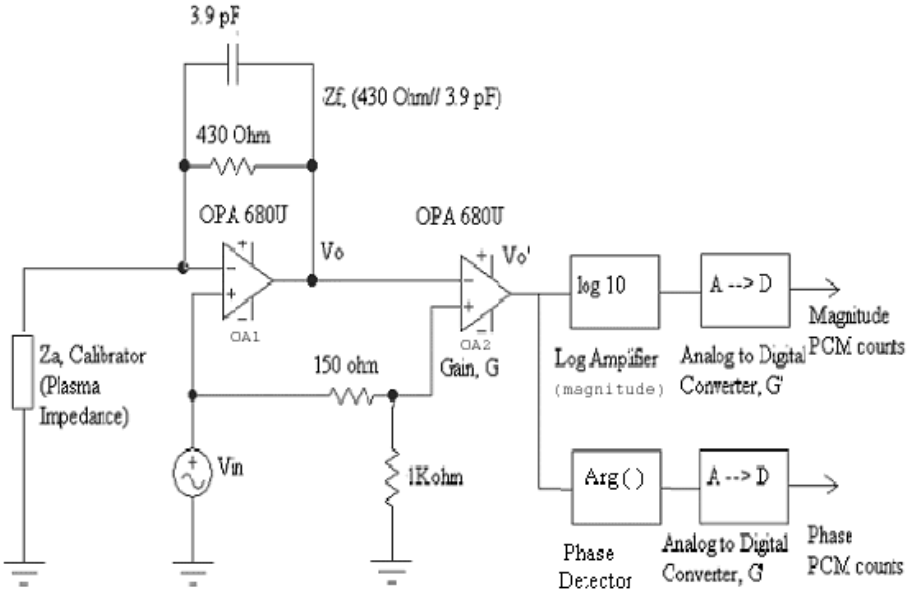

Fig. 3.1: Circuit diagram of the SIP measuring circuit.

and $1k\Omega$ resistors, was used to reduce the drive signal before subtraction. This was done because when the antenna was at very high impedance or in an open circuit condition the transimpedance amplifier would have reproduced the drive signal thus yielding an output of zero volts at the difference amplifier. This zero input caused problems with the phase detector circuit. It was thought that bleeding through about 13% of the drive signal for proper operation of the phase detector would result in a minor calibration inconvenience. This has proved wrong.

The derivation of mathematical relations for both the phase and magnitude are presented by Kurra [12]. A brief derivation of the magnitude is presented here in eq. 3.1 through eq. 3.7.

The output of OA_1 is $V_0(\omega)$ which can be calculated from the input voltage V_{in} as given by eq. 3.1 using $Z_a(\omega)$, the antenna impedance, and $Z_f(\omega)$, the amplifier feed back impedance of OA_1 defined in eq. 3.2. The output of OA_2, $V_0'(\omega)$, is found as a function of $V_0(\omega)$, where $G(\omega)$ is the gain of the amplifier and $\beta(\omega)$ is from the voltage divider

defined in eq. 3.4. The gain of the amplifier circuit, the values of the resistors, as well as all other values herein have been assumed to be frequency dependent (denoted as ω) although ideally these values would be independent of frequency. Equation 3.5 results from substituting eq. 3.1 and eq. 3.4 into eq. 3.3 and simplifying.

$$V_0(\omega) = V_{in}\left(1 + \frac{Z_f(\omega)}{Z_a(\omega)}\right) \tag{3.1}$$

$$Z_f(\omega) = R(\omega)//C(\omega) = \frac{1}{\frac{1}{R(\omega)} + j(\omega)} = \frac{R(\omega)}{j\omega R(\omega)C(\omega) + 1} \tag{3.2}$$

$$V_0'(\omega) = G(\omega)\left(V_0(\omega) - \beta(\omega) * V_{in}\right) \tag{3.3}$$

$$\beta(\omega) = \frac{1k\Omega}{150\Omega + 1k\Omega} = 1 - \alpha(\omega) \tag{3.4}$$

$$V_0'(\omega) = G(\omega)V_{in}\left(\alpha(\omega) + \frac{Z_f(\omega)}{Z_a(\omega)}\right) \tag{3.5}$$

Equation 3.5 represents the signal prior to both the phase detector circuit and the magnitude detector circuit. The log amplifier and the 14-bit A/D converter make up what is referred to as the magnitude detector circuit. The log amplifier has gain $G_L(\omega)$ and a base of K, nominal base 10. The 14-bit A/D converter has offset $O'(\omega)$ and gain $G'(\omega)$. Together this results in gain $G_m(\omega)$ and offset $O_m(\omega)$ for the magnitude detector circuit. The output of the magnitude detector circuit comprises the magnitude measurement and is in units referred to as PCM counts, eq. 3.6. The data has been digitized into integer output and this is represented by the function ¨INT¨. This reference to integerized data will be assumed and thus it will be dropped in subsequent references. After substitution of eq. 3.5 into eq. 3.6 and simplification the result is eq. 3.7.

$$PCM(\omega) = INT\left[G_m(\omega)\log_{K(\omega)}\left|V_0'(\omega)\right| + O_m(\omega)\right] \tag{3.6}$$

for $K(\omega) \approx 10$

$$PCM(\omega) = m(\omega)\log_{K(\omega)}\left|\alpha(\omega) \; + \; \frac{Z_f(\omega)}{Z_a(\omega)}\right| \; + \; b(\omega) \tag{3.7}$$

where

$$b(\omega) = G_m(\omega)\log_{K(\omega)}(G(\omega)V_{in}) + O_m(\omega) \tag{3.8}$$

$$m(\omega) = G_m(\omega) \tag{3.9}$$

$$\alpha(\omega) = 1 - \beta(\omega) \approx 0.13 \tag{3.10}$$

The feedback impedance of OA_1, Z_f, is found by looking at $R(\omega)$ and $C(\omega)$. It will now be assumed that all variables are a function of frequency so the 'ω' will be dropped and assumed in future equations. It is important to note that even coefficients such as R, which represents a real resistor, does not have the same impedance value at all frequencies and consequently is considered to be a function of frequency. The variables b, m, K, α, R, and C are called the calibration coefficients that may be either calculated or be determined by fitting algorithms. The results of these fitting algorithms are presented in chapter 4.

The circuit model, eq. 3.7, can be simplified (eq. 3.11), expanded (eq. 3.12) and then solved for $|Z_a|$ (eq. 3.13) using the quadratic formula.

$$X = K^{[(PCM-b)/m]} = \left|\alpha + \frac{Z_f}{Z_a}\right| \tag{3.11}$$

$$X^2 = \alpha^2 + 2\alpha\cos(\theta_f - \theta_a)\frac{|Z_f|}{|Z_a|} + \frac{|Z_f|^2}{|Z_a|^2} \tag{3.12}$$

$$|Z_a| = \frac{|Z_f|\left[\alpha\cos(\theta_f - \theta_a) \pm \sqrt{X^2 - \alpha^2\sin^2(\theta_f - \theta_a)}\right]}{X^2 - \alpha^2} \tag{3.13}$$

where

$$\theta_f = \arg(Z_f) \tag{3.14}$$

$$\theta_a = \arg(Z_a) \tag{3.15}$$

3.1.1 Problems With the Circuit Model

It was thought, during the design phase of the SIP circuitry, that the value of α would not be an important issue in the calibration of the instrument. Based on this thought, eq. 3.13 could be greatly simplified and the magnitude would not be dependent upon the phase.

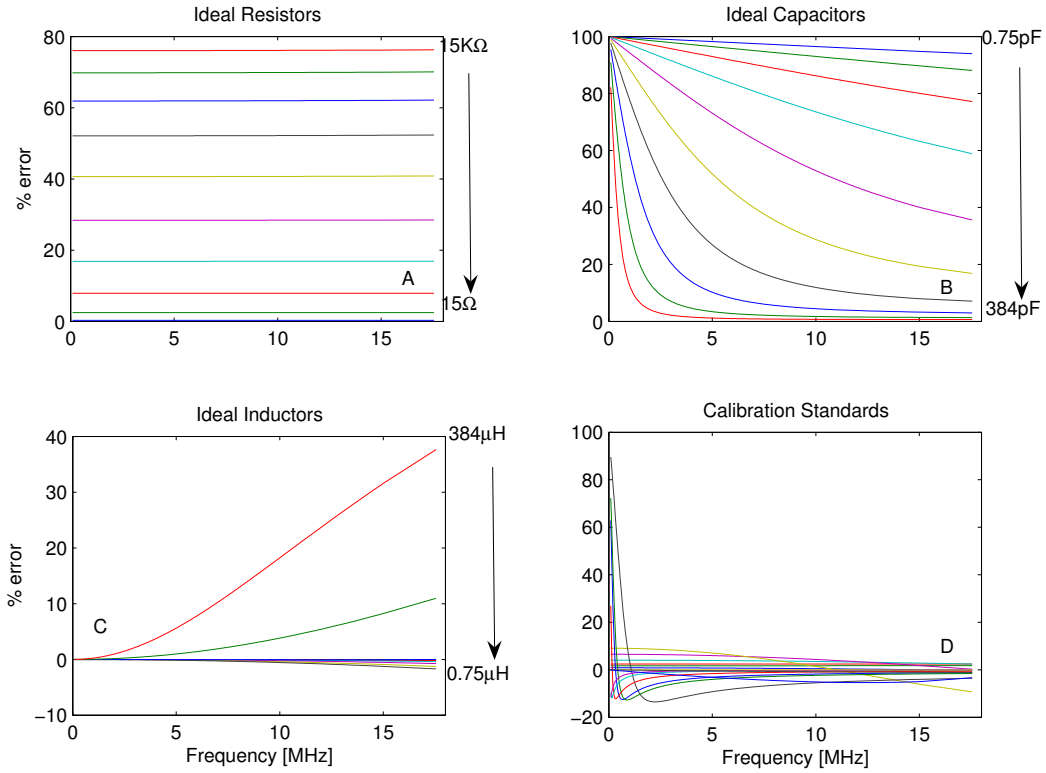

Fig. 3.2: Error due to assuming $\alpha \approx 0$ with ideal resistors(A), capacitors(B), inductors(C), and the calibration standards(D).

If the value of X, from eq. 3.11, is evaluated twice, once using α and again with the assumption that $\alpha \approx 0$, any error associated with α will be evident. To demonstrate the error introduced by this assumption ideal loads were created, ten for each type, and ranged to cover possible real load values as well as extremes values. The ideal resistors ranged from 15Ω to 15kΩ incremented cubically, the capacitors ranged from 0.75pF to 384pF in increments of powers of 2, the inductors ranged from 0.75μH to 384μH also incremented as powers of 2. The error introduced by these ideal loads is presented in fig. 3.2. Another demonstration of the error is seen in the evaluation of X by using the non-ideal calibrator standards. Notice that the error associated with the capacitor loads, seen in fig. 3.2, is near one hundred percent for capacitance similar to what is expected from the flight data. Therefore α can not be ignored and must be included.

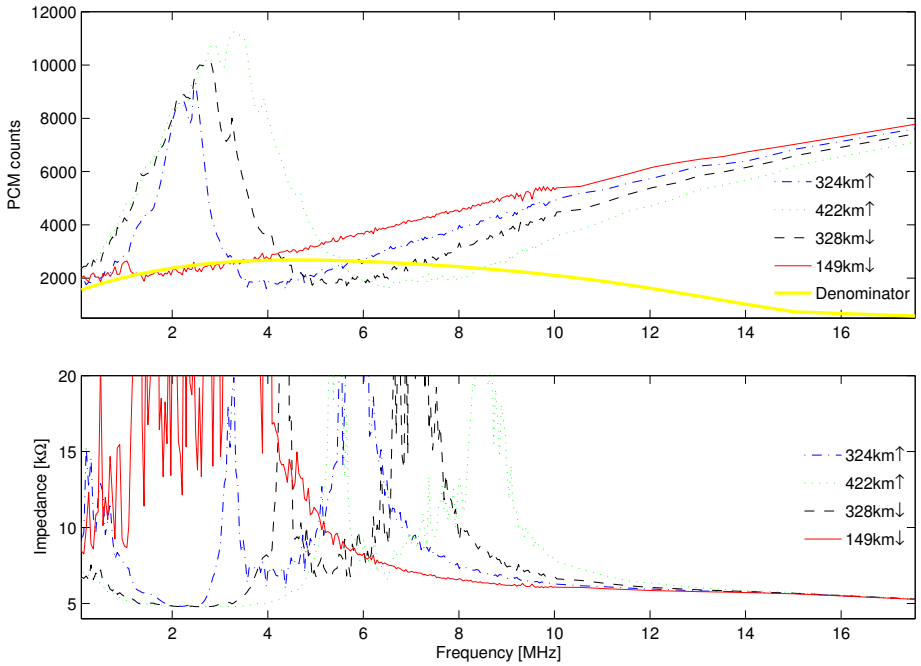

Fig. 3.3: The top portion shows the data in PCM counts along with the denominator. The denominator is calculated using fit values of the calibration coefficients. The bottom portion shows the results once the data is converted to impedance using the calibrator equation and the fit calibration coefficients for payload 29.037 data.

3.1.2 Poles in Circuit Model

There are is a problem associated with the circuit model, eq. 3.13. The denominator of eq. 3.13 is a difference of squares, quadratic. Thus there are two cases where the denominator will be identically zero. These two cases are called poles. When evaluating the model if the denominator approaches zero the model result will approach infinity. To find out when this happens the denominator from eq. 3.13 was solved for the PCM data resulting in eq. 3.16. Note that the pole equation, eq. 3.16, is dependent on most of calibration coefficients.

$$PCM = b + (m/2)Log_{K}(\alpha^2) \tag{3.16}$$

As the rocket flies into the plasma the capacitance of the antenna drops. This results in a capacitance in the plasma that may be much less than 10pF, the value of the smallest capacitor calibrator standard. As the capacitance decreases the data can cross the line where the denominator is zero, see the top half of fig. 3.3. If the data crosses or approaches

this line it will result in large discontinuities in the data once converted to impedance, see bottom half of fig. 3.3.

To correct for the poles the calibration coefficients must be fit so as to shift the denominator line, seen in the top portion of fig. 3.3, to lower PCM values or even to negative PCM values. Since the smallest calibrator load (the 10pF capacitor) is larger than the capacitance of flight data the poles that can appear in the flight data do not appear when fitting for the calibration coefficients. Therefore, the fitting algorithm alone can not fully correct for the poles. It is necessary that the person performing the calibration choose appropriate loads to include in the fitting algorithm that will yield both a good fit as well as shift the denominator line sufficiently. This process is not able to be automated at this time. Due to this extra step in the fitting routine, the fitting took more time and effort than anticipated. This is presented in chapter 4.

3.2 Results of Phase Dependence of the Magnitude Data

Equation 3.13 demonstrates that the magnitude of the antenna impedance, $|Z_a|$, is indeed dependent on the phase of the antenna impedance, θ_a, it further shows that if α had been set to zero then the magnitude would be independent of the phase. The calibration data, see fig. 2.2 and fig. 2.3, suggests that the phase measurements of the instrument are not accurate. Because of this error in the observed phase measurements, it is important that the phase and magnitude in a final flight calibration equation be separate from each other for the calibration application process. There are several different manners to deal with this dependency but all approaches introduce some error. The various methods involve making assumptions to simplify either eq. 3.11 or eq. 3.13. This section will focus on simplifying eq. 3.11.

Since the flight data will be capacitive above the upper hybrid resonance then it can be assumed, $\theta_a \approx -90^o$, and plugged into eq. 3.18. Using eq. 3.12 the cos term may be expanded to $\cos\theta_f \cos\theta_a + \sin\theta_f \sin\theta_a$. The the assumption $\theta_a \approx -90^o$ may be plugged in and then the expanded cos term becomes simply $-\sin\theta_f$.

The error associated with making this assumption for calculating X may be seen in fig. 3.4 and is defined in eq. 3.17. The same ideal loads used in demonstrating the effects of α are used in demonstrating the error introduced by this assumption.

$$\text{Percent Error} = 100 * \frac{\left|\alpha + \frac{Z_f}{Z_a}\right| - \sqrt{\alpha^2 - 2\alpha \sin\theta_f \frac{|Z_f|}{|Z_a|} + \frac{|Z_f|^2}{|Z_a|^2}}}{\left|\alpha + \frac{Z_f}{Z_a}\right|} \tag{3.17}$$

Using this assumption and using eq. 3.11, eq. 3.12, and eq. 3.13 the final calibration model, eq. 3.18, can be derived for the impedance magnitude independent of the impedance phase.

$$|Z_a| = \frac{|Z_f| \left[\alpha \sin\theta_f \mp \sqrt{K^{[2*(PCM-b)/m]} - \alpha^2 \cos^2\theta_f}\right]}{\alpha^2 - K^{[2*(PCM-b)/m]}} \tag{3.18}$$

Equation 3.18 is the calibration model that will be used for the flight data in the region where that data is purely capacitive.

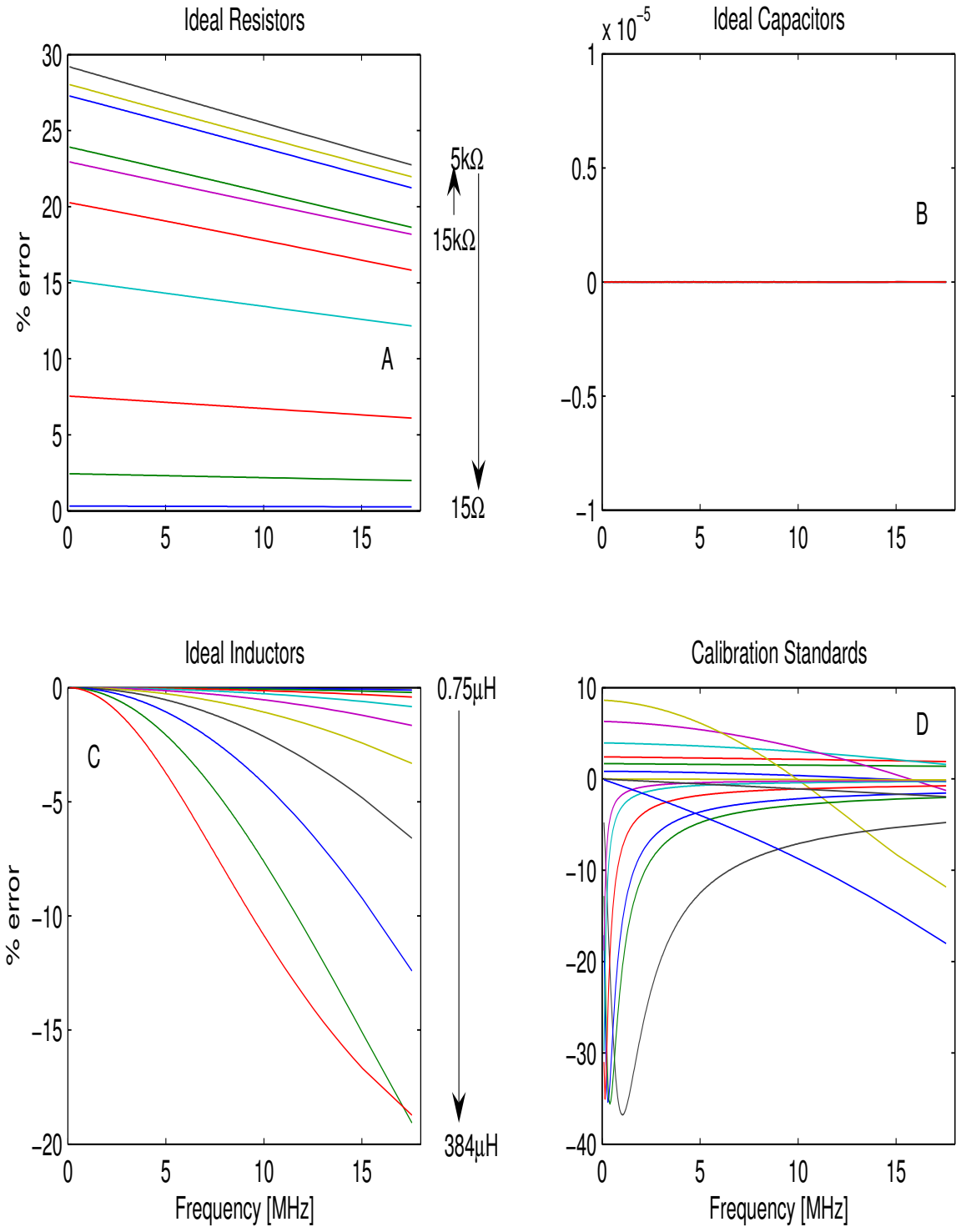

Fig. 3.4: The percent error due to ideal resistors(A), capacitors(B), inductors(C), and calibration standards(D). Notice the y axis in B is multiplied by 10^{-5}.

Chapter 4

PIP Calibration

This chapter describes the calibration of both instruments that comprise the PIP; those are the SIP and the PFP. The calibration of the SIP consists of finding unknown coefficients by adjusting those coefficients so that the observations of the calibration standards made on the SIP unit match the calibrator standards. Once the calibration coefficients are known, eq. 3.18 can be applied to the SIP data from the two rocket flights which will result in calibrated impedance data for each flight. The calibration of the PFP is much simpler as it amounts to knowing the frequency of the oscillator that is tuned to the plasma resonance.

4.1 Calibration of the SIP

The values of the components in the SIP circuitry are only known to within a certain degree of precision. Therefore, it may reduce the amount of error to include all components as fitting parameters (or fitting coefficients). There are six parameters, or coefficients, for which the algorithm may do a fitting; they are: b, m, K, α, R, and C.

In the fitting routine, the parameters are found in stages. The first stage finds values for m, b, and K and uses values based on component values for α, R, and C. After this step, a 6^{th} order polynomial, in frequency, is fit to the resulting values of m, b, and K to obtain more smooth, realistic values for those parameters. The result of this step for payload 29.036 is seen in fig. 4.1 with R and C being used to calculate Z_f from eq. 3.2, in the second panel on the right with both magnitude and phase. The value of α is shown in the top, right panel. The fit values for b, m, and K are seen in the left, top two panels along with the resulting polynomial fits for each where the polynomial fits are dashed lines. Also in the same figure are the values of the other parameters and the match (dashed lines) to the non-saturated resistive and capacitive standards (solid lines), third panels on left and

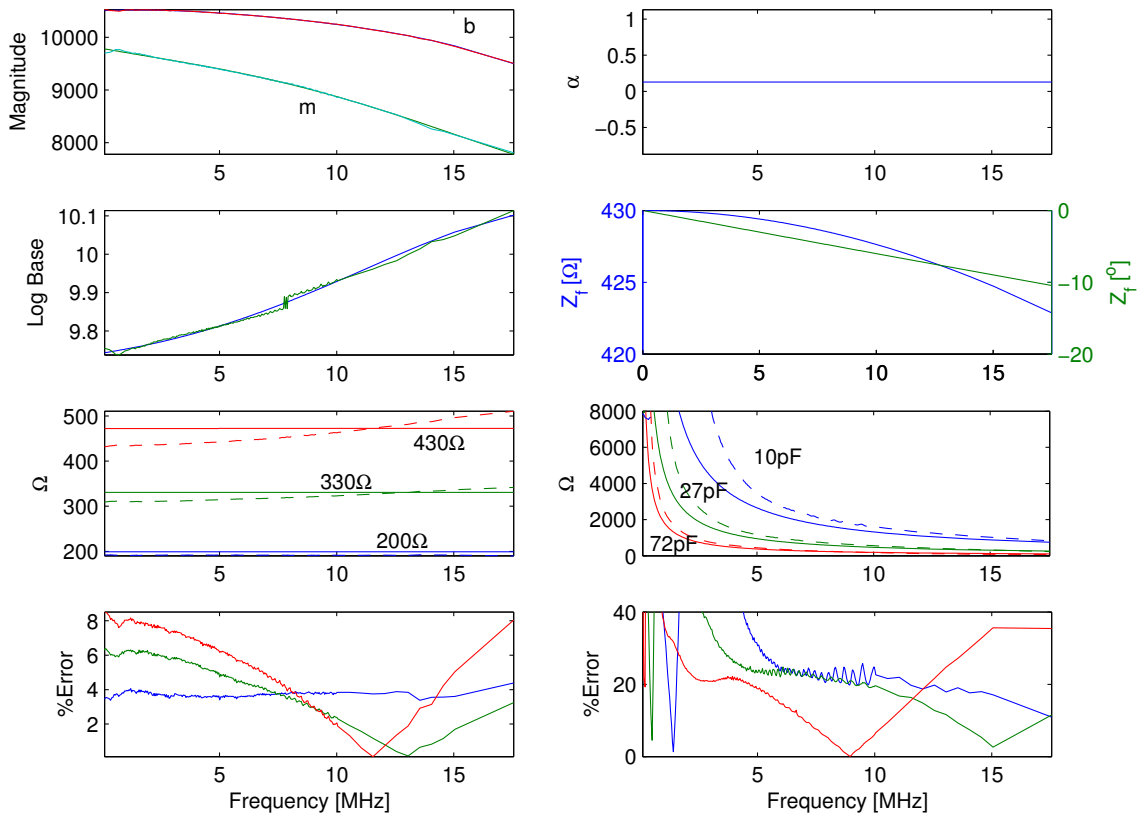

Fig. 4.1: Fitting results for stage 1 with the fitting for b, m, and K and assumed values for α, R and C.

right, with the error introduced by them, bottom panels on both left and right. After this stage it the error for capacitive loads seems to increase with decreasing capacitance. Since the flight data will have capacitance less than the 10pF calibrator standard the error at the end of this first stage will be about 30%.

The second stage of the fitting routine finds values for the coefficients α, R and C while using the polynomial fit values for the coefficients found in the first stage. After values for α, R, and C are found, a 6^{th} order polynomial, in frequency, is fit to the results for each of the coefficients to smooth those results. The error introduced by the nonsaturated loads after the final fitting for the six parameters may be seen in the bottom two panels of fig. 4.2 with the values for the coefficients are seen in the top four panels of the figure. Note that the error for a small capacitive load (less than 10pF) above 3 MHz is less than 5% for both payload SIP units. This directly corresponds to the expected range where the data will be

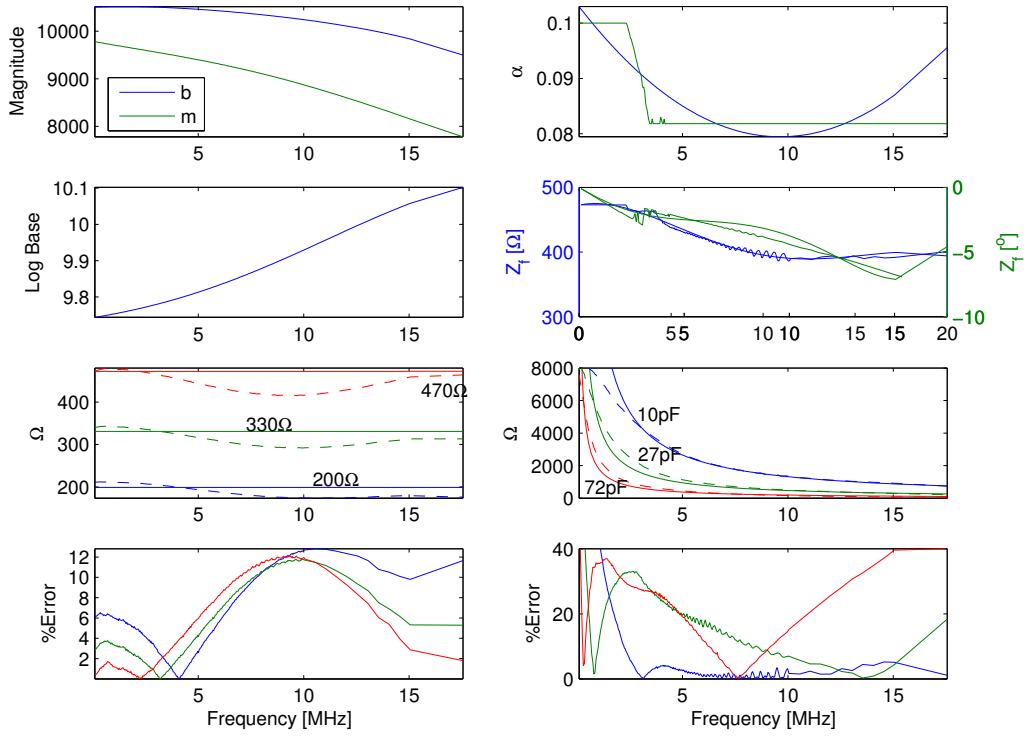

Fig. 4.2: Final error introduced by the calibration coefficients for payload 29.036.

capacitive. Figure 4.3, in the same format without the intermediate steps, demonstrates that the final calibration error for payload 29.037 is similar to that from payload 29.036.

4.2 Ionospheric Plasma Fitting Results

Figures 4.4 and 4.5 demonstrate the calibration application results. PCM data for several in-flight sweeps where there is some level of plasma with the corresponding impedance values, after calibration, are shown in those figures. The low altitude sweeps (low density) approach a free space measurement and thus look very much like an ideal capacitor. The sweeps at higher altitudes (higher densities) have large deviations from this ideal capacitor than do the low altitude sweeps. Note that each impedance sweep has a frequency above which the sweep is capacitive (downward sloping) and this capacitance decreases (slightly higher impedance) with increasing plasma. This decrease in capacitance is contrary to intuitive thought but it is clearly evident in the bottom half of fig. 4.4 above 9 MHz as a vertical impedance shift in the sweeps at 420 km in comparison to the lower altitude sweeps. This

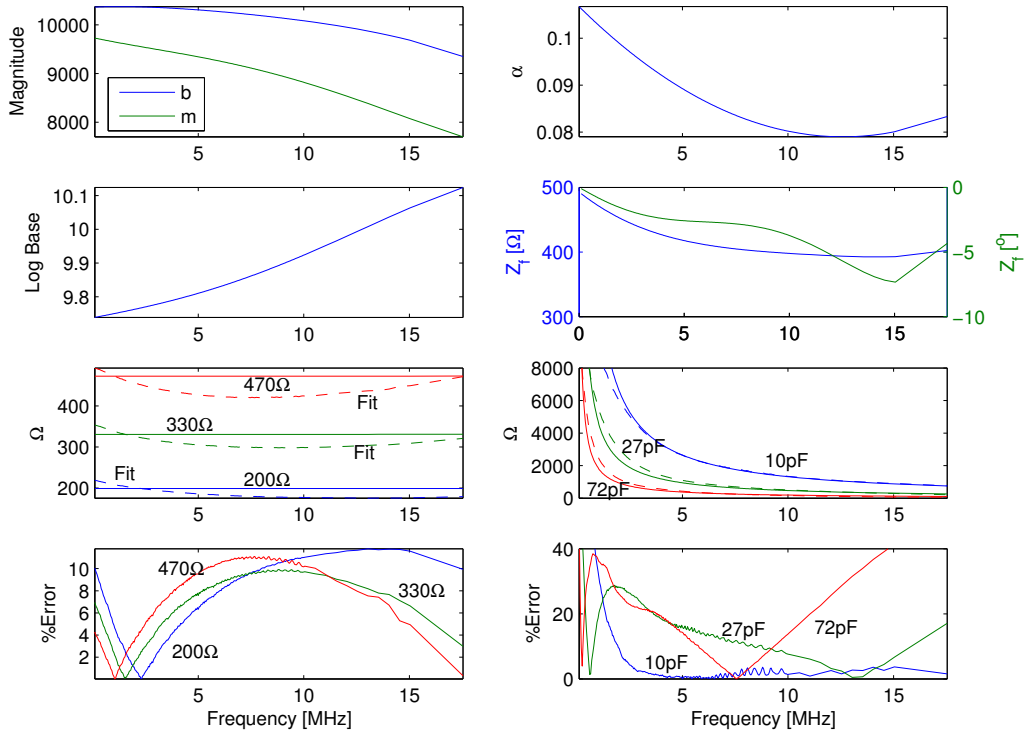

Fig. 4.3: Final error introduced by using the calibration coefficients for payload 29.037.

capacitive area is expected and is the region where the calibration will yield the error from the coefficient fitting.

The poles due to the denominator of eq. 3.13, mentioned in section 3.1.2, are corrected by adjusting some of the calibration coefficients. The poles are independent of R and C but dependent on the other four coefficients. Once the calibration coefficients are found with minimal error, they are used to find the PCM values of the poles using eq. 3.16 and compared to the flight data to verify the flight data does not cross the PCM value of this pole line. For the 29.036 data the calibration coefficients could not be adjusted sufficiently, still with small error, to completely correct for the introduced poles. However, the data from payload 29.036 for the resulting calibration coefficients does not cross the denominator pole line but it does approach it. This is seen as the spike in the impedance values in the high altitude (high density) sweep in fig. 4.5. For payload 29.037 the data does not approach the pole line (called ¨denominator line¨ in the figures) and thus the affects of the pole are minimized, see fig. 4.4.

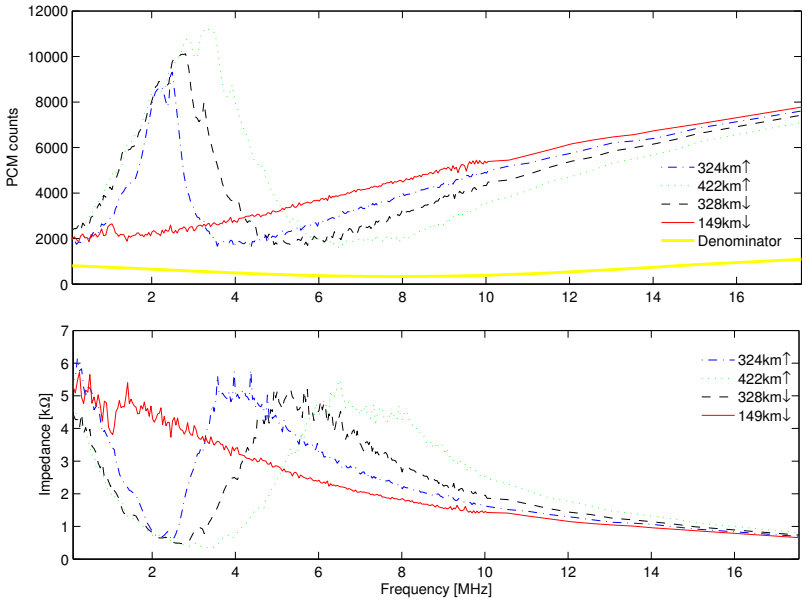

Fig. 4.4: Results of converting data from payload 29.037 in units of PCM counts to impedance.

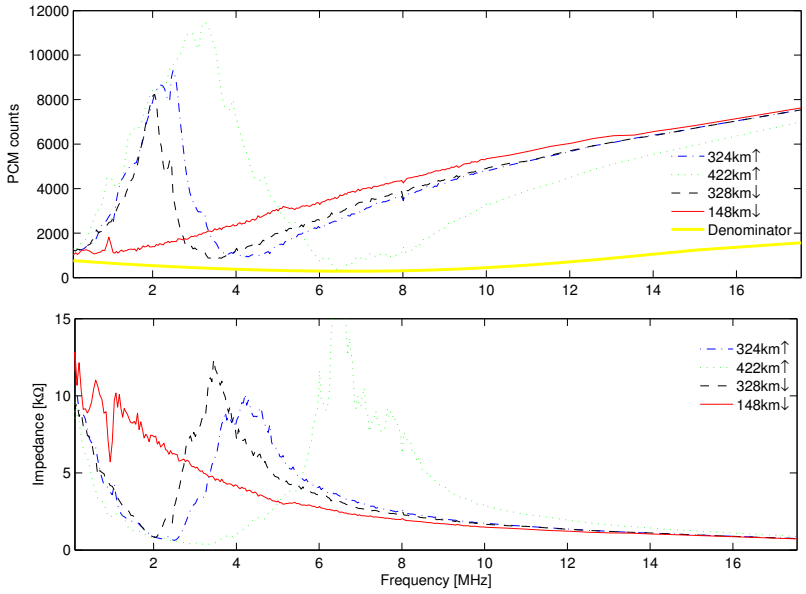

Fig. 4.5: Results of converting data from payload 29.036 in units of PCM counts to impedance.

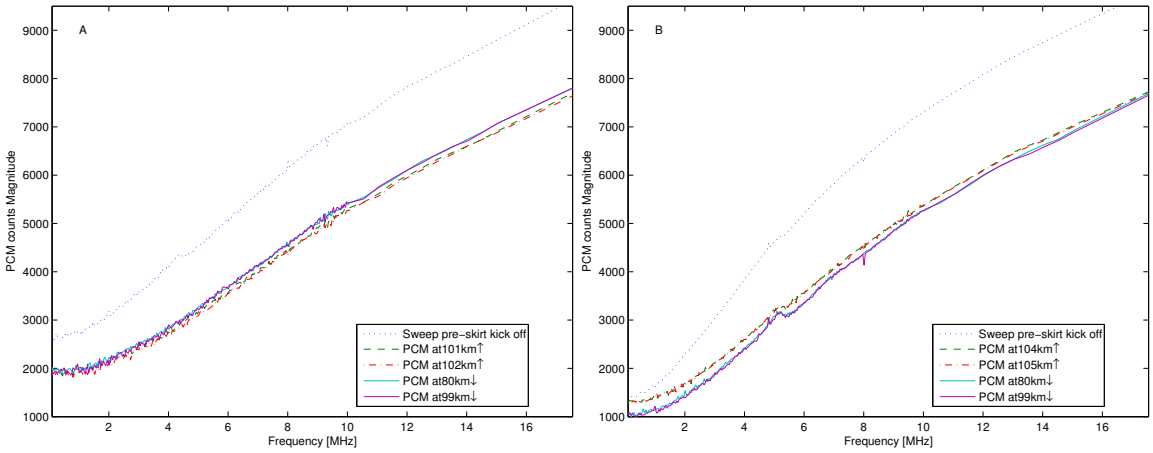

Fig. 4.6: Looking at up-leg and down-leg sweeps for finding Z_0. (A) is for payload 29.037 and (B) is from payload 29.036.

4.3 Free Space Fitting Results

To fit Balmain's theory [19] to the impedance data, see chapter 5 for fitting, the free space impedance of the SIP antenna needs to be known. Since a true measurement of the free space impedance must be made with the payload at several wavelengths from the nearest object (30 m to 6 km)including restraining devices, this can not be measured in a lab environment. Therefore, the only true free space impedance values come from flight data. This free space impedance, Z_0, is from an in-flight sweep where there is no plasma, i.e. a low altitude sweep. The free space impedance sweep for each payload will be first analyzed in PCM counts and then converted to impedance for use in normalizing the flight data.

For the Equis-II rocket flights, the skirt of the rocket covering the monopole antenna did not kick off until about 100 km on the up-leg portion of the flight, see fig. 1.4. At this altitude there may be some plasma so the up-leg portion is not as easily used for finding Z_0 as a sweep from the down-leg portion of the flight. Several sweeps from both the up-leg and down-leg will be compared to find a suitable free space sweep. A sweep from between about 101 km to 105 km will be used for the up-leg portion and for the down-leg a sweep from about 80 km will be used, fig. 4.6. The sweeps in fig. 4.6 from before the skirt was kicked off shows that there was a large influence, as expected, of the skirt on the measurement.

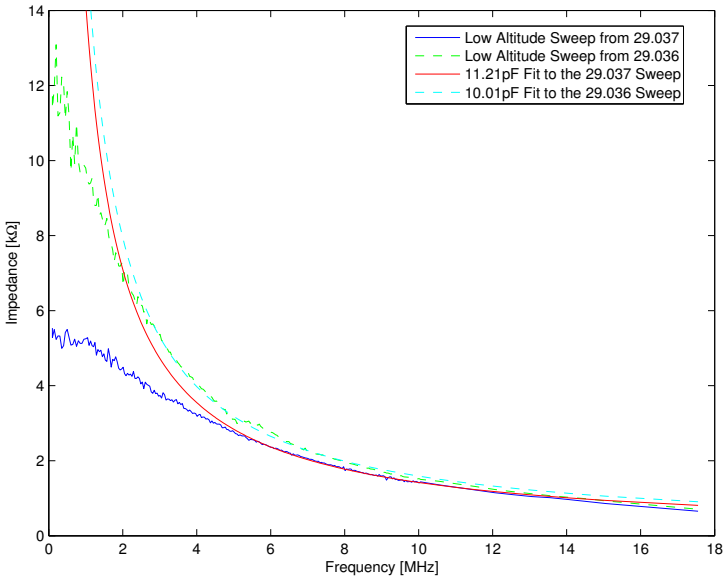

Fig. 4.7: Free-space impedance at low altitude on the down-leg from payloads 29.037 and 29.036 along with ideal capacitors fit to each.

The process of finding a free space sweep should have been a very simple process. The sweeps from the up-leg should match those from the down-leg. However, this is not the case and the up-leg sweeps do not match the down-leg sweeps for both payloads, see fig. 4.6. This means that the free space measurement was changing with time during the flight. At this time, there is no explanation for this change of the in-flight data. One method to circumvent this change is to use the up-leg free space sweep to normalize the up-leg data and the down-leg free space sweep to normalize down-leg data.

Also noted from fig. 4.6 is that the PCM values of the free space sweeps do not match across payloads. The values of the free space sweeps for payload 29.036 below about 2 MHz are about 1000 PCM counts and those for payload 29.037 in the same range are about 2000 PCM counts. To enable further analysis of what caused this difference, one of the free space sweeps for each payload are converted to impedance. The impedance of ideal capacitors are then fit to each low altitude impedance sweep, shown in fig. 4.7. This fitting results in a capacitive value of about 10pF for payload 29.037 and about 11pF for payload 29.037.

It is important to note that the low frequency data, below 4MHz, does appear to be small in impedance values when compared to the impedance of an ideal capacitor, see

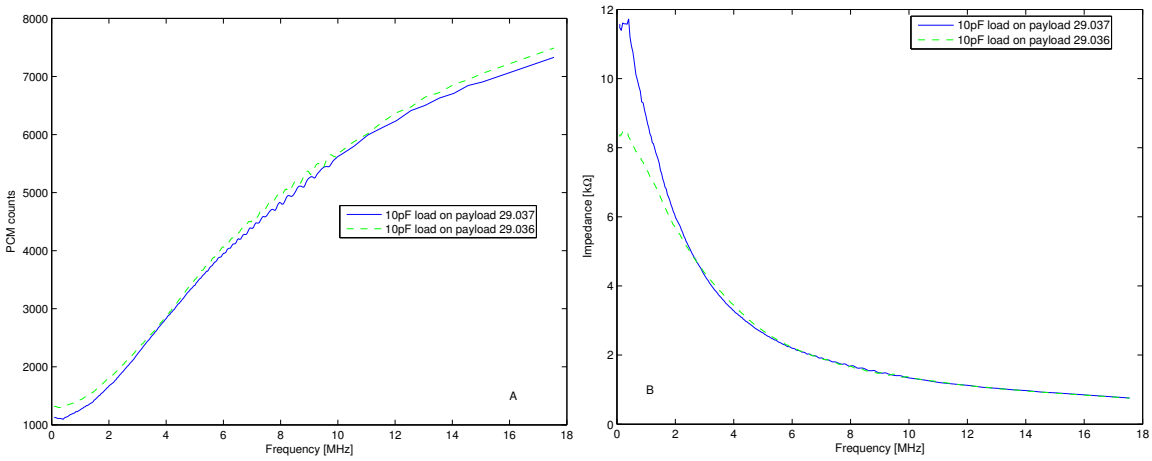

Fig. 4.8: Small capacitive load, 10pF, measured on both payloads. (A) is the calibration load raw data in PCM counts and (B) is the same data but with the calibration applied in impedance.

fig. 4.7. This is due to the error in the circuitry at low frequencies. This error is due to the unfortunate fact that α has a large influence on the recorded PCM data when the antenna impedance, $|Z_a|$, is high. Because of this influence of α, $|Z_a|$ can not be backed out via the calibration at these low frequencies.

Since the free space sweeps have a capacitance of about 10pF the calibrator standard of that value may be used to look at any differences in pre-flight data. The 10pF capacitor standard observations on the SIP for each payload are plotted in fig. 4.8(A). Those sweeps are also converted to impedance to look at differences after calibration, fig. 4.8(B). The large differences between payloads of the in-flight data is not evident in the pre-flight observations. This indicates that there is some change that occurred to the payloads between lab measurements and flight.

An explanation for this difference in the measurements made on the same payload is that there was more capacitance, shunt capacitance, introduced sometime between lab calibration and launch. This could possibly be an internal cable being bent to sharp or pinched in either re-assembly, transportation or flight. This could also be from the fact that to perform the calibration each antenna was removed from the payload body and a short cable with alligator clips was used to connect the calibration standard to the unit.

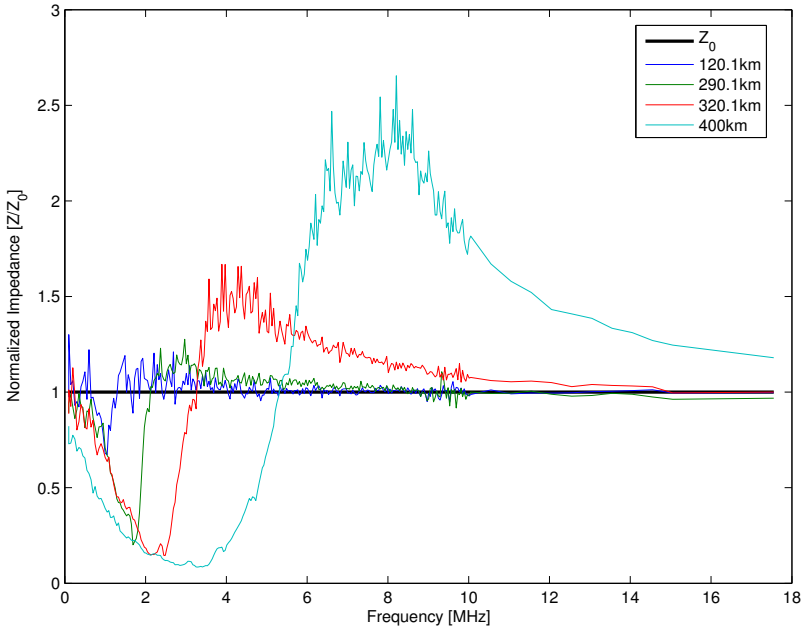

Fig. 4.9: Several sweeps from payload 29.037 in impedance normalized by Z_0.

The antenna was then re-attached. In this re-attaching the cables had to have been moved and some change in the unit is certain.

Figures 4.9 and 4.10 contain up-leg sweeps at various altitudes from each payload normalized by Z_0. The sweeps in the figures were chosen to demonstrate various amounts of plasma and the effects of the plasma on the sweep. It is interesting to see the large amounts of deviation in the dense plasma sweeps from the free-space value in the normalized data.

4.4 PFP Calibration

In flight, the frequency measured by the PFP is digitized and sent to the ground station. For the flights 29.037 and 29.036 data was sent in two 16 bit pieces, one being the top 16 bits of the frequency and the other being the bottom 16 bits. Those two pieces are then recombined during data processing. The PFPs were each driven by a chip 24 MHz chip up-sampled six times. Thus there is a calibration, consisting of only a small calculation, to get to the frequency from the ground recorded data. This is found in eq. 4.1 for Equis II and will vary per instrument design.

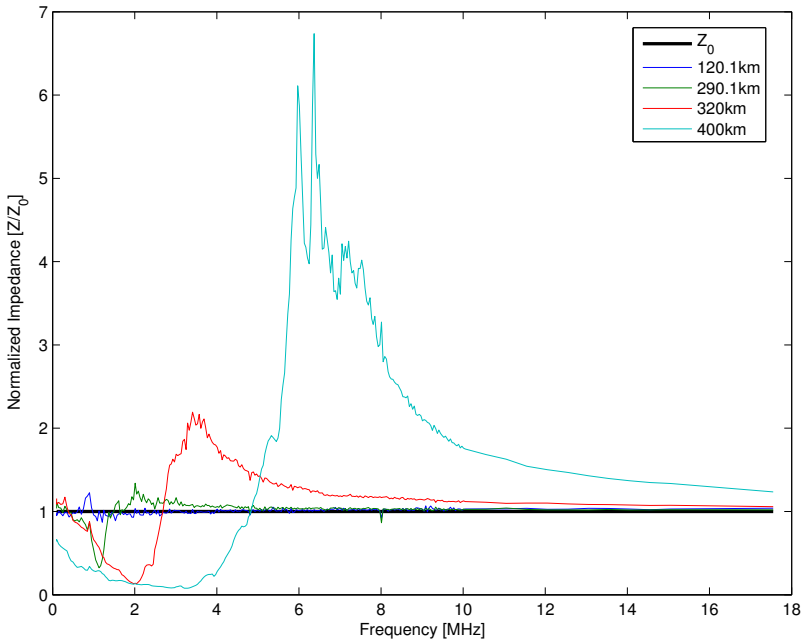

Fig. 4.10: Several sweeps from payload 29.036 in impedance normalized by Z_0.

$$f_{PFP} = \frac{144e6 * data_{PFP}}{2^{32}} = f_{uh} \tag{4.1}$$

The PFP is designed to lock onto the zero phase point in the antenna impedance. When not locked the unit continually scans in frequency, either up or down, until it is able lock onto the zero phase point [10]. The lock will only occur when the electron density is sufficiently large. Sometimes the density may become high enough as to put the system into saturation, in which case the unit will come unlocked and continue scanning. One method for determining PFP lock used was simply using a standard deviation over several data points; if the resulting standard deviation was smaller than 2x the frequency step then the unit was locked and the frequency measured is usable. However, this did not yield desirable results as too much data from the unit in tracking mode is still present after application. Although this is useful for visualizing the data or an initial estimate of when the unit is locked.

Another method used to find when the PFP data, or the unit, is locked is by using the reset of the unit. Each PFP unit was designed to reset to a start frequency of about 6

MHz once the tracking frequency reached either it's design upper or lower limits [10]. Thus while searching to lock onto the upper hybrid there will be a sudden jump or discontinuity in the unlocked data when the unit resets. This will happen at regular intervals in the data while the unit is searching and at very large intervals once the unit is locked onto the upper hybrid. Using this reset allows for more of the data from the tracking mode to be rejected.

Chapter 5

Electron Density from the PIP

The purpose of the PIP was to measure ionospheric electron density. The SIP data is analyzed by fitting Balmain's model of the impedance of an antenna in a plasma to the observed impedance data. For the PFP, electron density is found through analysis of the measured upper hybrid frequency. This analysis procedure and results are presented in this chapter. The resulting density profiles from both PIP instruments and from the sweeping Langmuir probe (SLP) are compared to assess the validity of the individual calibrations, measurement methods and instrument error.

5.1 Electron Density from the SIP

The SIP flight data, in units of PCM counts, is converted to impedance by applying the calibration equation, eq. 3.18, with the coefficients developed in chapter 4. The data and the model are normalized by their respective free space values before they are fit to each other, where The data is normalized by Z_0, as determined by data taken when the payload is not in ionosphere plasma and the model is normalized by an evaluation of the model for electron density near zero. These normalized quantities are generally proportional to the plasma relative dielectric strength. The Balmain model parameters are adjusted until the residuals, Γ, in eq. 5.1 are minimized. The MATLAB LSQC function is used to optimize the model parameters to find the minimum error fit.

$$\Gamma = \sum_{k=1}^{n} \left(\frac{|Z_a|}{|Z_0|} - \frac{|Balmain(\omega_{p_k}, \omega_c, \nu, R, L)|}{|Balmain(0, \omega_c, \nu, R, L)|} \right) \tag{5.1}$$

The Balmain model parameters are ω_p, ω_c, ν, θ, R, L, and R_{sheath}. Two of the parameters, θ (orientation to the magnetic field) and R_{sheath} (sheath radius), are assumed

to be zero because they only affect the model below the upper hybrid frequency. The antenna radius is R and it's length is L which are both known quantities of 1.43 cm and 48.9 cm, respectively. The cyclotron frequency, ω_c, is dependent on the magnitude of the local magnetic field. The magnetic field strength varies with altitude and is known by the IGRF model [20]. The collision frequency, ν, is found using neutral densities and the collision cross-section for the various gasses from the MSIS model [1, 21]. Both the IGRF model and the MSIS model are well documented and widely accepted as standards in their respective areas. The plasma frequency is ω_{p_k} and is dependent on the electron density and is the parameter varied by the fitting routine until a best fit is found. Once the model is fit to each sweep, electron density, ρ_e, is calculated from the plasma frequency by eq. 5.2. An electron density profile is built up by analysis of each sweep along the flight path.

$$\rho_e = \frac{\omega_p^2 m_e \epsilon_0}{e^2} \tag{5.2}$$

Not all of the sweep data points were used in fitting the model to the data. There are fewer data points at the higher frequencies, above 10 MHz, than at frequencies below. The frequency step between the lower frequency data is 40 KHz, between the higher frequency data is 0.5 MHz with the exception of the last data point being spaced at 2.5 MHz from the previous data point. There were ten points in the data and the frequency below 10 MHz that were centrally averaged such that the resulting averaged data was spaced at 0.5 MHz. The data above 10 MHz was used without any averaging. This is done so that the high frequency data (above 10 MHz) would have as much influence as the data points below 10 MHz in the fitting routine. The lower frequency bound of the region of data used in the fitting routine was shifted to match the change in the plasma density, as noted comparing fig. 5.1 to fig. 5.3 by the small circles, while the upper bound remained constant. The minimum frequency used, the lower bound, was 4 MHz below an altitude of 295 km leaving a total of 25 data points used in the fitting routine. Above this altitude the minimum frequency used was 9.5 MHz yielding a total of 13 data points for the fitting routine. The data points used in the fitting are seen as the small circles in fig. 5.1 through fig. 5.6. This

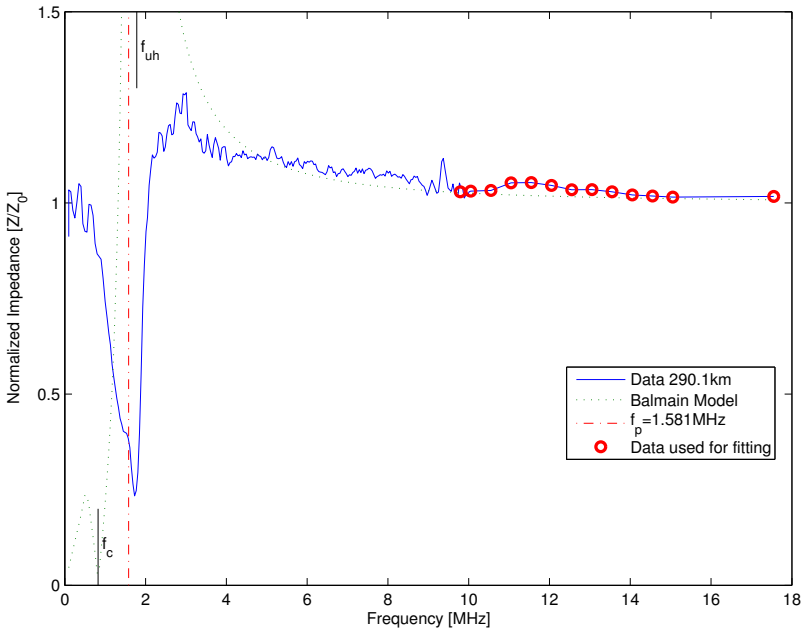

Fig. 5.1: Balmain model fit to data from payload 29.037 on the up-leg at about 290 km.

process is unable to resolve densities below about 2×10^3 $[N_e/\mathrm{cm}^3]$ due to the smaller signal to noise ratio at low densities and the larger error in the calibration at the low frequencies.

An example curve showing the fitting and results is presented in fig. 5.3. In this figure the normalized data from payload 29.037 at about 400 km in altitude, where the plasma is dense is presented as the solid line and the normalized model fit as the dotted line. The fit is only valid above about 9 MHz where the data is purely capacitive so the calibration error is minimal. Even though this is the only portion where the fit is important the remaining portion of the fit shows some interesting phenomena. As the data turns inductive near the R-L-C parallel resonance the model does not fit the data. This is due to a combination of the data having lower than expected values because of saturation and calibration error when the data is not capacitive. Also near the parallel resonance the Balmain model over predicts the changes in the normalized impedance [17]. However, in the data from payload 29.036 in high density plasma, seen in figs. 5.5 and 5.6, an additional error is introduced into the data by the calibration equation poles, seen as the peaking in the data near the parallel resonance. In the data near the series R-L-C like resonance the model does not

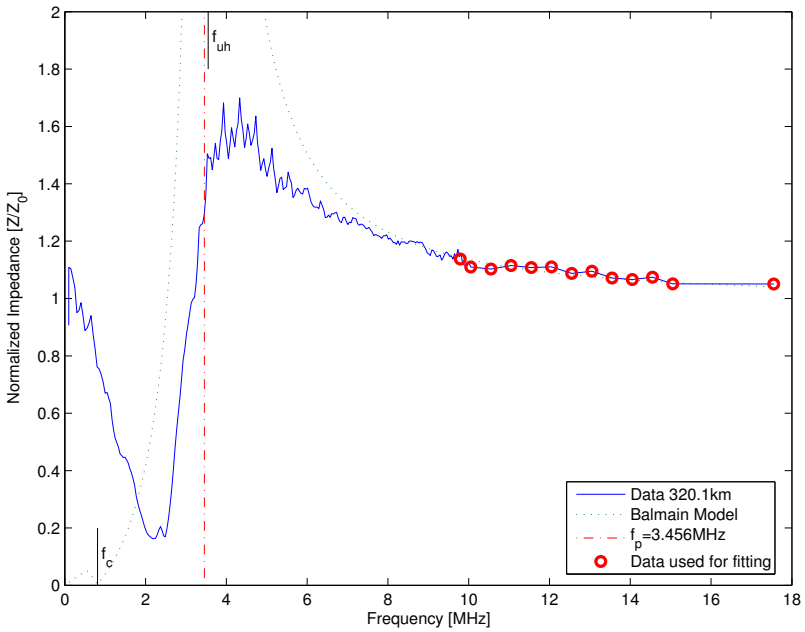

Fig. 5.2: Balmain model fit to data from payload 29.037 on the up-leg at about 320 km.

fit the data due to the higher error in the calibration at low frequency and the fact that the fitting uses the assumption that the sheath is negligible. The result of the fitting is the plasma frequency which is presented as the vertical line located appropriately along the frequency axis.

In principle, this procedure to get electron density may be improved by using a better model [17,22] or by having more data points at the higher frequencies and by having a better signal to noise ratio. The signal-to-noise ratio in the data is crucial to fitting lower density sweeps. The data points slightly above the upper hybrid frequency are very important for finding electron density as they are well calibrated by being capacitive and undergo a strong response due to the plasma.

5.2 Electron Density from the PFP

The PFP attempts to track the frequency at which the phase of the antenna impedance is zero [10, 23]. This zero phase corresponds to the upper hybrid frequency, ω_{uh}, is defined in eq. 5.3.

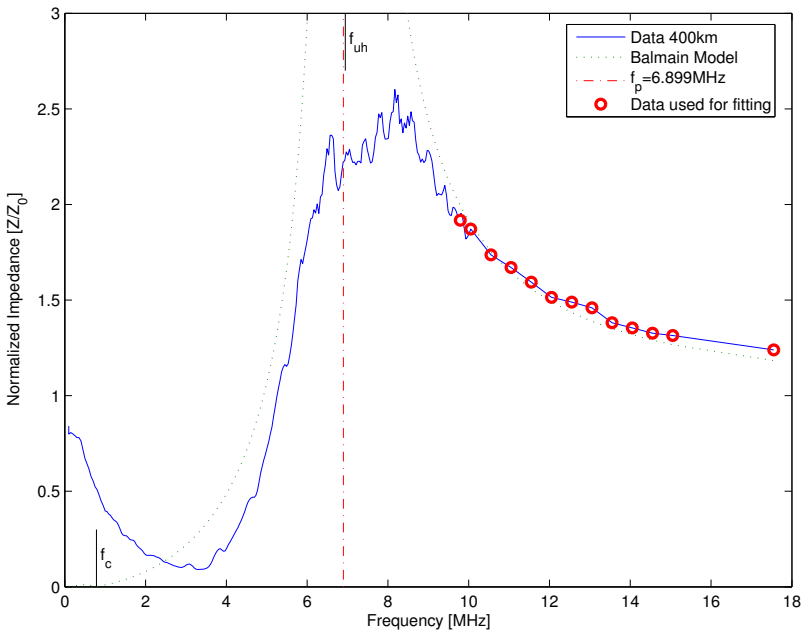

Fig. 5.3: Balmain model fit to data from payload 29.037 on the up-leg at about 400 km.

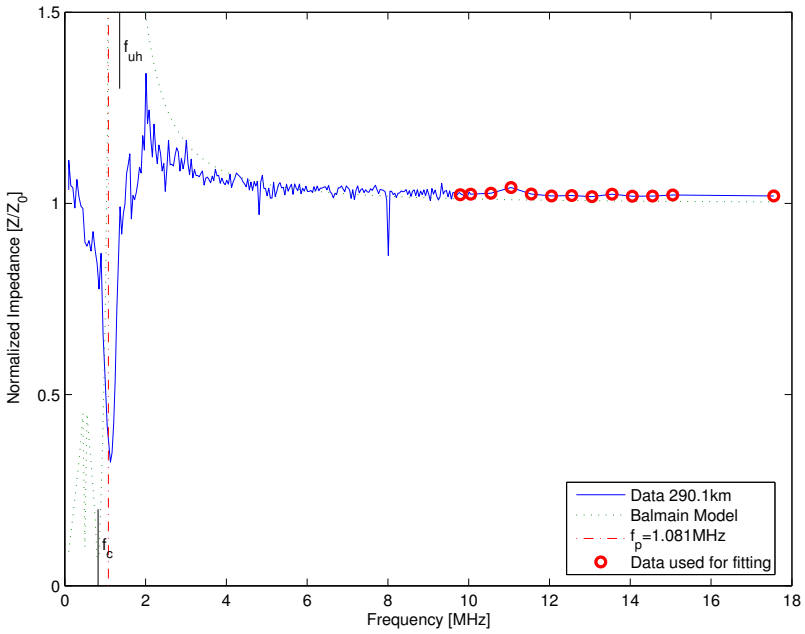

Fig. 5.4: Balmain model fit to data from payload 29.036 on the up-leg at about 290 km.

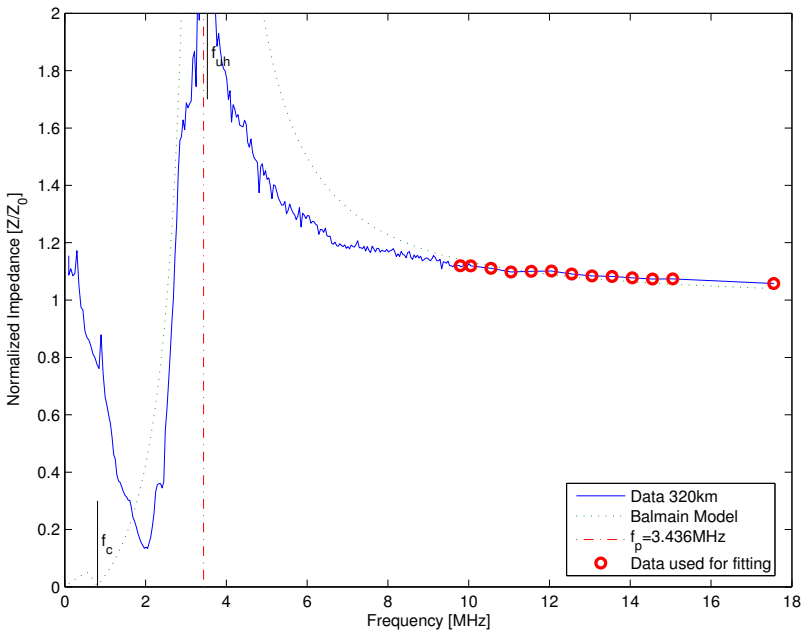

Fig. 5.5: Balmain model fit to data from payload 29.036 on the up-leg at about 320 km.

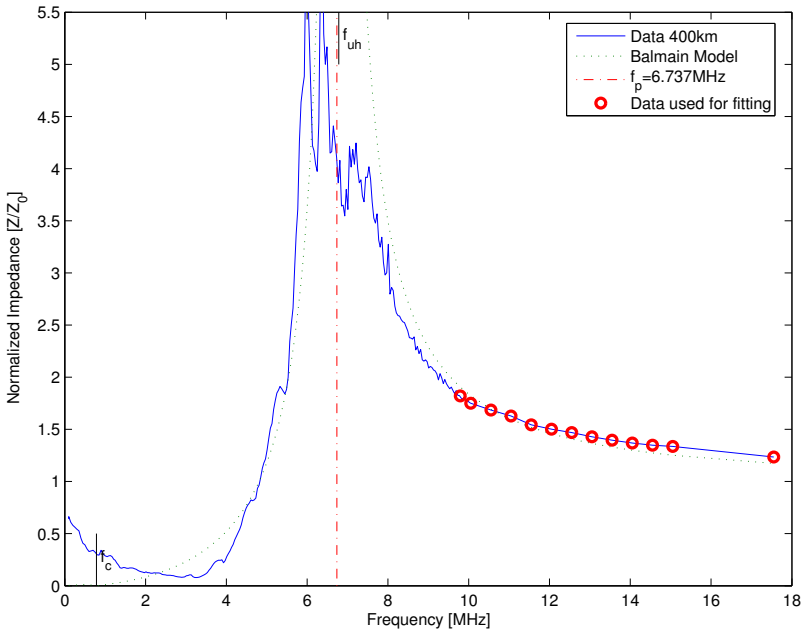

Fig. 5.6: Balmain model fit to data from payload 29.036 on the up-leg at about 400 km.

$$\omega_{uh}^2 = \omega_c^2 + \omega_p^2, \tag{5.3}$$

$$\omega_c = \frac{|B|e}{m_e}, \tag{5.4}$$

$$\omega_p = \sqrt{\frac{\rho_e e^2}{\epsilon_0 m_e}}, \tag{5.5}$$

where ω_c is the cyclotron frequency, ω_p is the plasma frequency, $|B|$ is the magnitude of the magnetic field [Teslas], e is the charge on an electron [Coulombs], m_e is mass of an electron [kg], ϵ_0 is the free-space permittivity [F/m], and ρ_e is the electron density [N_e/m^3]. The upper-hybrid frequency, ω_{uh}, is simply the frequency from the PFP data, eq. 4.1, converted to units of rad/sec. Combining eq. 4.1 and eq. 5.5 and solving for the density as a function of the PFP data results in eq. 5.6.

$$\rho_e = \epsilon_0 m_e \left[\left(\frac{144 \times 10^6 \ PFP}{e \ 2^{32}} \right)^2 - \left(\frac{|B|}{m_e} \right)^2 \right] \tag{5.6}$$

5.3 Electron Density Results

A comparison between the PFP electron density and SIP electron density profiles are presented in fig. 5.7 through fig. 5.10. Electron density from the sweeping Langmuir probe (SLP) is also included here as an independent instrument for comparison. The electron density data is plotted on a log x-axis so the variations in the small scale data may be seen more clearly along with the variations in the large scale data. The SLP data was processed to obtain electron density by Aroh Barjatya and result from the electron saturation current observations [24]. If the data from all the instruments is similar then the density profiles may be used with confidence. In each density profile figure the SIP is plotted as the solid line, the PFP as the dashed line and the SLP as the dash-dot line. The SLP provides a good relative measurement of electron density. It is a difficult instrument to calibrate in an absolute sense due to problems with surface contamination and probe geometry effect. These geometry effects are due to the plasma sheath and to the capped cylinder used for

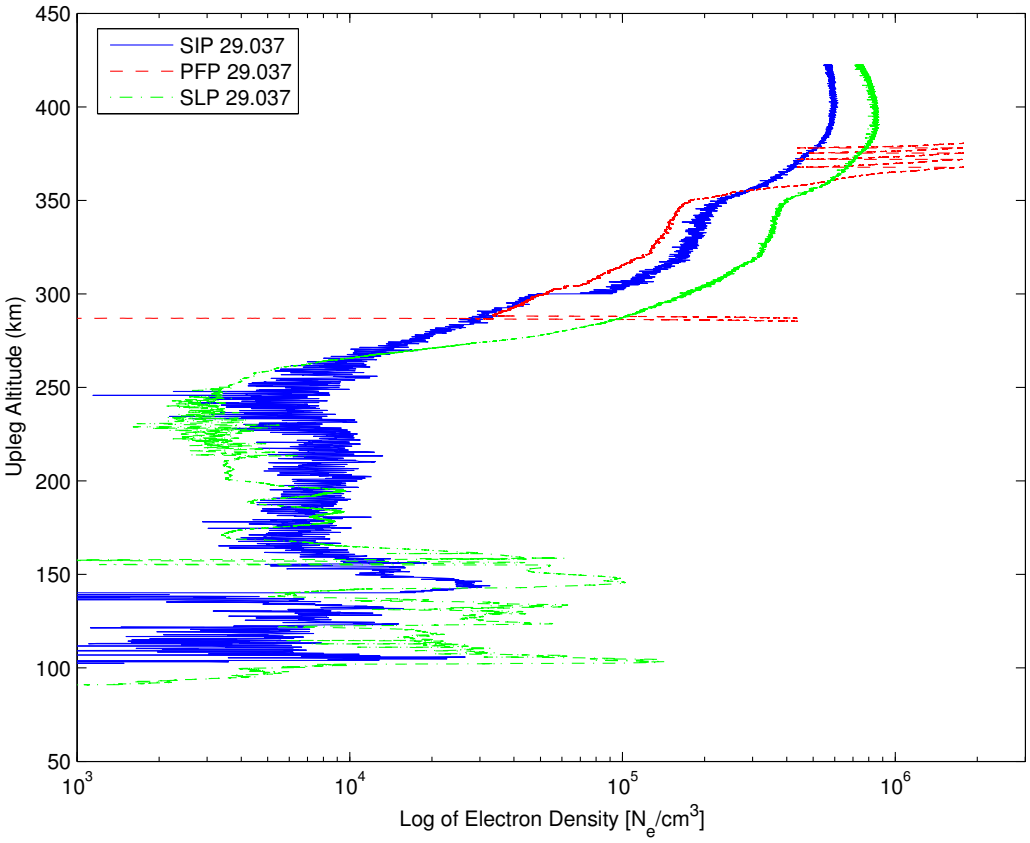

Fig. 5.7: Electron density from the up-leg portion of payload 29.037 for both the SIP and the PFP.

the sensor instead of a section of an infinite cylinder. Thus a factor of 2 or more difference to the SIP and PFP is not unexpected [25]. The SLP data is generally normalized to the PFP data and is used to extend the measurement range to lower altitudes and densities. However, there is an obvious error in the PIP phase measurement, which the PFP uses, resulting in unreliable PFP densities for plasma frequencies above about 6 MHz. This error was extreme at frequencies above 7 MHz as presented in chapter 2. At the higher densities, altitudes above 320 km, the resonant frequency approached 7 MHz and higher, therefore the PFP data is suspect. Eventually, the phase error resulted in the PFP losing lock at high densities. The SIP analysis is considered to be the most accurate in both an absolute and relative sense of the three measurement techniques presented in these figures.

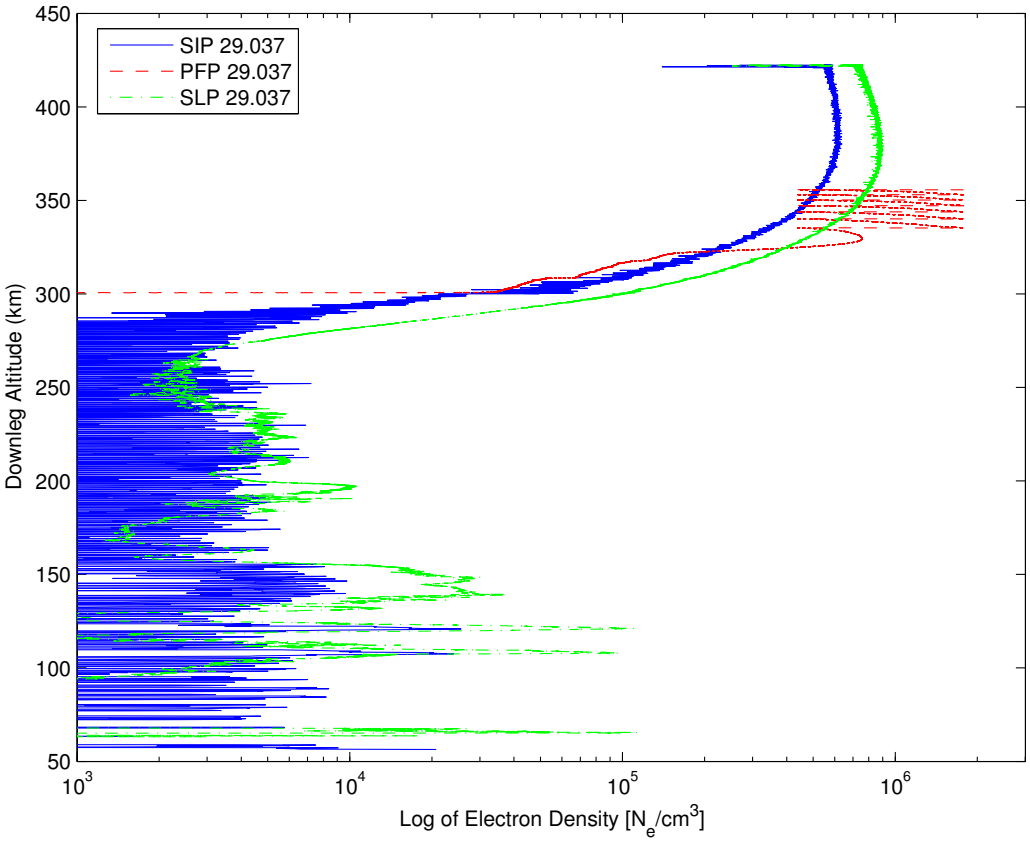

Fig. 5.8: Electron density from the down-leg portion of payload 29.037 for both the SIP and the PFP.

5.3.1 Payload 29.037 Electron Density Results

For payload 29.037, the up-leg densities are presented in fig. 5.7 and the down-leg densities in fig. 5.8. There are differences between the up-leg and the down-leg data and this is expected as the horizontal distance between the two observations is over 50 km. The low altitude densities from the SIP are dominated by some wide variations in the data below a density of about 10^4 N_e/cm^3. This can be largely attributed to the fitting routine and its decreased ability to distinguish the lower densities previously discussed. However, the basic trends are still seen when compared to the SLP data as well as several low altitude layers with densities above 10^4 N_e/cm^3.

The PFP instrument for this 29.037 payload at higher altitudes, corresponding to higher densities, lost lock on the upper hybrid frequency. At these higher altitudes the

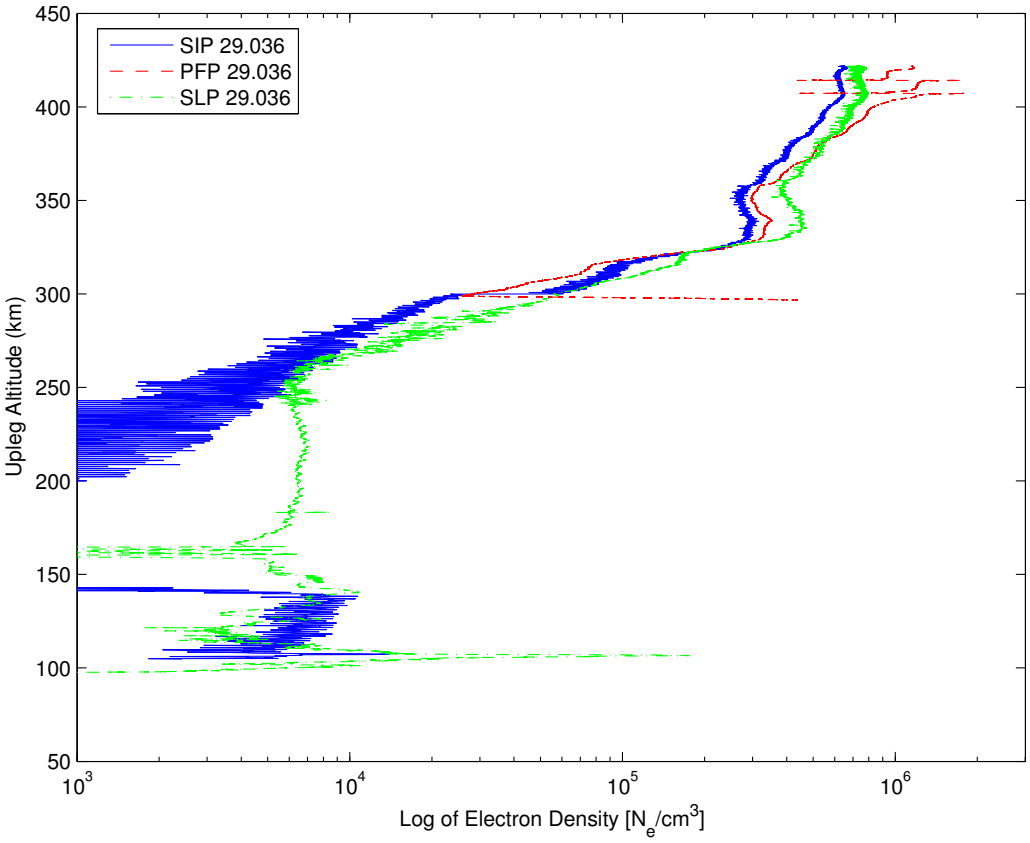

Fig. 5.9: Electron density from the up-leg portion of payload 29.036 for both the SIP and the PFP.

instrument, while tracking, reached the frequency limits and, as it was designed to do, reset to a frequency of 6 MHz. At this frequency the instrument began to track to find the zero phase but due to the error in the phase measurement it was never found and the PFP reset once reaching the frequency limit. Thus, high altitude data from the PFP for payload 29.037 is lost. This unlocking of the PFP was difficult to determine in analysis and is evident by the small set of cyclic data at about 350 km.

5.3.2 Payload 29.036 Electron Density Results

Electron density profiles for payload 29.036 may be seen in figs. 5.9 and 5.10. The density profiles for up-leg and down-leg are not the same with even greater differences than those evident from the payload 29.037. The phase measurement leading the PFP data

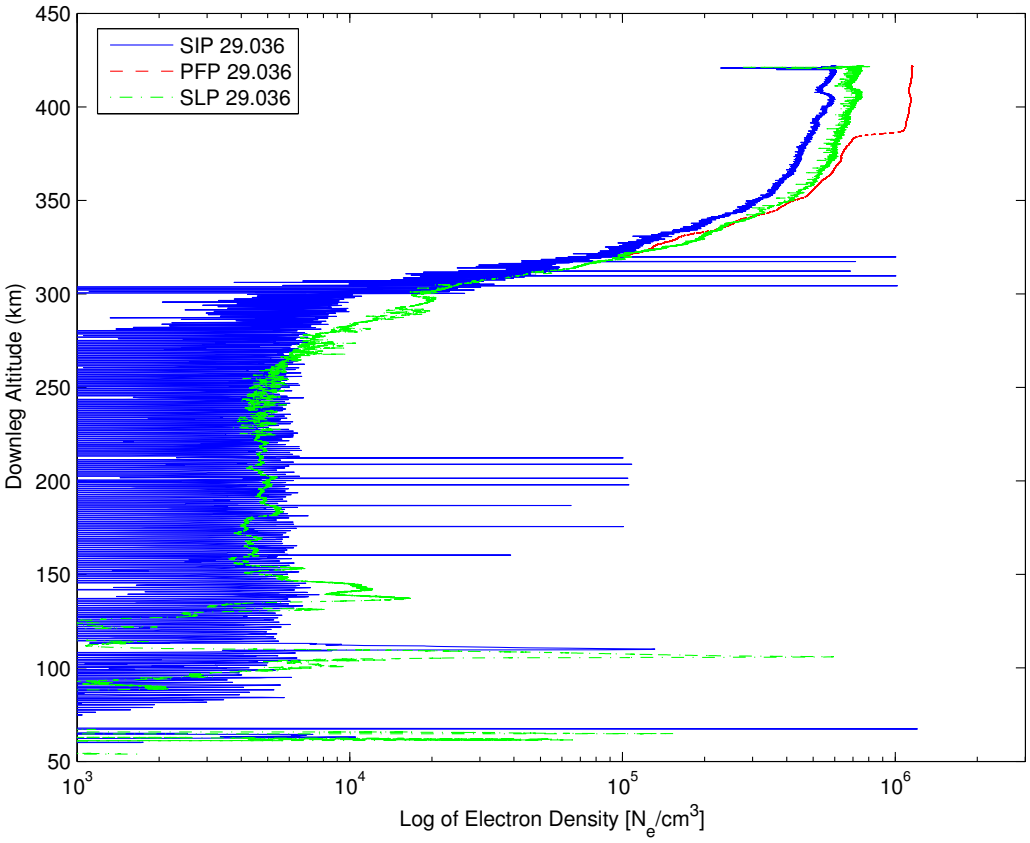

Fig. 5.10: Electron density from the down-leg portion of payload 29.036 for both the SIP and the PFP.

appears to be less erroneous for this payload than it was for payload 29.037 and the PFP functioned somewhat better. The difference between the PFP and the SIP in the up-leg between about 290 km and 310 km is unexpected. This is the region where the data is expected to most closely match. However, at altitudes slightly higher the two do match very well. The reason for this is not understood.

Chapter 6

Conclusion

This chapter will discuss application of this work to other programs, opinions on how to improve the calibration process and suggestions for improvement of the PIP instrumentation.

6.1 Application to Other Projects

The calibration presented herein has direct application to five other PIP units of a similar build. The E-winds campaign used four PIP units and flew from the Wallops Island NASA facility in Virginia. These instruments have the same fault in the phase. The instrument is yet uncalibrated and the data is unprocessed for electron density [10]. A successful calibration for these four instruments may be established using the same process presented herein of separating the magnitude measurements from the phase measurements. This same process has application to the PIP unit on the FPMU [12, 23]. This is the same unit that was calibrated by Kurra. It has yet to be installed on the ISS. This process may be used to get usable and important electron density measurements from the FPMU.

6.2 Suggested SIP Calibration Improvements

Improvements to the SIP should be made with the idea in mind that the SIP is a flying network analyzer and should be precise. Lab measurements should be made in controlled environments with attention paid to details and documenting those details. All care should be made in the design and building of the SIP so that leakage currents are minimized and components are very well isolated and/or shielded. These improvements will contribute to increasing the signal to noise ratio and thus enhancing the quality and reliability of the impedance measurements.

The most important improvement to the SIP or the calibration process would be to have a better set of calibration standards. For example, standards of about 0.5pF, 1pF, 5pF and one that is very close to the expected free space impedance of the antenna would be an improvement. Perhaps one possible load would be the antenna itself. Another example of better loads would be to reduce the error associated with the connection of the standard to the measurement device. This would mean to have the load embedded inside a device with a standard connector that is easily attached to a network analyzer as well as to the payload in place of the antenna. While there may be some error introduced by such a device the error may be calibrated out. Thus, noise introduced in the measuring process can be made negligible.

One improvement for the Equis-II SIP will entail improvement of the fit of the Balmain impedance model to the impedance data or by using a different model [17]. This model fitting would also be improved with a better method of finding the free space sweep.

Another important improvement is for the designers of future instruments, prior to building the circuit, to take the design and do some math. The derivation process and the circuit model equation can yield many insights to errors or phenomena (such as poles) that may not be obvious by looking at the circuit design or by testing. After having obtained a calibration equation the design may need to be adjusted slightly to account for any new insights.

Increased spatial resolution is another improvement for future probe designs. In other words, make measurements faster or more often as the unit flies through the plasma. In order to more closely measure plasma layers in the lower portions of the ionosphere more resolution is needed. In the data discussed herein plasma layers appear to have very sharp features. There are two explanations for those sharp features. The first being that is the actual character of the layer while the second is that the probe was not able to capture the details of the layer. Increasing the resolution would yield more detailed information.

Another improvement is to increase the frequency resolution, especially at the higher frequencies. Theoretically a frequency range from 10 KHz to 20.45 MHz with a constant

step size, yielding 512 data points, would work. This is, however, contrary to higher spatial resolution previously mentioned and a decision will have to be made by designers of future SIPs as to the specific variations of the instrument that meet requirements.

A manner in which to test the output measuring frequencies would be an improvement to future SIP units. The number of data points may be counted as well. Both the magnitude of each frequency and the number of them is important in the analysis and calibration of the SIP unit. I do not believe there is a need to measure the frequency of every point rather just the measurement of enough of the frequency point outputs to statistically verify that they are being output as designed.

Measuring the calibration standards on a well calibrated network analyzer at every frequency being used by the SIP unit (those measured from the previous paragraph) is another improvement that could be made to the calibration process of the SIP. This would mean using a network analyzer that is able to download the measured data to a computer as well as being in a temperature and humidity controlled environment. This would replace any error introduced by the three element model fitting to the calibration standards.

In the process of stripping the data from the raw files created by the ground station it was difficult to determine when there was lost data. A counter that counts each step of the SIP and resets at the end of each sweep would have greatly facilitated this process. Even a counter that simply incremented with the start of each sweep would have aided and sped up this process. Since the SFID, the sub-frame ID (see fig. 1.5), counter uses only three bits of the possible 14 bits, perhaps the top eleven bits could be used for such a counter.

The data processing herein started once the payloads were mangled and sitting at the bottom of the ocean; post flight. The SIP unit could not be taken back into the lab and have measurements or phenomena verified. The calibration process must start in the lab with measurements of the calibration standards. The impedance measured by each SIP unit should be verified against the values of the calibration standards before leaving the lab. Thus any concerns such as faulty phase information or too many data points may

be known, addressed and, if possible, fixed prior to being buttoned up for delivery. This process should be well documented.

6.3 Suggested Improvements for the PFP Instrument

The most important improvement to the PFP instrument is to fix the phase error in the instrument. This will allow the unit to not only track the zero phase point but more accurately measure it as well. This can be done by either using a different phase measuring chip or a completely different method of measuring.

The method used by the PFP unit to track the zero phase frequency is not well documented. In Carlson's thesis discussion only included general information about the control tracking loop and it's performance [10]. The performance of the control loop may be thought of as the ability of the control loop to accurately measure the frequency being limited by both the number of bits and the incrementation. The performance is also the ability of the control loop to dynamically adjust to fast changes to the system input, changes in plasma density. This should to be well documented as well as verified.

6.4 Summary

The SIP calibration should be precise and introduce minimal error to the data. The error introduced by the SIP calibration herein is small, under 5% for capacitive loads less than 10 pF above 3 MHz (see figs. 4.3 and 4.2). This range for good calibration results corresponds to the expected range of capacitive flight data. This error is significantly better than the error of the SIP on the FPMU which was reported to be 20% by Kurra [12].

The calibration of SIP and obtaining electron density may be summarized in four steps. The first step in the SIP calibration process is to measure the calibration standards on both the SIP and another device. This second set of observations serve as a reference to the SIP observations of the standards. The next step is to define and use a calibration model and determine values for the calibration coefficients. This is done fitting the SIP observations of the standards to the reference observations. Third, get the SIP flight data organized into individual sweeps as a function of time and altitude and apply the calibration equation

using the found values of the calibration coefficients to get impedance data for the entire set of SIP data. The final step is fitting the Balmain model to the now calibrated flight sweeps yielding electron density.

References

[1] R. W. Schunk and A. F. Nagy, *Ionospheres Physics, Plasma Physics, and Chemisty*, ser. Cambridge Atmospheric and Space Science Series. New York: Cambridge University Press, 2000.

[2] J. M. Goodman and J. Aarons, "Ionospheric effects on modern electronic systems," *Proceedings of the IEEE*, vol. 78, pp. 512–528, Mar. 1990.

[3] A. C. Tribble, *The Space Environment, Implications for Spacecraft Design.* Princeton, NJ: Princeton University Press, 1995.

[4] H. M. Mott-Smith and I. Langmuir, "The theory of collectors in gaseous," *Phys. Rev.*, vol. 28, p. 727, 1926.

[5] L. H. Brace, "Langmuir probe measurements in the ionosphere," in *Measurements Techniques in Space Plasmas, Particles.* American Geophysical Union, 1998.

[6] R. F. Pfaff, "In-situ measurement techniques for ionospheric research," NASA, Goddard Space Flight Center, Tech. Rep., Aug. 1996.

[7] K. G. Balmain, "The impedance of a short dipole antenna in a magnetoplasma," *IEEE Transaction on Antennas and Propagation*, vol. AP-12, pp. 605–617, Sept. 1964.

[8] K. G. Balmain, "Dipole admittance for magnetoplasma diagnostics," *IEEE Transaction on Antennas and Propagation*, vol. 17, no. 3, pp. 389–392, May 1969.

[9] M. D. Jensen and K. D. Baker, "Measuring ionospheric electron density using the plasma frequency probe," *Journal of Spacecraft And Rockets*, vol. 29, no. 1, pp. 91–95, Jan-Feb 1992.

[10] C. G. Carlson, "Next generation plasma frequency probe instrumentation technique," Master's thesis, Utah State University, Logan, 2004.

[11] S. Basu, J. Buchau, F. Rich, and E. Weber, *Handbook of Geophysics and the Space Environment*, ch. 10. Bedford, Mass: National Technical Information Service, 1985.

[12] K. Kurra, "Calibration of plasma impedance probe on the floating potential measurement unit," Master's project report, Utah State University, Logan, 2004.

[13] D. L. Hysell, M. F. Larsen, C. M. Swenson, A. Barjatya, T. F. Wheeler, M. F. Sarango, R. F. Woodman, J. L. Chau, and D. Sponseller, "Rocket and radar investigation of background electrodynamics," *Submitted to Annales Geophysicae*, 2005.

[14] R. T. Tsunoda and B. R. White, "On the generation and growth of equatorial backscatter plumes and wave structure in the bottomside f layer." *Radio Science*, vol. 14, p. 1111, 1979.

[15] S. Close, M. M. Oppenheim, S. Hunt, and L. P. Dyrud, "Scattering characteristics of high-resolution meteor head echoes detected at multiple frequencies." *Journal of Geophysics Res.*, vol. 107, p. 1295, 2002.

[16] M. A. Lieberman and A. J. Lichtenberg, *Principles of Plasma Discharges and Materials Processing*, 1st ed. John Wiley and Sons, 1994.

[17] J. Ward, C. Swenson, and C. Furse, "The impedance of a short dipole antenna in a magnetized plasma via a finite difference time domain model," *IEEE Transactions on Antennas and Propagation*, vol. 53, no. 8, pp. 2711–2718, Aug. 2005.

[18] C. Paul, *Introduction to Electromagnetic Compatability*, 1st ed., K. Chang, Ed. John Wiley and Sons, 1992.

[19] K. G. Balmain, "The properties of antennas in plasmas," *Annales Des Telecommunictaions*, vol. 35, no. 3-4, pp. 273–283, Mar.-Apr. 1979.

[20] NASA and et al, "Igrf magnetic field model," *http://nssdc.gsfc.nasa.gov/space/model/models/igrf.html*, Dec. 2004.

[21] NASA and NRL, "Msis 2000," *http://nssdc.gsfc.nasa.gov/space/model/models/msis.html*, Jun 2005.

[22] J. D. Ward, "A model of plasma probes utilizing plasma fluid equations and finite difference time domain (fdtd) theory," Master's thesis, Utah State University, Logan, 2002.

[23] C. Fish, "Design, development, test, and calibration of the floating potential measurement unit sensor suite," Master's project report, Utah State University, Logan, 2005.

[24] A. Barjatya, "Personal communication," 2005.

[25] L. R. Storey, "What's wrong with space plasma metrology?" in *Measurements Techniques in Space Plasmas, Particles*, R. F. Pfaff, Ed. American Geophysical Union, 1998.

Appendices

Appendix A

List of Measured Network Analyzer Calibrator Values

Table A.1: Measured Impedance of Calibrator Loads

	0.3[MHz]	0.5[MHz]	0.8[MHz]	1.0[MHz]	3.0[MHz]
Load 1	39.91+ 0.018i	39.9+0.029i	39.91+0.053i	39.91+0.054i	39.89+0.208i
Load 2	81.63-0.042i	81.58-0.001i	81.6+0.009i	81.57+0.018i	81.56+0.04i
Load 3	118.9-0.148i	118.8-0.035i	118.8-0.033i	118.8+0.027i	118.8-0.028i
Load 4	199.1-0.61i	198.9-0.353i	198.9-0.377i	198.7-0.123i	198.7-0.571i
Load 5	331.1-1.699i	330.5-0.983i	330.5-1.127i	330-0.285i	330.2-1.519i
Load 6	473-3.932i	472.1-2.493i	472.0-2.678i	470.9-0.778i	471.2-3.966i
Load 7	1025-18.68i	1021-11.51i	1020-12.88i	1015-3.412i	1017-18.54i
Load 8	3252-213.9i	3221-132i	3210-154.4i	3165-47.73i	3164-219.5i
Load 9	13259-3573i	13004-2128i	12741-2475i	12336-722i	11729-3322i
Load 10	-18898-38349i	-26638-57277i	-21155-56873i	-40016-193286i	-5668-45721i
Load 11	-11544-15484i	-9339-15849i	-5020-12833i	-4021-13022i	-490.5-4555i
Load 12	-5081-11441i	-2599-9301i	-1116-6323i	-695-5545i	-77.91-1849i
Load 13	-1285-6142i	-505.6-4152i	-196.4-2672i	-113.7-2214i	-12.22-736i
Load 14	-721-4680i	-265.4-3040i	-102-1936i	-56.9-1585i	-6.009-527i
Load 15	-178.9-2334i	-62.93-1464i	-23.47-925i	-13.27-749i	-1.207-249.8i
Load 16	-33.25-995i	-10.66-607i	-3.728-381.4i	-2.1-306.5i	-0.015-102.2i
Load 17	10.99-573i	13.31-351.1i	11.77-222.9i	10.78-180.1i	6.22-62.77i
Load 18	-0.006+0.216i	0.014+0.31i	0.025+0.47i	0.034+0.587i	0.029+1.734i
Load 19	0.631+3.201i	0.662+5.277i	0.697+8.421i	0.727+10.52i	0.874+31.47i
Load 20	1.297+22.63i	1.433+37.52i	1.562+59.85i	1.725+74.66i	2.1+224.4i
Load 21	5.872+66.57i	5.887+110.4i	5.733+176.5i	5.828+220.4i	-3.099+693i
Load 22	11.24+156.4i	10.46+259.1i	8.223+414.8i	7.436+516i	-50.75+1621i
Load 23	-1.015+405.9i	-7.765+674i	-24.88+1088i	-31.08+1346i	-417.2+4429i

	5.0[MHz]	8.0[MHz]	10.0[MHz]	15.0[MHz]	20.0[MHz]
Load 1	39.88+0.367i	39.89+0.6i	39.89+0.763i	39.9+1.157i	39.91+1.549i
Load 2	81.58+0.089i	81.57+0.149i	81.56+0.169i	81.64+0.204i	81.72+0.308i
Load 3	118.8-0.017i	118.8-0.009i	118.8-0.072i	118.9-0.225i	119.1-0.251i
Load 4	198.9-0.773i	198.8-1.041i	198.8-1.437i	198.9-2.442i	199.3-3.117i
Load 5	330.6-2.175i	330.6-2.844i	330.8-4.087i	330.9-6.666i	331.6-9.418i
Load 6	472.2-5.757i	471.5-7.734i	472-10.74i	471.5-16.61i	472.1-23.22i
Load 7	1021-27.91i	1019-37.55i	1022-52.1i	1016-82.55i	1019-117.1i
Load 8	3189-345.6i	3129-462i	3113-622i	2918-889i	2723-1193i
Load 9	11134-5071i	9549-5707i	7947-6721i	5089-6186i	3126-5743i
Load 10	-6771-29698i	-2706-22682i	-2637-16537i	-456.445-10799i	-600-7717i
Load 11	-215.6-2774i	-78-1763i	-56.45-1399i	-18.31-930i	-10.2-694i
Load 12	-31.33-1116i	-9.822-702i	-6.234-559i	-0.462-373.6i	0.824-288.1i
Load 13	-4.232-442.8i	-.7221-277.5i	-0.119-221.6i	0.687-147.9i	0.963-111.0i
Load 14	-1.949-316.7i	-0.229-198.3i	0.132-158.4i	0.553-105.7i	0.717-79.33i
Load 15	-0.277-150.1i	0.143-93.9i	0.257-75.06i	0.315-50.16i	0.387-37.74i
Load 16	0.137-61.33i	0.205-38.37i	0.247-30.67i	0.23-20.49i	0.265-15.43i
Load 17	4.76-38.69i	3.756-24.88i	3.393-20.16i	2.776-13.78i	2.474-10.53i
Load 18	0.033+2.87i	0.06+4.559i	0.088+5.684i	0.057+8.524i	0.048+11.33i
Load 19	1.093+52.55i	1.704+84.51i	2.240+106.2i	4.474+162.7i	7.374+223.7i
Load 20	1.653+379.6i	3.423+629i	3.362+816i	29.48+1411i	65.22+2390i
Load 21	-36.05+1285i	-163.8+2773i	-678+5257i	-1290-9450i	-145.7-3122i
Load 22	-247.5+2959i	-997+5926i	-3482+9893i	-14340-19209i	-1516-7374i
Load 23	-2102+8589i	-12170+18001i	-33307-47.93i	-4575-13031i	-1447-7485i

Appendix B

Calibration Coefficient Values for SIP Unit1

Table B.1: Calibration Coefficient Values from SIP Unit1

Frequency [MHz]	α	Z_f	b	m	K
0.1	0.10675	490.29+0.80105i	10367	9729.2	9.7391
0.1	0.10675	490.29+0.80105i	10367	9729.2	9.7391
0.15	0.10653	489.04+1.1962i	10368	9724.7	9.7397
0.2	0.10631	487.8+1.5875i	10369	9720.3	9.7403
0.25	0.10609	486.57+1.975i	10370	9715.8	9.7409
0.3	0.10587	485.35+2.3584i	10370	9711.4	9.7415
0.35	0.10565	484.15+2.7378i	10371	9707.1	9.7421
0.4	0.10544	482.96+3.1129i	10372	9702.7	9.7427
0.45	0.10522	481.79+3.4838i	10372	9698.4	9.7433
0.5	0.105	480.62+3.8503i	10373	9694.1	9.744
0.55	0.10479	479.47+4.2123i	10373	9689.8	9.7446
0.6	0.10458	478.33+4.5698i	10374	9685.5	9.7452
0.65	0.10436	477.21+4.9227i	10374	9681.3	9.7458
0.7	0.10415	476.09+5.2709i	10374	9677.1	9.7464
0.75	0.10394	474.99+5.6144i	10375	9672.9	9.747
0.8	0.10373	473.9+5.9532i	10375	9668.8	9.7477
0.85	0.10352	472.83+6.2871i	10375	9664.6	9.7483
0.9	0.10331	471.76+6.6162i	10375	9660.5	9.7489
0.95	0.10311	470.71+6.9404i	10376	9656.4	9.7496

1	0.1029	469.67+7.2597i	10376	9652.3	9.7502
1.04	0.10273	468.84+7.5116i	10376	9649.1	9.7507
1.08	0.10257	468.03+7.7604i	10376	9645.9	9.7512
1.12	0.10241	467.22+8.0059i	10376	9642.6	9.7517
1.16	0.10224	466.42+8.2482i	10376	9639.4	9.7522
1.2	0.10208	465.62+8.4874i	10376	9636.2	9.7527
1.24	0.10192	464.83+8.7233i	10376	9633	9.7532
1.28	0.10176	464.05+8.956i	10376	9629.8	9.7538
1.32	0.1016	463.28+9.1855i	10376	9626.7	9.7543
1.36	0.10144	462.51+9.4118i	10376	9623.5	9.7548
1.4	0.10128	461.76+9.6349i	10376	9620.4	9.7553
1.44	0.10112	461+9.8547i	10376	9617.2	9.7558
1.48	0.10096	460.26+10.071i	10376	9614.1	9.7564
1.52	0.1008	459.52+10.285i	10376	9611	9.7569
1.56	0.10065	458.79+10.495i	10376	9607.8	9.7574
1.6	0.10049	458.07+10.702i	10376	9604.7	9.7579
1.64	0.10033	457.35+10.906i	10375	9601.6	9.7585
1.68	0.10018	456.64+11.107i	10375	9598.5	9.759
1.72	0.10002	455.94+11.304i	10375	9595.4	9.7595
1.76	0.099869	455.24+11.498i	10375	9592.4	9.7601
1.8	0.099716	454.55+11.69i	10375	9589.3	9.7606
1.84	0.099562	453.87+11.878i	10374	9586.2	9.7611
1.88	0.09941	453.19+12.063i	10374	9583.2	9.7617
1.92	0.099258	452.52+12.244i	10374	9580.1	9.7622
1.96	0.099106	451.85+12.423i	10373	9577.1	9.7627
2	0.098955	451.2+12.599i	10373	9574	9.7633
2.04	0.098805	450.55+12.771i	10373	9571	9.7638

2.08	0.098655	449.9+12.941i	10372	9567.9	9.7644
2.12	0.098506	449.26+13.107i	10372	9564.9	9.7649
2.16	0.098357	448.63+13.271i	10372	9561.9	9.7655
2.2	0.098209	448.01+13.431i	10371	9558.9	9.766
2.24	0.098062	447.39+13.588i	10371	9555.8	9.7666
2.28	0.097915	446.77+13.743i	10370	9552.8	9.7672
2.32	0.097768	446.16+13.894i	10370	9549.8	9.7677
2.36	0.097622	445.56+14.043i	10369	9546.8	9.7683
2.4	0.097477	444.97+14.189i	10369	9543.8	9.7688
2.44	0.097333	444.38+14.332i	10368	9540.8	9.7694
2.48	0.097188	443.8+14.472i	10368	9537.8	9.77
2.52	0.097045	443.22+14.609i	10367	9534.8	9.7705
2.56	0.096902	442.65+14.743i	10367	9531.8	9.7711
2.6	0.09676	442.08+14.875i	10366	9528.8	9.7717
2.64	0.096618	441.52+15.004i	10366	9525.8	9.7723
2.68	0.096476	440.97+15.13i	10365	9522.8	9.7728
2.72	0.096336	440.42+15.253i	10364	9519.8	9.7734
2.76	0.096196	439.88+15.374i	10364	9516.8	9.774
2.8	0.096056	439.34+15.492i	10363	9513.9	9.7746
2.84	0.095917	438.81+15.608i	10363	9510.9	9.7752
2.88	0.095779	438.28+15.72i	10362	9507.9	9.7758
2.92	0.095641	437.76+15.831i	10361	9504.9	9.7764
2.96	0.095503	437.24+15.939i	10361	9501.9	9.777
3	0.095367	436.73+16.044i	10360	9498.9	9.7775
3.04	0.095231	436.23+16.147i	10359	9495.9	9.7781
3.08	0.095095	435.73+16.247i	10358	9492.9	9.7787
3.12	0.09496	435.24+16.345i	10358	9489.9	9.7793

3.16	0.094826	434.75+16.44i	10357	9486.9	9.78
3.2	0.094692	434.26+16.533i	10356	9483.9	9.7806
3.24	0.094558	433.78+16.624i	10355	9480.9	9.7812
3.28	0.094426	433.31+16.713i	10354	9477.9	9.7818
3.32	0.094293	432.84+16.799i	10354	9474.9	9.7824
3.36	0.094162	432.38+16.883i	10353	9471.9	9.783
3.4	0.094031	431.92+16.965i	10352	9468.9	9.7836
3.44	0.0939	431.47+17.044i	10351	9465.8	9.7843
3.48	0.09377	431.02+17.122i	10350	9462.8	9.7849
3.52	0.093641	430.57+17.197i	10349	9459.8	9.7855
3.56	0.093512	430.13+17.271i	10349	9456.8	9.7861
3.6	0.093384	429.7+17.342i	10348	9453.7	9.7868
3.64	0.093256	429.27+17.411i	10347	9450.7	9.7874
3.68	0.093129	428.85+17.478i	10346	9447.7	9.788
3.72	0.093003	428.42+17.543i	10345	9444.6	9.7887
3.76	0.092877	428.01+17.607i	10344	9441.6	9.7893
3.8	0.092752	427.6+17.668i	10343	9438.5	9.79
3.84	0.092627	427.19+17.728i	10342	9435.4	9.7906
3.88	0.092503	426.79+17.786i	10341	9432.4	9.7913
3.92	0.092379	426.39+17.842i	10340	9429.3	9.7919
3.96	0.092256	426+17.896i	10339	9426.2	9.7926
4	0.092133	425.61+17.949i	10338	9423.1	9.7932
4.04	0.092011	425.22+17.999i	10337	9420.1	9.7939
4.08	0.09189	424.84+18.049i	10336	9417	9.7946
4.12	0.091769	424.47+18.096i	10335	9413.9	9.7952
4.16	0.091649	424.09+18.142i	10334	9410.7	9.7959
4.2	0.091529	423.73+18.187i	10333	9407.6	9.7966

4.24	0.09141	423.36+18.23i	10332	9404.5	9.7972
4.28	0.091292	423+18.271i	10330	9401.4	9.7979
4.32	0.091174	422.65+18.312i	10329	9398.2	9.7986
4.36	0.091056	422.29+18.35i	10328	9395.1	9.7993
4.4	0.09094	421.95+18.388i	10327	9391.9	9.8
4.44	0.090823	421.6+18.423i	10326	9388.8	9.8007
4.48	0.090708	421.26+18.458i	10325	9385.6	9.8014
4.52	0.090592	420.93+18.492i	10324	9382.4	9.802
4.56	0.090478	420.59+18.524i	10323	9379.2	9.8027
4.6	0.090364	420.26+18.555i	10321	9376	9.8034
4.64	0.090251	419.94+18.585i	10320	9372.8	9.8041
4.68	0.090138	419.62+18.613i	10319	9369.6	9.8048
4.72	0.090025	419.3+18.641i	10318	9366.4	9.8056
4.76	0.089914	418.99+18.668i	10317	9363.2	9.8063
4.8	0.089803	418.67+18.693i	10315	9359.9	9.807
4.84	0.089692	418.37+18.718i	10314	9356.7	9.8077
4.88	0.089582	418.06+18.742i	10313	9353.4	9.8084
4.92	0.089473	417.76+18.764i	10312	9350.1	9.8091
4.96	0.089364	417.47+18.786i	10310	9346.9	9.8099
5	0.089255	417.17+18.807i	10309	9343.6	9.8106
5.04	0.089148	416.88+18.828i	10308	9340.3	9.8113
5.08	0.08904	416.6+18.847i	10306	9337	9.8121
5.12	0.088934	416.31+18.866i	10305	9333.6	9.8128
5.16	0.088828	416.03+18.884i	10304	9330.3	9.8135
5.2	0.088722	415.76+18.902i	10302	9327	9.8143
5.24	0.088617	415.48+18.918i	10301	9323.6	9.815
5.28	0.088513	415.21+18.935i	10300	9320.2	9.8158

5.32	0.088409	414.94+18.95i	10298	9316.9	9.8165
5.36	0.088306	414.68+18.966i	10297	9313.5	9.8173
5.4	0.088204	414.42+18.98i	10296	9310.1	9.818
5.44	0.088102	414.16+18.995i	10294	9306.7	9.8188
5.48	0.088	413.9+19.009i	10293	9303.2	9.8195
5.52	0.087899	413.65+19.022i	10292	9299.8	9.8203
5.56	0.087799	413.4+19.035i	10290	9296.3	9.8211
5.6	0.087699	413.15+19.048i	10289	9292.9	9.8218
5.64	0.0876	412.91+19.061i	10287	9289.4	9.8226
5.68	0.087501	412.67+19.074i	10286	9285.9	9.8234
5.72	0.087403	412.43+19.086i	10284	9282.4	9.8242
5.76	0.087306	412.19+19.098i	10283	9278.9	9.825
5.8	0.087209	411.96+19.11i	10282	9275.4	9.8257
5.84	0.087112	411.73+19.122i	10280	9271.9	9.8265
5.88	0.087017	411.5+19.134i	10279	9268.3	9.8273
5.92	0.086921	411.27+19.146i	10277	9264.7	9.8281
5.96	0.086827	411.05+19.158i	10276	9261.2	9.8289
6	0.086733	410.83+19.17i	10274	9257.6	9.8297
6.04	0.086639	410.61+19.182i	10273	9254	9.8305
6.08	0.086546	410.4+19.194i	10271	9250.4	9.8313
6.12	0.086454	410.18+19.206i	10270	9246.7	9.8321
6.16	0.086362	409.97+19.219i	10268	9243.1	9.8329
6.2	0.086271	409.77+19.232i	10267	9239.4	9.8338
6.24	0.08618	409.56+19.245i	10265	9235.8	9.8346
6.28	0.08609	409.36+19.258i	10263	9232.1	9.8354
6.32	0.086	409.15+19.272i	10262	9228.4	9.8362
6.36	0.085911	408.96+19.286i	10260	9224.7	9.837

6.4	0.085823	408.76+19.3i	10259	9220.9	9.8379
6.44	0.085735	408.56+19.315i	10257	9217.2	9.8387
6.48	0.085648	408.37+19.331i	10256	9213.4	9.8395
6.52	0.085561	408.18+19.347i	10254	9209.7	9.8404
6.56	0.085475	407.99+19.363i	10252	9205.9	9.8412
6.6	0.085389	407.81+19.38i	10251	9202.1	9.8421
6.64	0.085304	407.62+19.398i	10249	9198.3	9.8429
6.68	0.08522	407.44+19.416i	10248	9194.4	9.8438
6.72	0.085136	407.26+19.435i	10246	9190.6	9.8446
6.76	0.085053	407.08+19.455i	10244	9186.7	9.8455
6.8	0.08497	406.9+19.476i	10243	9182.9	9.8463
6.84	0.084888	406.73+19.497i	10241	9179	9.8472
6.88	0.084806	406.56+19.519i	10239	9175.1	9.848
6.92	0.084725	406.39+19.542i	10238	9171.1	9.8489
6.96	0.084645	406.22+19.566i	10236	9167.2	9.8498
7	0.084565	406.05+19.59i	10234	9163.2	9.8507
7.04	0.084486	405.88+19.616i	10233	9159.3	9.8515
7.08	0.084407	405.72+19.642i	10231	9155.3	9.8524
7.12	0.084329	405.56+19.67i	10229	9151.3	9.8533
7.16	0.084251	405.4+19.698i	10227	9147.3	9.8542
7.2	0.084174	405.24+19.728i	10226	9143.2	9.8551
7.24	0.084098	405.08+19.759i	10224	9139.2	9.856
7.28	0.084022	404.93+19.791i	10222	9135.1	9.8568
7.32	0.083947	404.77+19.824i	10220	9131	9.8577
7.36	0.083872	404.62+19.858i	10219	9127	9.8586
7.4	0.083798	404.47+19.893i	10217	9122.8	9.8595
7.44	0.083724	404.32+19.93i	10215	9118.7	9.8604

7.48	0.083651	404.18+19.967i	10213	9114.6	9.8614
7.52	0.083578	404.03+20.006i	10212	9110.4	9.8623
7.56	0.083507	403.88+20.047i	10210	9106.2	9.8632
7.6	0.083435	403.74+20.089i	10208	9102	9.8641
7.64	0.083364	403.6+20.132i	10206	9097.8	9.865
7.68	0.083294	403.46+20.176i	10204	9093.6	9.8659
7.72	0.083225	403.32+20.222i	10202	9089.4	9.8669
7.76	0.083155	403.18+20.27i	10201	9085.1	9.8678
7.8	0.083087	403.05+20.318i	10199	9080.8	9.8687
7.84	0.083019	402.91+20.369i	10197	9076.5	9.8696
7.88	0.082952	402.78+20.421i	10195	9072.2	9.8706
7.92	0.082885	402.64+20.474i	10193	9067.9	9.8715
7.96	0.082819	402.51+20.529i	10191	9063.6	9.8725
8	0.082753	402.38+20.586i	10189	9059.2	9.8734
8.04	0.082688	402.25+20.644i	10188	9054.8	9.8743
8.08	0.082623	402.12+20.704i	10186	9050.4	9.8753
8.12	0.082559	402+20.765i	10184	9046	9.8762
8.16	0.082496	401.87+20.828i	10182	9041.6	9.8772
8.2	0.082433	401.75+20.893i	10180	9037.2	9.8782
8.24	0.082371	401.62+20.96i	10178	9032.7	9.8791
8.28	0.082309	401.5+21.028i	10176	9028.2	9.8801
8.32	0.082248	401.38+21.098i	10174	9023.7	9.881
8.36	0.082187	401.26+21.17i	10172	9019.2	9.882
8.4	0.082127	401.14+21.244i	10170	9014.7	9.883
8.44	0.082068	401.02+21.319i	10168	9010.1	9.8839
8.48	0.082009	400.91+21.397i	10166	9005.6	9.8849
8.52	0.081951	400.79+21.476i	10164	9001	9.8859

8.56	0.081893	400.67+21.557i	10162	8996.4	9.8869
8.6	0.081836	400.56+21.64i	10160	8991.8	9.8879
8.64	0.08178	400.44+21.725i	10158	8987.2	9.8888
8.68	0.081724	400.33+21.812i	10156	8982.5	9.8898
8.72	0.081668	400.22+21.901i	10154	8977.9	9.8908
8.76	0.081613	400.11+21.991i	10152	8973.2	9.8918
8.8	0.081559	400+22.084i	10150	8968.5	9.8928
8.84	0.081505	399.89+22.179i	10148	8963.8	9.8938
8.88	0.081452	399.78+22.275i	10146	8959	9.8948
8.92	0.081399	399.67+22.374i	10144	8954.3	9.8958
8.96	0.081347	399.56+22.475i	10142	8949.5	9.8968
9	0.081296	399.46+22.577i	10140	8944.7	9.8978
9.04	0.081245	399.35+22.682i	10138	8939.9	9.8988
9.08	0.081195	399.25+22.789i	10136	8935.1	9.8998
9.12	0.081145	399.14+22.898i	10134	8930.3	9.9008
9.16	0.081096	399.04+23.009i	10131	8925.5	9.9019
9.2	0.081047	398.94+23.122i	10129	8920.6	9.9029
9.24	0.080999	398.83+23.237i	10127	8915.7	9.9039
9.28	0.080952	398.73+23.355i	10125	8910.8	9.9049
9.32	0.080905	398.63+23.474i	10123	8905.9	9.9059
9.36	0.080858	398.53+23.595i	10121	8901	9.907
9.4	0.080813	398.43+23.719i	10119	8896	9.908
9.44	0.080767	398.33+23.845i	10116	8891	9.909
9.48	0.080723	398.23+23.972i	10114	8886.1	9.9101
9.52	0.080679	398.13+24.102i	10112	8881.1	9.9111
9.56	0.080635	398.03+24.234i	10110	8876.1	9.9121
9.6	0.080592	397.94+24.369i	10108	8871	9.9132

9.64	0.08055	397.84+24.505i	10105	8866	9.9142
9.68	0.080508	397.74+24.643i	10103	8860.9	9.9153
9.72	0.080467	397.65+24.784i	10101	8855.8	9.9163
9.76	0.080426	397.55+24.927i	10099	8850.7	9.9174
9.8	0.080386	397.46+25.071i	10096	8845.6	9.9184
9.84	0.080347	397.36+25.218i	10094	8840.5	9.9195
9.88	0.080308	397.27+25.367i	10092	8835.3	9.9205
9.92	0.080269	397.17+25.519i	10090	8830.2	9.9216
9.96	0.080232	397.08+25.672i	10087	8825	9.9226
10	0.080194	396.99+25.827i	10085	8819.8	9.9237
10.04	0.080158	396.89+25.985i	10083	8814.6	9.9248
10.54	0.079747	395.76+28.127i	10053	8748.1	9.9382
11.04	0.079425	394.67+30.569i	10022	8679.3	9.9519
11.54	0.079193	393.62+33.265i	9988.2	8608.3	9.9658
12.04	0.079049	392.6+36.146i	9952.9	8535.3	9.9799
12.54	0.078993	391.64+39.119i	9915.3	8460.6	9.994
13.04	0.079027	390.77+42.064i	9875.2	8384.4	10.008
13.54	0.079149	390.04+44.834i	9832.3	8307	10.022
14.04	0.079361	389.52+47.254i	9786.4	8228.9	10.036
14.54	0.079661	389.33+49.113i	9737.1	8150.4	10.05
15.04	0.08005	389.57+50.163i	9684.1	8072	10.064
17.54	0.083326	401.34+30.079i	9349.3	7699.2	10.124

Appendix C

Calibration Coefficient Values for SIP Unit2

Table C.1: Calibration Coefficient Values from SIP Unit2

Frequency [MHz]	α	Z_f	b	m	K
0.1	0.10304	468.12+0.67233i	10503	9756.9	9.7436
0.1	0.10304	468.12+0.67233i	10503	9756.9	9.7436
0.15	0.1028	468.87+1.0209i	10504	9755	9.7441
0.2	0.10255	469.56+1.3767i	10505	9753.1	9.7446
0.25	0.10231	470.22+1.7389i	10506	9751	9.7451
0.3	0.10207	470.83+2.1068i	10507	9748.9	9.7456
0.35	0.10182	471.4+2.4796i	10508	9746.8	9.7461
0.4	0.10159	471.92+2.8567i	10509	9744.5	9.7466
0.45	0.10135	472.41+3.2372i	10510	9742.2	9.7471
0.5	0.10111	472.85+3.6205i	10511	9739.8	9.7477
0.55	0.10087	473.26+4.0059i	10512	9737.4	9.7482
0.6	0.10064	473.63+4.3928i	10512	9734.9	9.7487
0.65	0.10041	473.96+4.7806i	10513	9732.3	9.7492
0.7	0.10017	474.25+5.1685i	10514	9729.7	9.7498
0.75	0.099943	474.51+5.5561i	10514	9727	9.7503
0.8	0.099714	474.73+5.9427i	10515	9724.3	9.7509
0.85	0.099485	474.92+6.3278i	10516	9721.4	9.7514
0.9	0.099259	475.08+6.7109i	10516	9718.6	9.752
0.95	0.099033	475.2+7.0914i	10517	9715.7	9.7525

1	0.098809	475.29+7.469i	10517	9712.7	9.7531
1.05	0.098586	475.35+7.843i	10517	9709.7	9.7536
1.09	0.098408	475.38+8.1395i	10518	9707.3	9.7541
1.13	0.098232	475.38+8.4332i	10518	9704.8	9.7545
1.17	0.098056	475.37+8.7241i	10518	9702.3	9.755
1.21	0.097881	475.34+9.0118i	10518	9699.7	9.7555
1.25	0.097707	475.29+9.2962i	10519	9697.2	9.7559
1.29	0.097533	475.22+9.5771i	10519	9694.6	9.7564
1.33	0.097361	475.14+9.8544i	10519	9692	9.7569
1.37	0.097189	475.04+10.128i	10519	9689.3	9.7573
1.41	0.097018	474.92+10.398i	10519	9686.6	9.7578
1.45	0.096848	474.79+10.663i	10519	9683.9	9.7583
1.49	0.096679	474.64+10.924i	10519	9681.2	9.7588
1.53	0.096511	474.48+11.181i	10519	9678.5	9.7593
1.57	0.096343	474.3+11.434i	10519	9675.7	9.7598
1.61	0.096177	474.11+11.682i	10519	9672.9	9.7602
1.65	0.096011	473.9+11.925i	10519	9670.1	9.7607
1.69	0.095846	473.68+12.163i	10519	9667.3	9.7612
1.73	0.095681	473.44+12.397i	10519	9664.4	9.7617
1.77	0.095518	473.19+12.626i	10519	9661.5	9.7622
1.81	0.095355	472.93+12.85i	10519	9658.6	9.7627
1.85	0.095194	472.65+13.069i	10519	9655.7	9.7633
1.89	0.095033	472.37+13.282i	10518	9652.8	9.7638
1.93	0.094873	472.07+13.491i	10518	9649.8	9.7643
1.97	0.094713	471.75+13.695i	10518	9646.8	9.7648
2.01	0.094555	471.43+13.893i	10518	9643.8	9.7653
2.05	0.094397	471.1+14.086i	10518	9640.8	9.7658

2.09	0.09424	470.75+14.274i	10517	9637.8	9.7664
2.13	0.094084	470.4+14.456i	10517	9634.8	9.7669
2.17	0.093929	470.03+14.634i	10517	9631.7	9.7674
2.21	0.093775	469.66+14.806i	10516	9628.6	9.768
2.25	0.093622	469.27+14.973i	10516	9625.5	9.7685
2.29	0.093469	468.88+15.135i	10516	9622.4	9.769
2.33	0.093317	468.47+15.291i	10515	9619.3	9.7696
2.37	0.093166	468.06+15.443i	10515	9616.2	9.7701
2.41	0.093016	467.64+15.589i	10515	9613	9.7707
2.45	0.092866	467.21+15.73i	10514	9609.9	9.7712
2.49	0.092718	466.77+15.866i	10514	9606.7	9.7718
2.53	0.09257	466.32+15.997i	10513	9603.5	9.7724
2.57	0.092423	465.87+16.123i	10513	9600.3	9.7729
2.61	0.092277	465.41+16.244i	10512	9597.1	9.7735
2.65	0.092132	464.94+16.36i	10512	9593.9	9.774
2.69	0.091988	464.47+16.471i	10511	9590.7	9.7746
2.73	0.091844	463.99+16.578i	10511	9587.4	9.7752
2.77	0.091701	463.5+16.68i	10510	9584.2	9.7758
2.81	0.091559	463.01+16.777i	10510	9580.9	9.7764
2.85	0.091418	462.51+16.869i	10509	9577.7	9.7769
2.89	0.091278	462+16.957i	10509	9574.4	9.7775
2.93	0.091139	461.49+17.041i	10508	9571.1	9.7781
2.97	0.091	460.97+17.12i	10507	9567.8	9.7787
3.01	0.090862	460.45+17.195i	10507	9564.5	9.7793
3.05	0.090725	459.93+17.266i	10506	9561.2	9.7799
3.09	0.090589	459.4+17.333i	10505	9557.8	9.7805
3.13	0.090454	458.86+17.396i	10505	9554.5	9.7811

3.17	0.090319	458.33+17.455i	10504	9551.2	9.7817
3.21	0.090186	457.78+17.51i	10503	9547.8	9.7823
3.25	0.090053	457.24+17.561i	10503	9544.5	9.783
3.29	0.089921	456.69+17.609i	10502	9541.1	9.7836
3.33	0.08979	456.13+17.653i	10501	9537.8	9.7842
3.37	0.089659	455.58+17.693i	10500	9534.4	9.7848
3.41	0.08953	455.02+17.73i	10500	9531	9.7855
3.45	0.089401	454.46+17.764i	10499	9527.6	9.7861
3.49	0.089273	453.89+17.795i	10498	9524.2	9.7867
3.53	0.089146	453.32+17.823i	10497	9520.8	9.7874
3.57	0.08902	452.75+17.848i	10497	9517.4	9.788
3.61	0.088894	452.18+17.87i	10496	9514	9.7887
3.65	0.08877	451.61+17.889i	10495	9510.6	9.7893
3.69	0.088646	451.03+17.905i	10494	9507.2	9.79
3.73	0.088523	450.45+17.919i	10493	9503.8	9.7906
3.77	0.088401	449.88+17.931i	10492	9500.4	9.7913
3.81	0.08828	449.3+17.94i	10491	9496.9	9.7919
3.85	0.088159	448.71+17.947i	10490	9493.5	9.7926
3.89	0.08804	448.13+17.952i	10490	9490.1	9.7933
3.93	0.087921	447.55+17.954i	10489	9486.6	9.7939
3.97	0.087803	446.97+17.955i	10488	9483.2	9.7946
4.01	0.087686	446.38+17.954i	10487	9479.7	9.7953
4.05	0.08757	445.8+17.951i	10486	9476.3	9.796
4.09	0.087454	445.21+17.947i	10485	9472.8	9.7967
4.13	0.087339	444.63+17.941i	10484	9469.3	9.7973
4.17	0.087226	444.04+17.933i	10483	9465.9	9.798
4.21	0.087113	443.45+17.924i	10482	9462.4	9.7987

4.25	0.087	442.87+17.914i	10481	9458.9	9.7994
4.29	0.086889	442.28+17.903i	10480	9455.4	9.8001
4.33	0.086779	441.7+17.891i	10479	9452	9.8008
4.37	0.086669	441.12+17.878i	10478	9448.5	9.8015
4.41	0.08656	440.53+17.863i	10477	9445	9.8022
4.45	0.086452	439.95+17.849i	10476	9441.5	9.803
4.49	0.086345	439.37+17.833i	10475	9438	9.8037
4.53	0.086238	438.79+17.817i	10474	9434.5	9.8044
4.57	0.086133	438.21+17.8i	10473	9431	9.8051
4.61	0.086028	437.63+17.783i	10471	9427.5	9.8058
4.65	0.085924	437.06+17.765i	10470	9424	9.8066
4.69	0.085821	436.48+17.748i	10469	9420.5	9.8073
4.73	0.085719	435.91+17.73i	10468	9417	9.808
4.77	0.085617	435.34+17.712i	10467	9413.4	9.8088
4.81	0.085517	434.77+17.694i	10466	9409.9	9.8095
4.85	0.085417	434.2+17.676i	10465	9406.4	9.8103
4.89	0.085318	433.63+17.658i	10464	9402.9	9.811
4.93	0.08522	433.07+17.641i	10462	9399.3	9.8118
4.97	0.085123	432.51+17.624i	10461	9395.8	9.8125
5.01	0.085026	431.95+17.607i	10460	9392.3	9.8133
5.05	0.08493	431.39+17.59i	10459	9388.7	9.814
5.09	0.084836	430.83+17.575i	10458	9385.2	9.8148
5.13	0.084742	430.28+17.56i	10456	9381.6	9.8156
5.17	0.084648	429.73+17.545i	10455	9378.1	9.8163
5.21	0.084556	429.18+17.531i	10454	9374.5	9.8171
5.25	0.084465	428.64+17.518i	10453	9370.9	9.8179
5.29	0.084374	428.1+17.506i	10451	9367.4	9.8187

5.33	0.084284	427.56+17.495i	10450	9363.8	9.8195
5.37	0.084195	427.02+17.485i	10449	9360.2	9.8202
5.41	0.084107	426.49+17.476i	10448	9356.7	9.821
5.45	0.084019	425.96+17.468i	10446	9353.1	9.8218
5.49	0.083933	425.43+17.461i	10445	9349.5	9.8226
5.53	0.083847	424.91+17.456i	10444	9345.9	9.8234
5.57	0.083762	424.39+17.452i	10442	9342.3	9.8242
5.61	0.083678	423.87+17.449i	10441	9338.7	9.825
5.65	0.083595	423.36+17.447i	10440	9335.1	9.8258
5.69	0.083512	422.85+17.447i	10439	9331.5	9.8266
5.73	0.083431	422.34+17.449i	10437	9327.9	9.8275
5.77	0.08335	421.84+17.452i	10436	9324.3	9.8283
5.81	0.08327	421.34+17.456i	10434	9320.7	9.8291
5.85	0.083191	420.84+17.463i	10433	9317	9.8299
5.89	0.083113	420.35+17.471i	10432	9313.4	9.8307
5.93	0.083035	419.86+17.48i	10430	9309.8	9.8316
5.97	0.082959	419.37+17.492i	10429	9306.1	9.8324
6.01	0.082883	418.89+17.505i	10428	9302.5	9.8332
6.05	0.082808	418.41+17.52i	10426	9298.8	9.8341
6.09	0.082734	417.94+17.537i	10425	9295.2	9.8349
6.13	0.08266	417.47+17.555i	10423	9291.5	9.8358
6.17	0.082588	417.01+17.576i	10422	9287.8	9.8366
6.21	0.082516	416.54+17.599i	10421	9284.1	9.8375
6.25	0.082445	416.09+17.623i	10419	9280.5	9.8383
6.29	0.082375	415.63+17.65i	10418	9276.8	9.8392
6.33	0.082306	415.18+17.679i	10416	9273.1	9.84
6.37	0.082238	414.74+17.71i	10415	9269.4	9.8409

6.41	0.08217	414.3+17.742i	10413	9265.7	9.8418
6.45	0.082103	413.86+17.777i	10412	9261.9	9.8426
6.49	0.082037	413.43+17.815i	10410	9258.2	9.8435
6.53	0.081972	413+17.854i	10409	9254.5	9.8444
6.57	0.081908	412.57+17.895i	10407	9250.7	9.8452
6.61	0.081845	412.15+17.939i	10406	9247	9.8461
6.65	0.081782	411.74+17.985i	10404	9243.2	9.847
6.69	0.08172	411.32+18.033i	10403	9239.5	9.8479
6.73	0.081659	410.92+18.083i	10401	9235.7	9.8488
6.77	0.081599	410.51+18.136i	10400	9231.9	9.8497
6.81	0.08154	410.11+18.191i	10398	9228.1	9.8506
6.85	0.081481	409.72+18.248i	10397	9224.3	9.8514
6.89	0.081424	409.33+18.307i	10395	9220.5	9.8523
6.93	0.081367	408.94+18.369i	10393	9216.7	9.8532
6.97	0.081311	408.56+18.432i	10392	9212.9	9.8541
7.01	0.081256	408.18+18.499i	10390	9209.1	9.8551
7.05	0.081201	407.81+18.567i	10389	9205.2	9.856
7.09	0.081148	407.44+18.638i	10387	9201.4	9.8569
7.13	0.081095	407.08+18.711i	10385	9197.5	9.8578
7.17	0.081043	406.72+18.786i	10384	9193.6	9.8587
7.21	0.080992	406.36+18.864i	10382	9189.8	9.8596
7.25	0.080942	406.01+18.944i	10380	9185.9	9.8605
7.29	0.080893	405.67+19.026i	10379	9182	9.8615
7.33	0.080844	405.32+19.111i	10377	9178	9.8624
7.37	0.080797	404.99+19.197i	10375	9174.1	9.8633
7.41	0.08075	404.65+19.286i	10374	9170.2	9.8643
7.45	0.080704	404.32+19.378i	10372	9166.2	9.8652

7.49	0.080658	404+19.471i	10370	9162.3	9.8661
7.53	0.080614	403.68+19.567i	10369	9158.3	9.8671
7.57	0.08057	403.36+19.665i	10367	9154.3	9.868
7.61	0.080528	403.05+19.765i	10365	9150.3	9.869
7.65	0.080486	402.74+19.867i	10364	9146.3	9.8699
7.69	0.080444	402.44+19.972i	10362	9142.3	9.8709
7.73	0.080404	402.14+20.078i	10360	9138.3	9.8718
7.77	0.080365	401.84+20.187i	10358	9134.2	9.8728
7.81	0.080326	401.55+20.298i	10357	9130.2	9.8737
7.85	0.080288	401.27+20.411i	10355	9126.1	9.8747
7.89	0.080251	400.98+20.526i	10353	9122	9.8756
7.93	0.080215	400.71+20.643i	10351	9117.9	9.8766
7.97	0.08018	400.43+20.762i	10349	9113.8	9.8776
8.01	0.080145	400.16+20.883i	10348	9109.7	9.8785
8.05	0.080112	399.9+21.006i	10346	9105.5	9.8795
8.09	0.080079	399.64+21.131i	10344	9101.4	9.8805
8.13	0.080047	399.38+21.258i	10342	9097.2	9.8814
8.17	0.080016	399.12+21.386i	10340	9093	9.8824
8.21	0.079985	398.88+21.517i	10339	9088.9	9.8834
8.25	0.079956	398.63+21.649i	10337	9084.6	9.8844
8.29	0.079927	398.39+21.784i	10335	9080.4	9.8854
8.33	0.079899	398.15+21.92i	10333	9076.2	9.8864
8.37	0.079872	397.92+22.057i	10331	9071.9	9.8873
8.41	0.079846	397.69+22.197i	10329	9067.6	9.8883
8.45	0.07982	397.46+22.338i	10327	9063.4	9.8893
8.49	0.079796	397.24+22.48i	10325	9059	9.8903
8.53	0.079772	397.02+22.624i	10323	9054.7	9.8913

8.57	0.079749	396.81+22.77i	10322	9050.4	9.8923
8.61	0.079727	396.6+22.917i	10320	9046	9.8933
8.65	0.079706	396.39+23.066i	10318	9041.7	9.8943
8.69	0.079685	396.19+23.216i	10316	9037.3	9.8953
8.73	0.079666	395.99+23.367i	10314	9032.9	9.8963
8.77	0.079647	395.79+23.52i	10312	9028.5	9.8973
8.81	0.079629	395.6+23.674i	10310	9024	9.8983
8.85	0.079612	395.41+23.829i	10308	9019.6	9.8993
8.89	0.079595	395.23+23.986i	10306	9015.1	9.9004
8.93	0.07958	395.05+24.143i	10304	9010.6	9.9014
8.97	0.079565	394.87+24.302i	10302	9006.1	9.9024
9.01	0.079551	394.69+24.462i	10300	9001.6	9.9034
9.05	0.079538	394.52+24.622i	10298	8997	9.9044
9.09	0.079526	394.35+24.784i	10296	8992.5	9.9054
9.13	0.079515	394.19+24.946i	10293	8987.9	9.9065
9.17	0.079504	394.03+25.11i	10291	8983.3	9.9075
9.21	0.079494	393.87+25.274i	10289	8978.7	9.9085
9.25	0.079486	393.72+25.438i	10287	8974	9.9095
9.29	0.079477	393.56+25.604i	10285	8969.4	9.9106
9.33	0.07947	393.42+25.77i	10283	8964.7	9.9116
9.37	0.079464	393.27+25.936i	10281	8960	9.9126
9.41	0.079458	393.13+26.104i	10279	8955.3	9.9137
9.45	0.079453	392.99+26.271i	10277	8950.6	9.9147
9.49	0.07945	392.86+26.439i	10274	8945.8	9.9157
9.53	0.079446	392.72+26.607i	10272	8941	9.9168
9.57	0.079444	392.59+26.776i	10270	8936.2	9.9178
9.61	0.079443	392.47+26.945i	10268	8931.4	9.9188

9.65	0.079442	392.34+27.113i	10266	8926.6	9.9199
9.69	0.079442	392.22+27.282i	10263	8921.7	9.9209
9.73	0.079443	392.1+27.451i	10261	8916.9	9.922
9.77	0.079445	391.99+27.62i	10259	8912	9.923
9.81	0.079448	391.87+27.789i	10257	8907.1	9.9241
9.85	0.079451	391.76+27.958i	10254	8902.1	9.9251
9.89	0.079456	391.66+28.126i	10252	8897.2	9.9262
9.93	0.079461	391.55+28.294i	10250	8892.2	9.9272
9.97	0.079467	391.45+28.462i	10247	8887.2	9.9283
10.01	0.079474	391.35+28.629i	10245	8882.2	9.9293
10.05	0.079481	391.25+28.796i	10243	8877.1	9.9304
10.55	0.079646	390.25+30.812i	10213	8812.4	9.9436
11.05	0.079941	389.57+32.608i	10180	8744.3	9.9569
11.55	0.080364	389.18+34.058i	10146	8672.9	9.9702
12.05	0.080917	389.03+35.047i	10109	8598.4	9.9835
12.55	0.081598	389.06+35.491i	10070	8521.1	9.9967
13.05	0.082409	389.25+35.352i	10028	8441.5	10.01
13.55	0.083349	389.58+34.657i	9982.5	8360.3	10.022
14.05	0.084418	390.01+33.52i	9934.5	8278.5	10.035
14.55	0.085616	390.53+32.163i	9883.3	8197.1	10.047
15.05	0.086943	391.17+30.946i	9828.9	8117.7	10.058
17.55	0.095516	396.46+53.114i	9505.6	7818.7	10.102

Appendix D

Calibration Load Fitting Figures

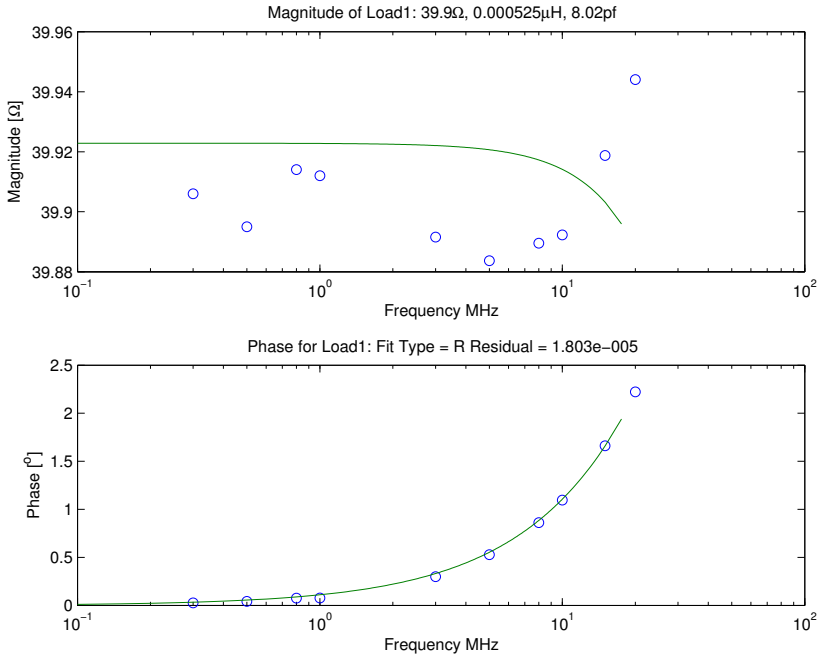

Fig. D.1: Calibration load 1, a 40.2 Ω resistor.

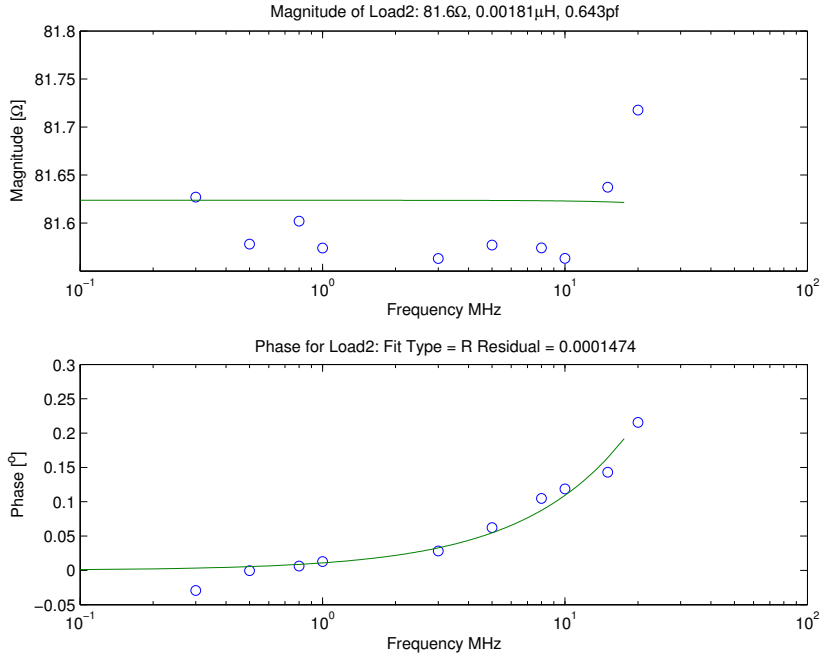

Fig. D.2: Calibration load 2, a 82 Ω resistor.

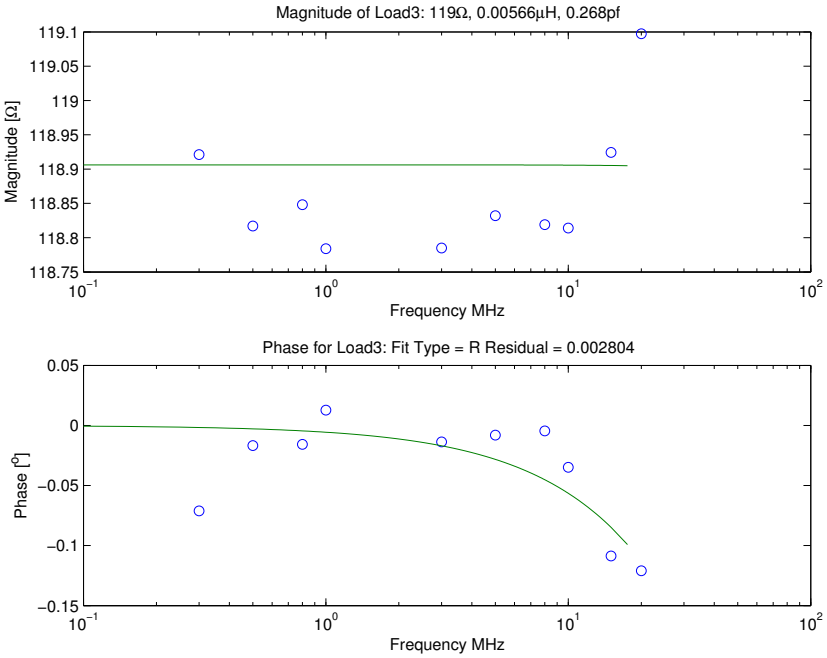

Fig. D.3: Calibration load 3, a 120 Ω resistor.

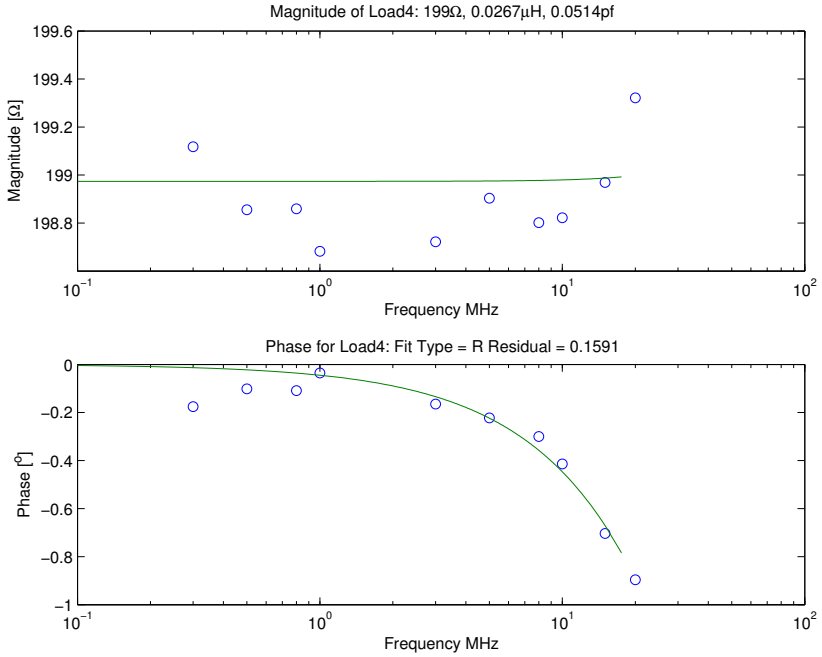

Fig. D.4: Calibration load 4, a 200 Ω resistor.

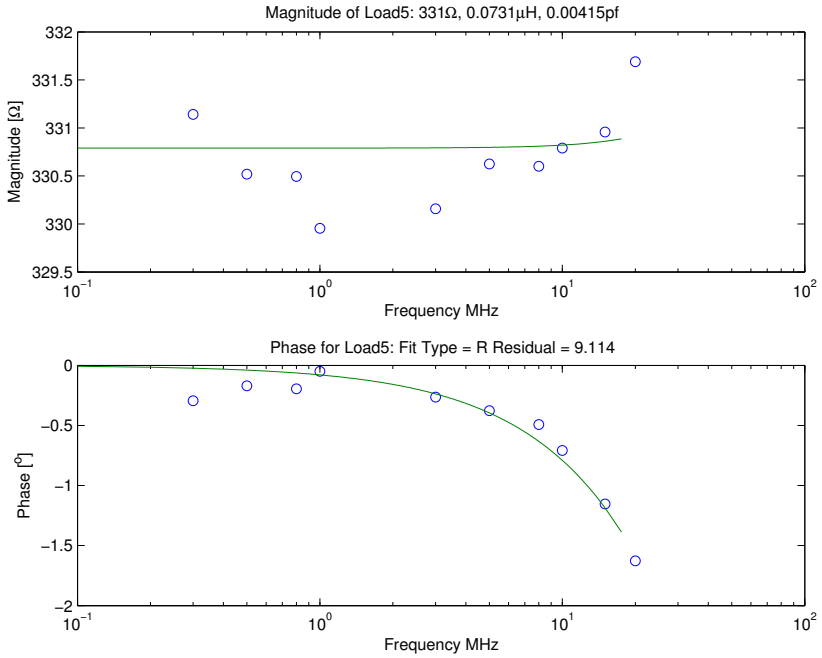

Fig. D.5: Calibration load 5, a 330 Ω resistor.

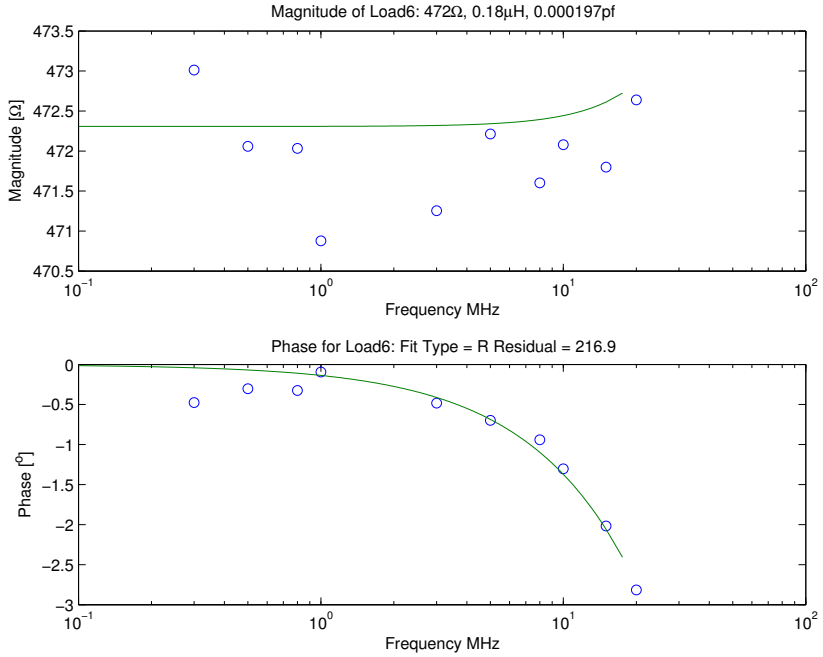

Fig. D.6: Calibration load 6, a 470 Ω resistor.

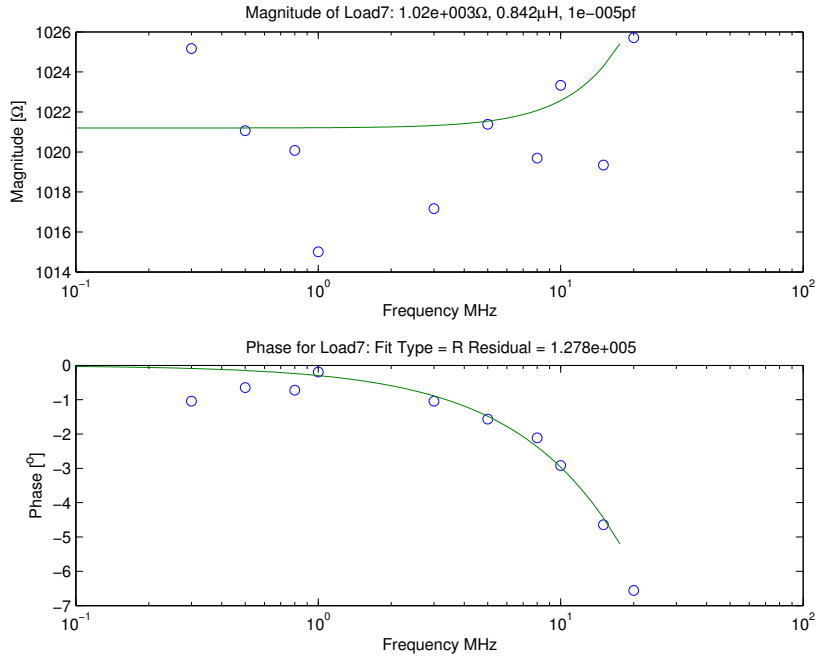

Fig. D.7: Calibration load 7, a 1 kΩ resistor.

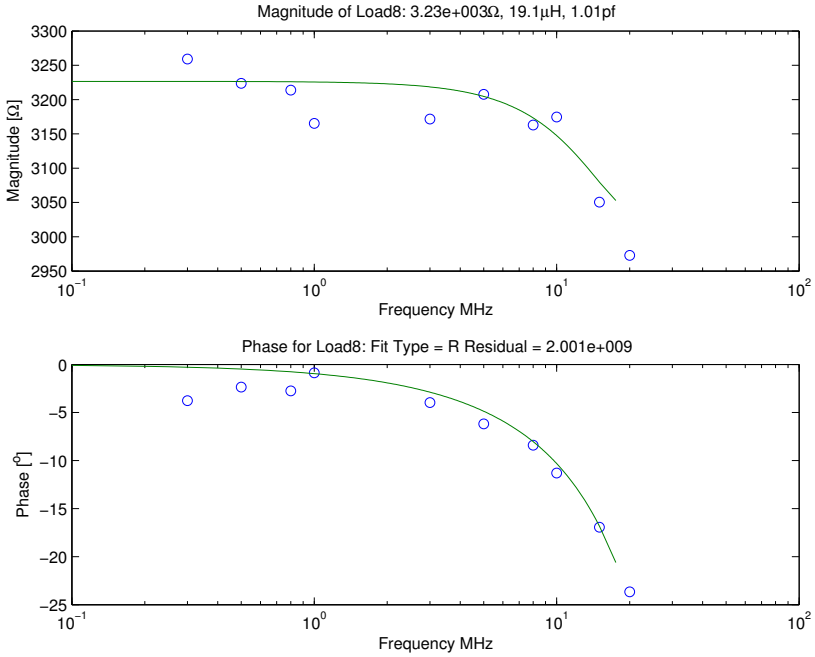

Fig. D.8: Calibration load 8, a 3 kΩ resistor.

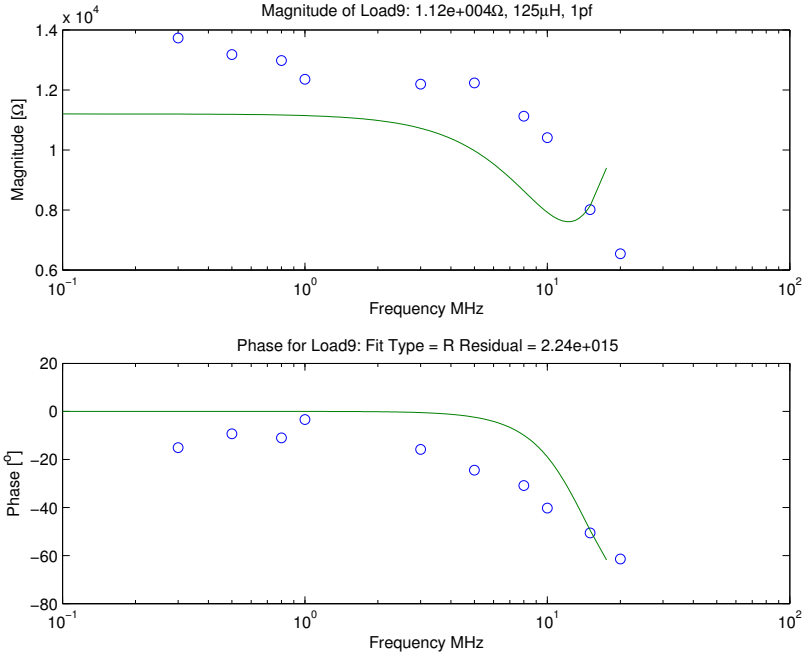

Fig. D.9: Calibration load 9, a 10 kΩ resistor.

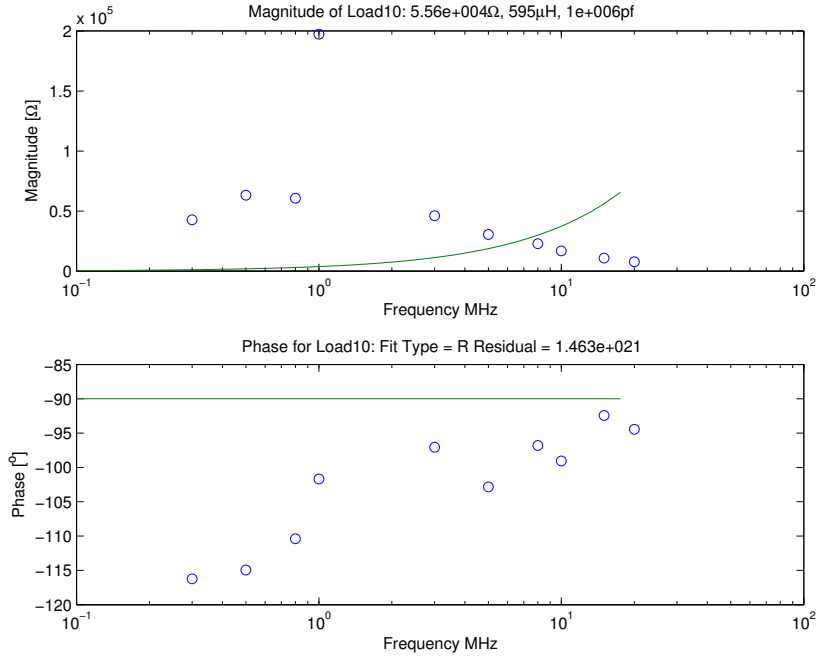

Fig. D.10: Calibration load 10, a 50 kΩ resistor.

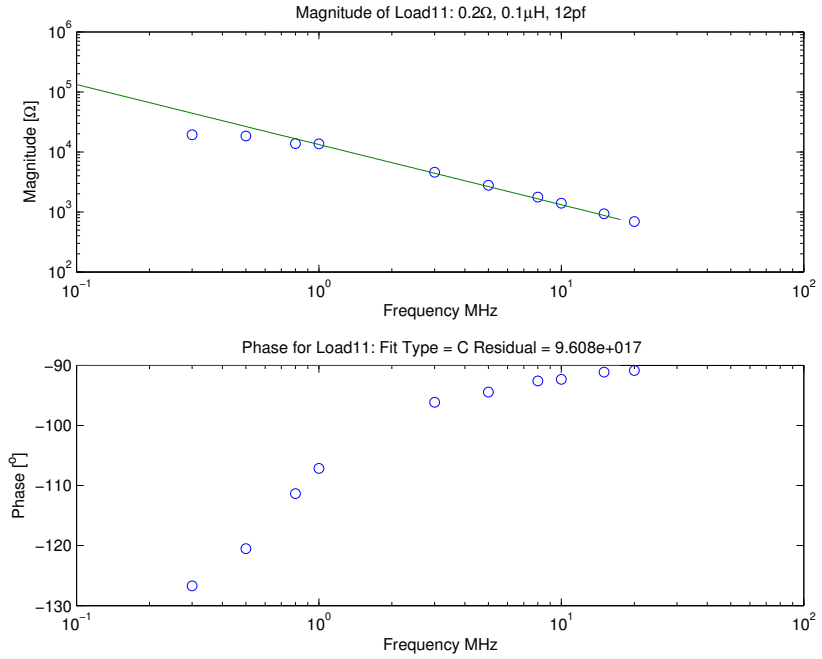

Fig. D.11: Calibration load 11, a 10 pF capacitor.

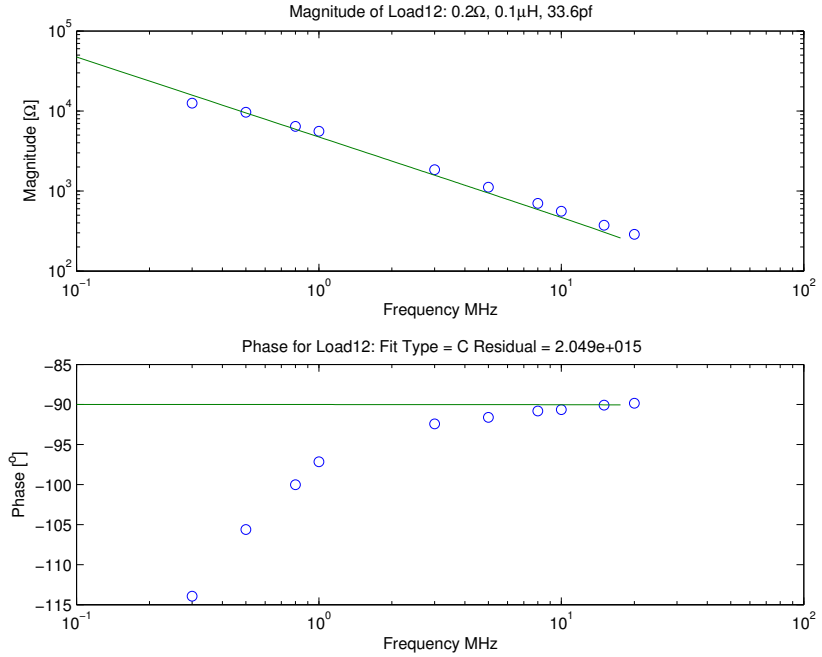

Fig. D.12: Calibration load 12, a 27 pF capacitor.

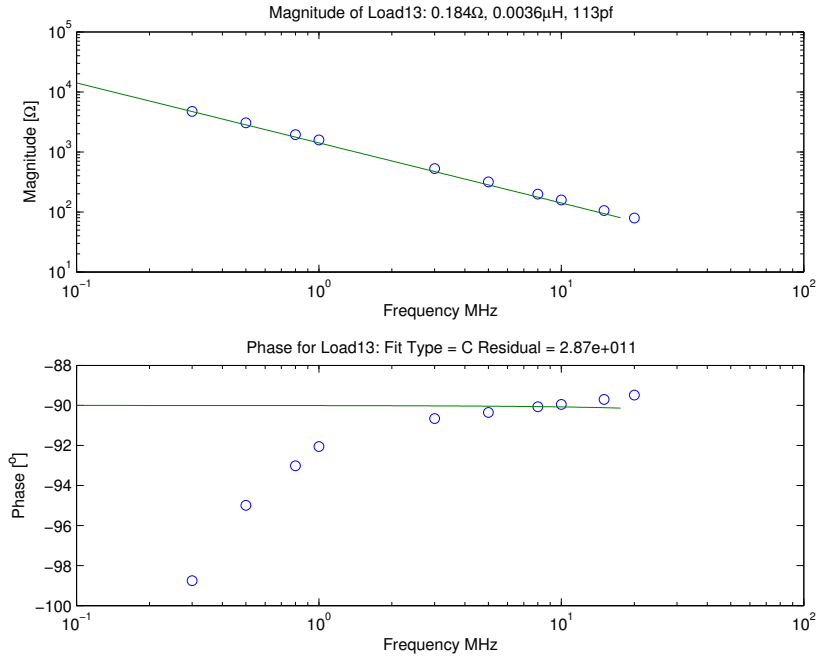

Fig. D.13: Calibration load 13, a 100 pF capacitor.

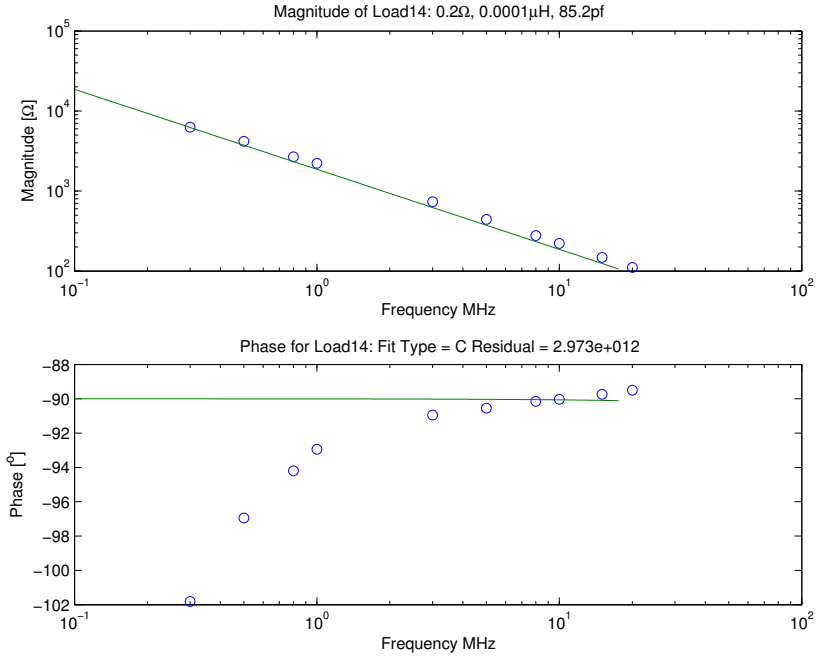

Fig. D.14: Calibration load 14, a 72 pF capacitor.

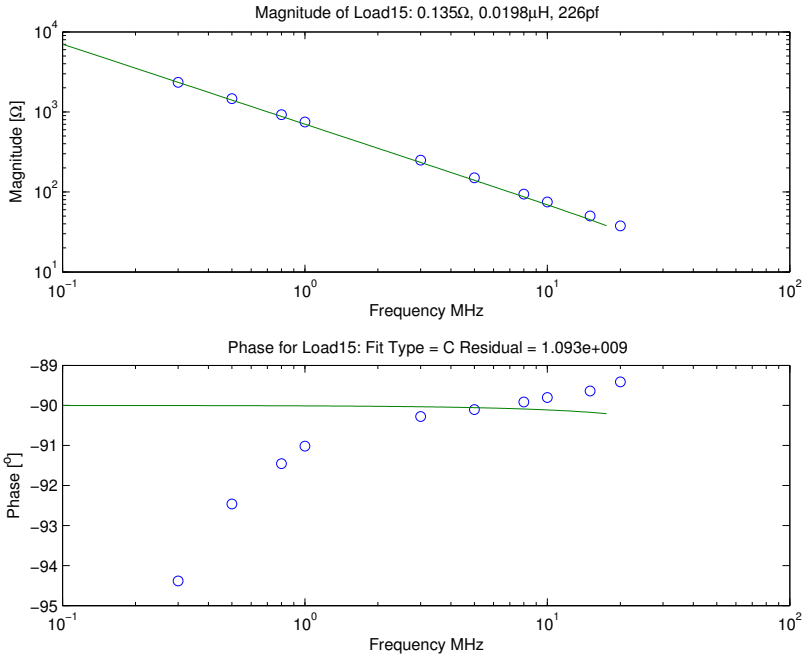

Fig. D.15: Calibration load 15, a 220 pF capacitor.

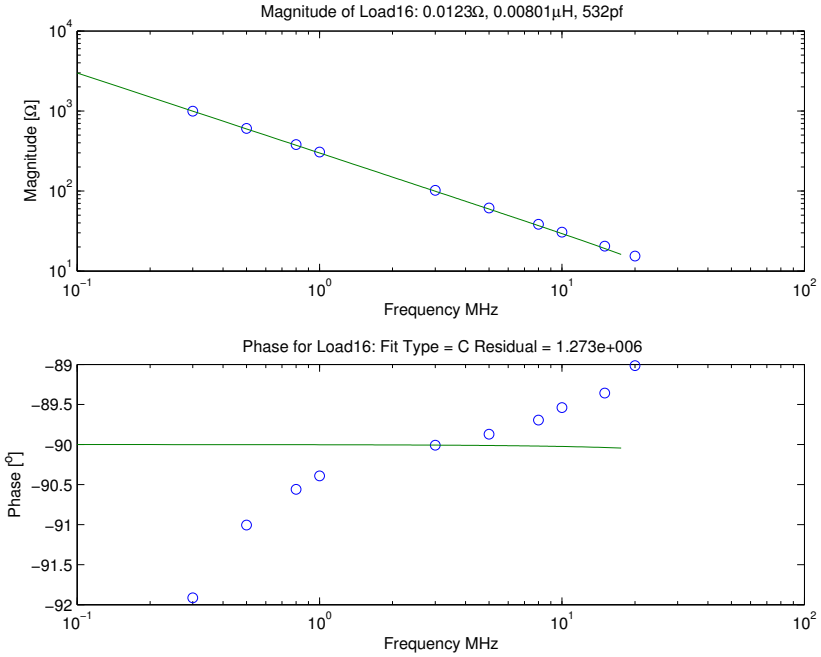

Fig. D.16: Calibration load 16, a 560 pF capacitor.

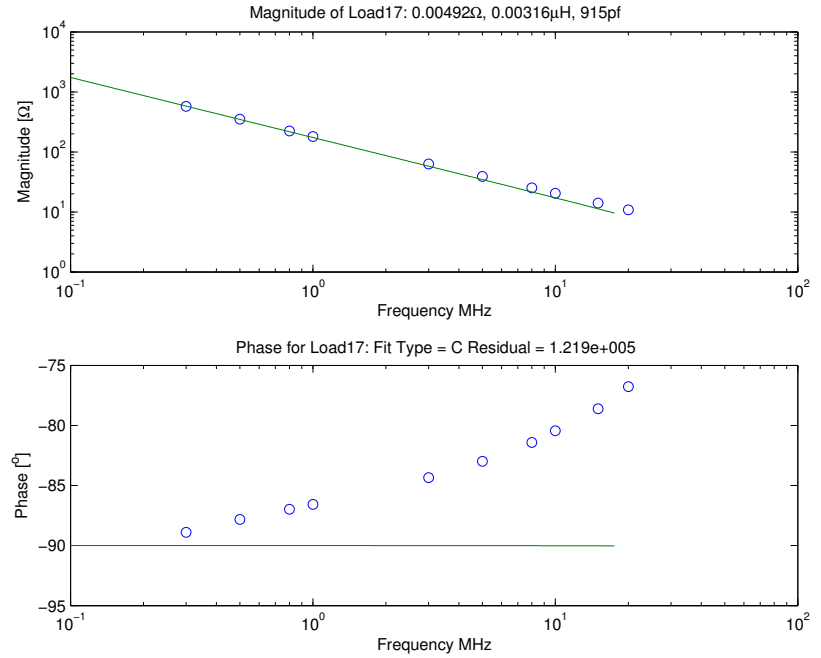

Fig. D.17: Calibration load 17, a 1 nF capacitor.

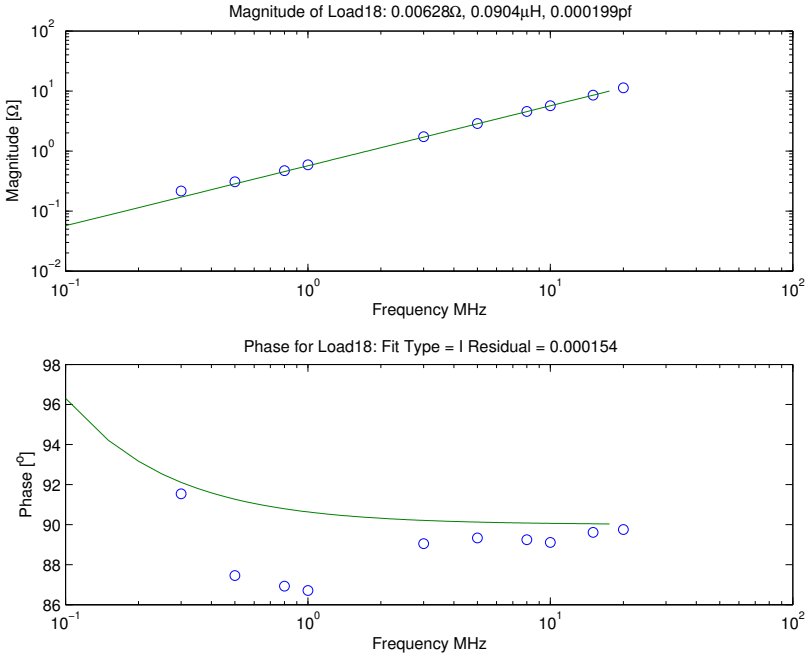

Fig. D.18: Calibration load 18, a 0.1 μH inductor.

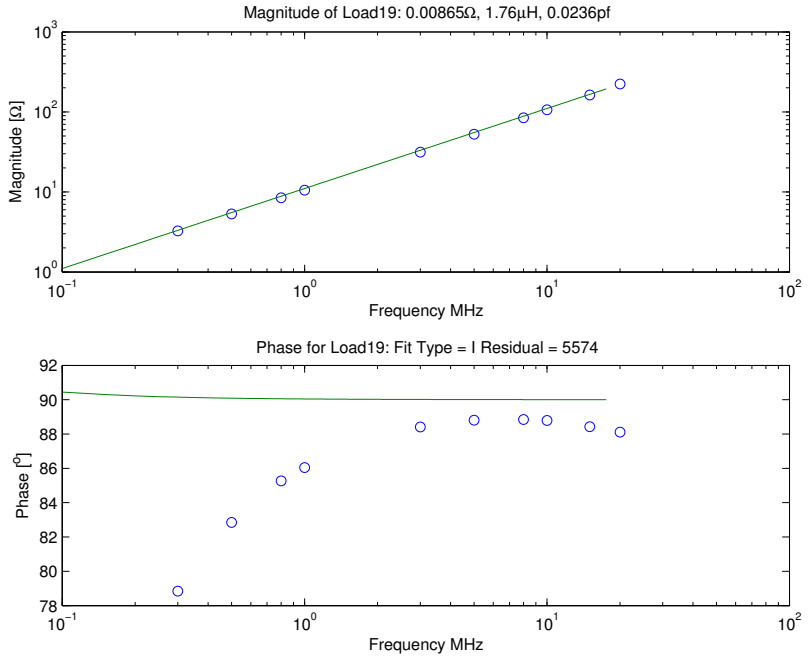

Fig. D.19: Calibration load 19, a 1.8 μH inductor.

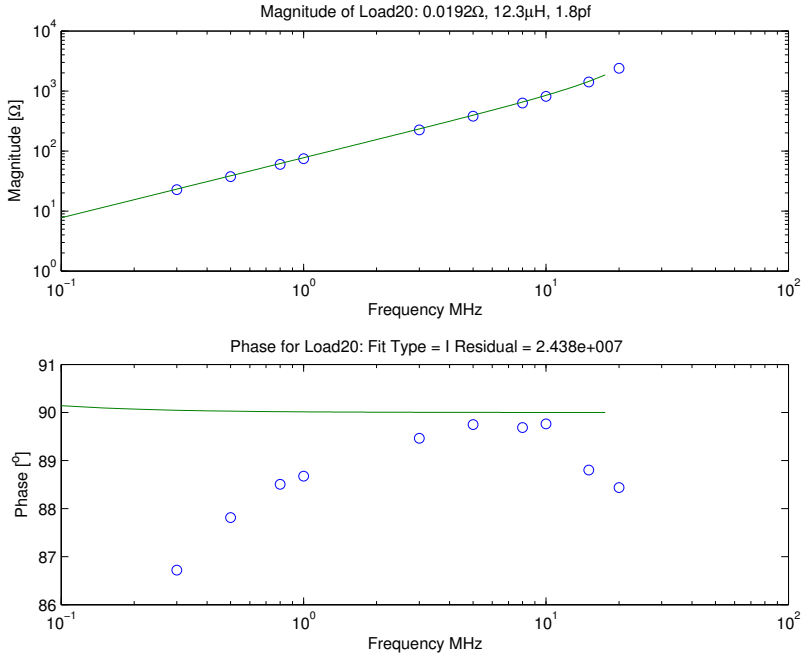

Fig. D.20: Calibration load 20, a 12 μH inductor.

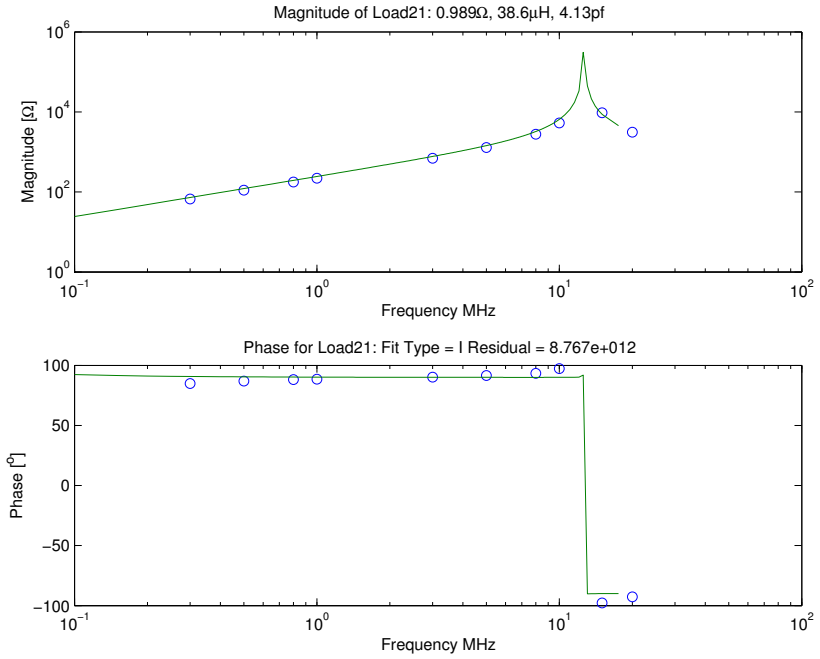

Fig. D.21: Calibration load 21, a 39 μH inductor.

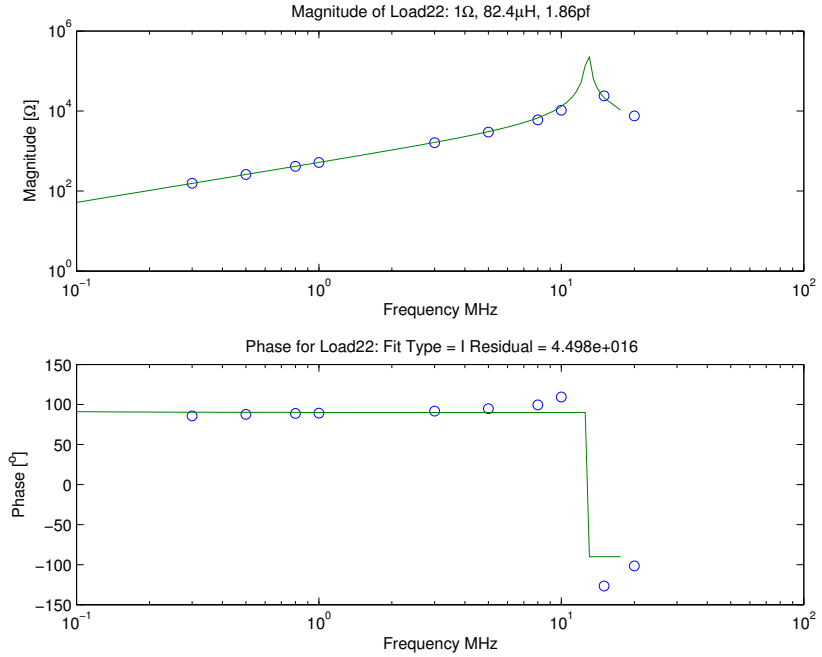

Fig. D.22: Calibration load 22, a 82 μH inductor.

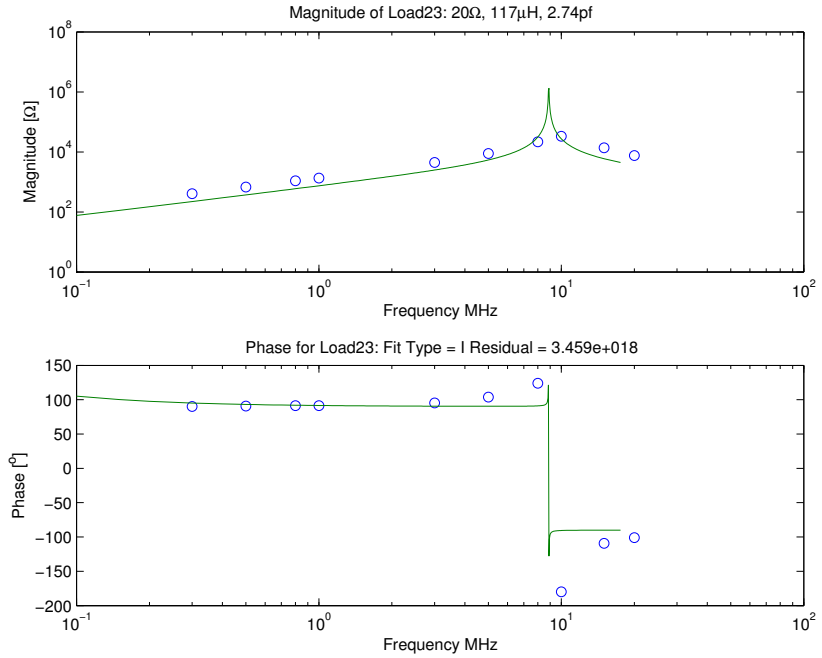

Fig. D.23: Calibration load 23, a 120 μH inductor.